GEORG-AUGUST-UNIVERSITÄT
GÖTTINGEN

Fakultät für
Physik

Master's Thesis

Suche nach $H^{\pm} \rightarrow W^{\pm}Z$-Ereignissen mit dem ATLAS-Detektor am LHC

Search for $H^{\pm} \rightarrow W^{\pm}Z$ events with the ATLAS detector at the LHC

prepared by

Henrike Fleischhack

from Oldenburg

at the II. Physikalisches Institut

Thesis number:	II.Physik-UniGö-MSc-2012/04
Thesis period:	26th September 2011 until 2nd April 2012
First referee:	Prof. Dr. Arnulf Quadt
Second referee:	Prof. Dr. Steffen Schumann
Supervisor:	Dr. Ulrike Blumenschein

Abstract

In this work, the vertex $H^{\pm}W^{\pm}Z^{0}$ is examined in the context of the production and decay of a charged Higgs at the Large Hadron Collider at CERN. The existence of this vertex would be a clear sign for new physics beyond the Standard Model. Signal properties and possible background processes are studied using Monte Carlo simulations. The MC simulations of the backgrounds are validated against 2011 data from the ATLAS detector and expected limits for the vertex factor are derived.

Zusammenfassung

In dieser Arbeit wird der Vertex $H^{\pm}W^{\pm}Z^{0}$ im Rahmen der Produktion und des Zerfalls geladener Higgs-Bosonen am Large Hadron Collider am CERN untersucht. Das Vorhandensein dieses Vertex wäre ein klarer Hinweis auf neue Physik jenseits des Standardmodells. Die Eigenschaften des Signalprozesses und eventueller Untergrundprozesse wird anhand von Monte-Carlo-Simulationen studiert. Die MC-Simulationen des Untergrundes werden mit den 2011-er Daten des ATLAS-Detektors validiert und erwartete Limits auf den Vertex-Faktor werden hergeleitet.

Contents

1. Introduction

Particle physics offers insights into the workings of nature on a very fundamental level. It is concerned with the behaviour of matter on tiny length scales and at large energies and describes the production, interactions and eventual decay of the fundamental constituents of ordinary matter, and their heavier counterparts. The Standard Model of particle physics offers a well-tested theoretical framework that predicts many properties of elementary particles and their interactions to a high level of precision.

The field of experimental particle physics, especially collider physics, has seen a lot of progress over the last few decades. With the collider experiments at LEP, HERA, Tevatron, and now the LHC, theory predictions made using the Standard Model have been tested to a very high level of precision. Almost all predicted particles have been observed and their properties measured. First potential hints of the Higgs boson, the last missing puzzle piece, have been seen recently.

Until now, no significant deviations from the Standard Model of particle physics have been found. However, this might change soon: The LHC, taking collision data since 2009, is advancing into energy regimes that have never been produced in laboratory conditions before. The search for new physics is well under way, using data taken by the two multi-purpose detectors ATLAS and CMS as well as the more specialised ones, ALICE and LHC-B. There are many possible extensions to the Standard Model predicting exciting new physics processes that have to be understood, searched for and either observed or excluded.

This thesis focuses on the search for charged Higgs bosons decaying into a charged $W^{\pm}$ and a neutral Z^0 boson with the ATLAS experiment at the LHC. This process, if observed, would be a strong hint for a highly non-standard Higgs sector, and would already exclude some of the more popular extensions of the Standard Model. It offers an interesting and challenging signature that will be searched for with data taken by the ATLAS detector.

This thesis is organised as follows: In chapter 2, the underlying theory, the Standard Model of particle physics and some of its extensions, is summarised. The experimental setup at the LHC and especially ATLAS is described in chapter 3. Chapter 4 gives an overview over some methods that are used in the analysis, in particular boosted decision trees and limit setting procedures. In chapter 5, the results of phenomenological studies of the $H^{\pm} \rightarrow W^{\pm}Z$ decay, performed in collaboration with the THEP group at Uppsala universitet, are reported. The results of studies carried out using the ATLAS detector, as a member of the II. Physikalisches Institut at the Georg-August-Universität Göttingen[1], are reported in chapter 6. Limits of the production cross section of the charged Higgs times the branching ratio for the decay in question are derived. Chapter 7 concludes and summarises the results.

[1] in der Arbeitsgruppe A. Quadt, experimental hadron collider physics

2. Theoretical Background

In this chapter, a short overview of the Standard Model of particle physics, its implications and possible extensions will be given. Extensive treatments of this can be found in e.g. [1, 2].
In addition, section 2.5 gives a short overview over the techniques used for the simulation of events at particle colliders.

2.1. The Standard Model of Particle Physics

The Standard Model of particle physics (SM) is a set of quantum field theories that describe the properties and interactions of elementary particles. Interactions are modeled by the exchange of gauge bosons. The elementary particle content of the SM can be divided into *fermions* with half integer spin and *bosons* with integer spin. The fermions can be further divided into *quarks* (with colour charge) and *leptons* (no colour charge). Sorting the particles by mass, we find three "generations", giving rise to an approximate flavour symmetry. Each generation contains two quarks, one charged lepton and one neutrino (uncharged lepton).
On the boson side, we have photons, $W^{\pm}$ and Z^0 bosons mediating the electroweak interactions and gluons mediating the strong interactions. Photons couple to all charged particles, Z^0 bosons to charged or left-handed particles (and charged or right-handed antiparticles). $W^{\pm}$ bosons couple to left-handed particles and right-handed anti-particles. They carry electrical charge and are the only gauge bosons that can mediate flavour changes.
Gluons couple to colour charge, i.e. to quarks and other gluons. Because the gluons themselves carry colour charge, the strong force behaves differently compared to the more well-known electromagnetic force: It gets stronger the more the particles are

separated, but is small for short distances/high energies. This leads to a phenomenon called "confinement", which means that all macroscopically observed objects must be colour neutral. Hence, quarks and gluons can only exist in bound states, called *hadrons*, e.g. in a combination of quark/antiquark (meson) or three quarks (baryon).

2.1.1. The Proton

As this work will deal with hadron collider physics, it is important to understand the structure of the protons that are used in the collisions.

Protons are composite particles, made up of a number of *partons*. The number and properties of the observed partons depends on the probe that is used to measure them, or rather on the momentum transferred between probe and proton. At low momentum transfers, the proton appears as an elementary particle.

At higher momentum transfers one can observe three valence quarks (uud) as well as gluons and quark-anti-quark pairs, the sea quarks. Each parton carries a fraction x of the proton's momentum and energy. The probability of finding a parton (gluon, valence quark, or sea quark) with a given momentum fraction x of the proton's momentum is given by the *parton distribution functions* (*pdf*s). These pdfs can not be predicted by current theoretical calculations. However, their evolution with the momentum transfer is described by the so-called *DGLAP equations* [3, 4, 5]. There have been several fits of pdfs to measurements over a wide range of momentum transfers and momentum fractions, in proton-antiproton collisions, deep inelastic scattering in electron-proton collisions, and fixed target experiments [6]. Generally, it has been found that gluons dominate at low x, valence quarks at high x [7].

2.1.2. The Standard Model Lagrangian

The fermions described above can be modeled using wave functions, arranged in spinors. They follow certain equations of motion, depending on the spin[1]. The interactions described above can be obtained by starting out with the observed fermion content and requiring a local $U(1) \times SU(2) \times SU(3)$ gauge symmetry. The neutral gauge bosons from the $U(1) \times SU(2)$ symmetry mix to the observed (massless) photon and (massive)

[1] e.g. the Dirac equation for a (hypothetical) free electron

Z^0. Field equations can be obtained by the Euler-Lagrange formalism, i.e. using

$$\frac{\partial \mathcal{L}}{\partial \phi_i} - \partial_\mu \left(\frac{\partial \mathcal{L}}{\partial(\partial_\mu \phi_i)} \right) = 0$$

for all the fields ϕ_i the Lagrangian depends on. These equations are in general not easily solvable. One can use them to find the time evolution for quantised fields. For electroweak interactions and for strong interactions at high energies, this time evolution can be treated using a perturbative approach (Feynman calculus) to calculate observables. This will be described in more detail in section 2.1.3. The "Feynman rules" used during the calculations can be directly extracted from the Lagrangian; see e.g. [1, 2, 8].

Generally, one wants to compare theoretical predictions to experimental results to verify/disprove a theory and/or to measure parameters that are not fixed by the theory. Common observables are cross sections and decay rates. The cross section gives the probability of a given scattering process in a collision experiment. The (partial) decay width gives the probability of a particle decaying into a given final state in a given time. The total decay width (the sum of all partial decay widths) is proportional to the inverse of the life-time of a particle. Many other common observables are derived from these. As an example, the *branching ratio* is the ratio of a partial decay width to the total decay width. It gives the probability for a particle to decay into a given final state.

2.1.3. Hadronic Cross Sections

For hadronic interactions, e.g. the proton-proton collisions that will be treated here, the factorization theorem may be applied: It is possible to split up hadronic cross sections, e.g. the one giving the probability to produce a Z boson by quark-antiquark scattering in a given proton-proton collision, into several parts that can be treated (nearly) independently:

- The "hard scattering" of quarks or gluons, modeled by a perturbative approach. This may be used as long as the QCD coupling constant, α_s, is significantly smaller than 1, i.e. for sufficiently large momentum transfers.

- The probability of finding a quark with a given momentum inside a proton, modeled by the parton distribution functions, as described in section 2.1.1.

- Possible interactions of the other partons in the two protons (*underlying event*), measured in data.

- The *hadronisation* or *fragmentation* of final-state quarks and antiquarks into hadrons, modeled by fragmentation functions that are fitted to measurements.

Using the Feynman approach, the hard scattering cross section is given as the sum of all contributions with a given final state. This is written as a power series/Taylor expansion in the (small) coupling parameter(s). The contribution with the minimal number of vertices usually dominates and is called *leading order* (LO) contribution. Next-to-leading order (NLO) corrections that have to be taken into account include *real* emissions and *virtual* corrections. Both of these corrections are divergent, but their sum is finite.

2.1.4. The Higgs Mechanism

However, while stipulation of gauge symmetry leads to a Lagrangian that describes the interactions well, it only predicts massless gauge bosons. Moreover, it can not accommodate fermion masses either, even if they are inserted by hand. Since we can observe masses for almost all fermions and some gauge bosons, there must be another mechanism leading to massive particles. The most accepted way to explain particle masses is the Higgs mechanism, developed in 1964 [9, 10, 11]. It postulates a complex scalar doublet field ϕ with a potential

$$V = -\mu^2 \phi^\dagger \phi + \lambda (\phi^\dagger \phi)^2. \tag{2.1}$$

If $\mu^2 > 0$ and $\lambda > 0$, this potential has a local *maximum* at 0, but a (global) *minimum* at

$$|\langle \phi \rangle| = v := \sqrt{\frac{\mu}{2\lambda}}, \tag{2.2}$$

the so called *vacuum expectation value (vev)* $|\langle \phi \rangle|$. The vacuum state/ground state of the Higgs field is not the state $\phi = 0$, but some state with $|\phi| = v$. We are interested in small fluctuations of the field around this ground state, so it is useful to rewrite the Lagrangian using $\phi(x) = \langle \phi \rangle + h(x)$. The interactions between bosons/fermions and the Higgs field can then be split accordingly. The terms containing the constant vacuum field have the desired shape and give the mass terms. The “mass” of a particle is thus

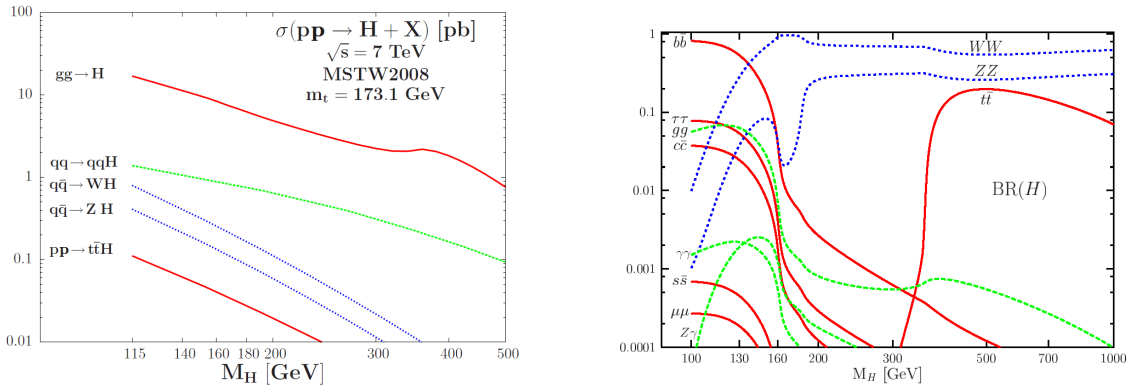

(a) **(b)**

Figure 2.1.: Left: Standard model Higgs production cross section for different production processes at a 7 TeV proton-proton collider, from [12]. Right: Standard model Higgs branching ratios for different decay modes, from [13].

Vertex	Vertex factor
$Hf\bar{f}$	$-\frac{igm_f}{2m_W}$
HW^+W^-	$igm_W g^{\mu\nu}$
HHW^+W^-	$\frac{1}{2}ig^2 m g_{\mu\nu}$
HZZ	$\frac{igm_Z}{\cos(\theta_W)} g^{\mu\nu}$
$HHZZ$	$\frac{ig^2}{2\cos^2(\theta_W)} g_{\mu\nu}$
HHH	$\frac{-3igm_H^2}{2m_W}$
$HHHH$	$\frac{-3ig^2 m_H^2}{4m_W^2}$

Table 2.1.: Vertex factors for the SM Higgs coupling to fermions and bosons. g is the $SU(2)$ coupling constant, θ_W the Weinberg angle. Cf. [8].

caused by the interactions with the vacuum Higgs field. Terms containing the space-time dependent $h(x)$ describe the dynamics of and the interactions of other particles with the *Higgs boson*, described in the following section.

2.1.5. Phenomenology of the Higgs Boson

More details on the Standard Model Higgs boson and its properties can be found e.g. in [8, 12, 13]. It is common to choose the ground state so that one of the two components of the doublet is 0. Rewriting the Lagrangian by expanding around the ground state then gives one massive and one massless scalar boson. The massless boson is a so called Goldstone-boson. It is not a physical particle and can indeed be removed by

choosing a convenient gauge. We are left with one additional scalar, the Higgs boson, with a mass term and self interaction terms. The Higgs boson also couples to the now massive gauge bosons. To obtain fermion masses, one has to add terms containing fermions and the Higgs doublet to the Lagrangian. This means that the Higgs boson has to couple to fermions, with a coupling strength proportional to the fermion's mass. The predicted couplings are summarised in table 2.1.

Production at Hadron Collider Experiments

As the Higgs boson predominantly couples to heavy particles, the major production modes at hadron colliders involve heavy vector bosons or top quarks. At the LHC, the expected dominant production channel for the Higgs boson is gluon fusion (via a top loop), dominating by about an order of magnitude. Other production channels are vector boson fusion of W^+W^- or Z^0Z^0, Higgs-Strahlung from an off-shell W or Z, and in association with a $t\bar{t}$ pair. The cross sections for these processes depend on the centre of mass (cms) energy and the Higgs mass. The expected values for a proton-proton collider with a cms energy of 7 TeV, the energy that the LHC ran at in 2011, are shown in Fig. 2.1(a).

Decay

The favoured decay modes of the Higgs strongly depend on its mass. Basically, the Higgs will predominantly decay into the heaviest decay mode that is kinematically allowed. For low masses (significantly lower than, say, $130\,\text{GeV}$), this will be $b\bar{b}$ or $\tau^+\tau^-$, for higher masses W^+W^-, Z^0Z^0, or $t\bar{t}$. Due to the relatively short lifetime and therefore large width of the two heavy vector bosons, the Higgs can decay into boson pairs where at least one boson is virtual even in mass ranges where the decay into two real bosons would not be allowed. Decays into pairs of photons or gluons are possible via loops. The expected branching ratios for a SM Higgs boson are shown in Fig. 2.1(b).

2.1.6. Current Experimental Status

The Higgs field is an essential part of the Standard Model and its associated boson is the only elementary particle described by the SM that has not been discovered yet. All its couplings and properties are fixed by the SM except for its mass. There are,

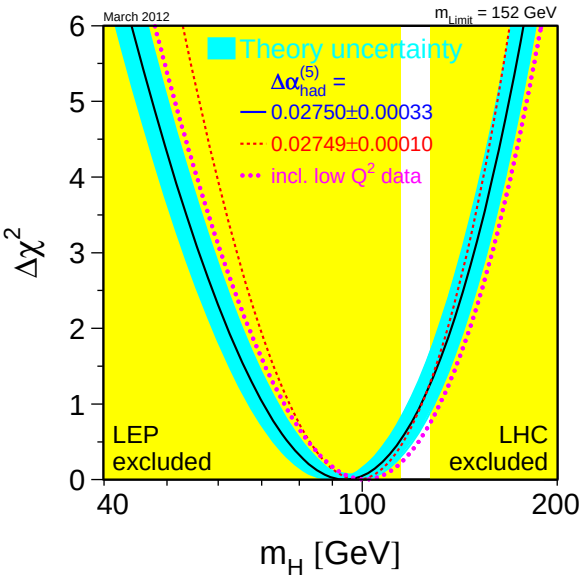

Figure 2.2.: Likelihood ratio for the Higgs mass in a fit to precision measurements of Standard Model observables [14], and mass ranges excluded by direct searches. The preferred value for the Higgs mass is (94^{+29}_{-24}) GeV. This uncertainty refers to the fit uncertainty ($\Delta\chi^2 = 1$) and does not take the theory uncertainty (blue band) into account.

however, a number of direct and indirect constraints on the Higgs mass both from theory and experiments.

The Higgs mass influences other SM parameters like the mass and width of the W boson via loop corrections. A recent fit from the LEP electroweak working group [14], using precision measurements of several electroweak observables made at the Large Electron Positron Collider (LEP), the Stanford Linear Collider (SLC), and Tevatron puts the Higgs mass at (94^{+29}_{-24}) GeV, cf. Fig. 2.2.

Through direct measurements at LEP, Tevatron, and the Large Hadron Collider (LHC), large ranges of the SM Higgs mass have been excluded at $95\,\%$CL or more [15, 16, 17, 18]. In particular, a SM Higgs boson cannot be lighter than $115.5\,$GeV. The range $127-600$ GeV has also been excluded. The different colliders are sensitive to different mass ranges, but with large overlaps. Hence, a full combination (which is not available yet) might lead to slightly different exclusion regions.

CMS, ATLAS, and both Tevatron experiments see a slight excess of events that are compatible with a Higgs with a mass of $124\,$GeV [18], $126\,$GeV [17] and $115-$

135 GeV [16], respectively[2]. These results can be seen as a hint for a SM Higgs boson in this mass range, but the statistic significance is not high enough to classify this as a "discovery" of the Higgs boson. Further conclusions will be drawn once a full combination of results from the four experiments is available, or after more data has been taken and analyzed by the LHC experiments.

2.2. Extensions to the Standard Model Higgs Sector

While one Higgs doublet is sufficient to give mass to all particles in the Standard Model, there is no a priori reason why there should only be one such Higgs doublet. In fact, supersymmetry, a popular extension of the SM, requires at least two scalar doublets in the Higgs sector. But a non-standard Higgs sector can exist independent of other extensions of the Standard Model. Additional scalar doublets or triplets will lead to the existence of additional charged (or even doubly charged) Higgs bosons. Most non-SM Higgs models predict deviations from the SM values of certain precision observables, which have not been observed so far. Hence, some regions of the parameter space of each extended Higgs sector have already been excluded. However, by choosing model parameters appropriately, it is usually possible to stay compliant with experimental results. On the other hand, no evidence for a non-SM Higgs sector (e.g. the detection of a non-SM Higgs boson) has been reported. A more detailed overview can be found in [8].

2.2.1. Two-Higgs-Doublet Models (2HDM)

The treatment here closely follows [8]. The simplest way to extend the Higgs sector is to introduce an additional complex scalar doublet. This is needed e.g. in supersymmetry, where one needs one Higgs doublet coupling to the up-type quarks and leptons and another one coupling to the down-type quarks and leptons. After electroweak symmetry breaking, there are five Higgs bosons (in contrast to the Standard Model's one Higgs boson), two of which are charged. The charged Higgs bosons are of interest here and will be treated in a little more detail. The neutral Higgs bosons mix to two scalar and one pseudoscalar eigenstate. In general, this will lead to flavour changing neutral

[2]The LEP experiments were not sensitive in this mass range.

currents, on which there are tight constraints from experiment. However, this can be avoided by specifying appropriate couplings of the fermions to the Higgs doublets. In context of the Minimal Supersymmetric Standard Model (MSSM), this is achieved automatically.

Two-Higgs-Doublet models can offer an interesting and challenging phenomenology in the Higgs sector. Especially the charged scalar bosons they predict offer new search channels, for example $t \to H^+ b$ decays. However, in these types of models, $H^\pm W^\pm Z$ couplings always vanish at tree level [8]. They might come in via loops (dominantly tb or some supersymmetric particles), which means they will be suppressed compared to tree-level couplings. $H^\pm \to W^\pm Z$ decays might still be somewhat important in special kinematic regions. However, the authors of [19] find that these decays are probably rare enough not to play an important role in the discovery of such a Higgs sector, hence they will not be treated here.

2.2.2. Triplet Models

Instead of (or in addition to) a second scalar doublet one may extend the Standard Model Higgs sector by an additional real or complex scalar $SU(2)$ triplet [8, 19]. The kind of bosons one obtains depend on the hypercharge Y of the triplet. $Y = 2$ triplets will lead to doubly charged Higgs bosons.

In models with only one Higgs triplet, the vacuum expectation value of the triplet is constrained by electroweak precision measurements, since a Higgs triplet would lead to deviations of the electroweak mass parameter $\rho = \frac{M_W}{M_Z \cdot \cos(\theta_W)}$ from unity. The vacuum expectation value of the triplet would have to be very small. Hence, the additional Higgs bosons would only couple very weakly to SM particles and they would be hard to discover.

In models with one real and one complex triplet (and an arbitrary number of additional doublets and singlets), one can impose an additional symmetry on the model (i.e. tune the vacuum expectation values of the two triplets) to fix $\rho = 1$ at tree level, like in the Standard Model. In this case, the vacuum expectation values of the triplets might be relatively large, such that they could be produced in sufficient numbers to be discovered at a contemporary collider experiment.

2.3. Charged Higgs Phenomenology

In most 2HDM or Higgs triplet models, the charged Higgs bosons couple to fermions, preferably to the heavier ones. The relative coupling strengths of the Higgs bosons to leptons and quarks depend on the model. A more detailed description can be found in [8].

2.3.1. Production

Depending on its mass and the relevant coupling strengths, there are several ways to produce a charged Higgs boson at a proton collider. If the charged Higgs is lighter than the top quark, it can be produced via the decay $t \rightarrow H^+b$. It can also be produced in association with a top quark or a weak boson or even with a neutral Higgs boson. If the $H^\pm W^\pm Z$ coupling is large enough, the charged Higgs can be produced via vector boson fusion of W and Z, cf. section 5.2. Pairs of charged Higgs bosons may also be produced, e.g. via a Z^0 boson or photon.

2.3.2. Decays

Again, the possible decay modes depend on the mass of the Higgs and the coupling strengths. If one assumes that the Yukawa couplings of the second Higgs doublet correspond to those of the first Higgs doublet, the charged Higgs would preferably decay into heavy fermions, i.e. $t\bar{b}$ (if kinematically allowed), $c\bar{s}$ and $\tau^+\nu_\tau$. This is for example the case in the MSSM extension to the Standard Model. However, if one finds a charged Higgs boson, it will become important to further examine the underlying properties of the Higgs sector. In this work, therefore, a different decay channel will be examined: The decay into two (real) vector bosons $H^\pm \rightarrow W^\pm Z$. This is kinematically allowed for $m_{H^\pm} > m_{W^\pm} + m_Z$. Its associated decay width depends on the (effective) coupling of the vertex $H^\pm W^\pm Z$. Measurements of the coupling of the charged Higgs to W and Z bosons are a powerful tool to distinguish different extended Higgs models, such as models with several Higgs doublets from triplet models.

2.4. The Vertex $H^{\pm}W^{\pm}Z$

In the following, I will develop a general description of the vertex $H^{\pm}W^{\pm}Z$, following [19]. Then I will specify the behaviour in different physical models.

2.4.1. General Phenomenological Description

In general, the vertex factor corresponding to $H^{\pm}W^{\pm}Z$ derived from the Lagrangian will be of the form

$$i \cdot g \cdot m_W \cdot V_{\mu\nu} \cdot \varepsilon_W^{*\mu}(p_W, \lambda_W)\, \varepsilon_W^{*\nu}(p_Z, \lambda_Z)\,,$$

where the ε are polarization vectors of the weak gauge bosons with momentum p and helicity λ, and $V_{\mu\nu}$ is a stand-in for the (model-dependent) vertex factor. In the most general case, $V_{\mu\nu}$ can be written as

$$V_{\mu\nu} = F g_{\mu\nu} + \frac{G}{m_W^2} p_{Z\,\mu} p_{W\,\nu} + \frac{H}{m_W^2} \epsilon_{\mu\nu\rho\sigma} p_Z{}^{\rho} p_W{}^{\sigma},$$

with form factors F, G, H and the totally antisymmetric tensor ϵ. This corresponds to an effective Lagrangian

$$\mathcal{L}_{eff} = f_{HWZ} \cdot H^{\pm} W_{\mu}^{\mp} Z^{\mu} + g_{HWZ} \cdot F_Z^{\mu\nu} F_{\mu\nu}^W + h_{HWZ} \cdot i\epsilon_{\mu\nu\rho\sigma} F_Z^{\mu\nu} F_{\rho\sigma}^W$$

with coupling strengths $f_{HWZ}, g_{HWZ}, h_{HWZ}$ and field strength tensors $F_{W/Z}$. The (absolute and relative) strength of the couplings then depends on the physical model in question. At tree level, only the F term can contribute. It turns out that it is always the dominant coupling. The authors of [19] calculate the approximate coupling strengths for different models which predict the existence of charged Higgs bosons.

2.4.2. Models with Doublets

In models containing one or more additional Higgs doublets, one will obtain a charged Higgs boson. Those models can not contain a tree level $H^{\pm}W^{\pm}Z$ coupling. However, this vertex exists at loop level and can be described by an effective Lagrangian as shown above. According to the authors of [19], the dominant contributions come from tb and neutral Higgs bosons. In the case of a supersymmetric model, there can also be

contributions from supersymmetric particles.
The effective couplings are fixed by the model and can in principle be calculated from loop diagrams. Of course, they depend on the parameters of the model, i.e. the masses and couplings of the loop particles. These parameters may be constrained by theory or experiment. The authors of [19] find that the G and H contributions can be neglected in the 2HDM case. They find $|F^{2HDM}|^2 \sim 10^{-3}$ $(10^{-4}, 10^{-5})$ for $\tan(\beta) = 0.3$ $(1.0, 3-10)$. Here, $\tan(\beta)$ is the ratio of the vevs of the two Higgs doublets. Lower $\tan(\beta)$ values are not considered because they would lead to a too large Yukawa coupling for the top quark. The tb loop dominates for most $\tan(\beta)$ values. The bosonic loop only becomes important for $3 \lesssim \tan(\beta) \lesssim 10$. For the MSSM model, they find that adding contributions from loops of supersymmetric particles does not significantly change the coupling.

2.4.3. Models with Triplets

In models containing additional Higgs triplets, F will generally be non-zero at tree level, and hence contribute more than the loop-induced G and H terms. The details depend on the model, but generally F will be proportional to $\frac{v'}{v}$, where v is the vacuum expectation value of the Higgs doublet and v' is the vev of the triplet (or a combination of the triplet vevs in case of more that one Higgs triplet).
In models with *one* Higgs triplet, v' is generally constrained to be quite small from precision measurements of the ρ parameter. For example, for the low energy effective field theory in the Littlest Higgs model (LLH), the authors of [8] predict one complex Higgs triplet field. The authors of [19] find (to leading order)

$$F^{LLH} = \frac{4v'}{\cos\theta_W} \text{ and } m_\Phi = \frac{2m_h^2 f^2}{v^2 \cdot \left(1 - (4v'f/v^2)^2\right)}.$$

Here, $m_\Phi (= 115\,\text{GeV})$ refers to the mass of the triplet field, m_h is the SM Higgs mass, and f is the symmetry breaking scale. From electroweak precision measurements, one finds $1 \lesssim v' \lesssim 4\,\text{GeV}$ for $f = 2\,\text{TeV}$. The authors of [19] calculate the form factor F for two different reference points.

$$\begin{aligned} f = 1\,\text{TeV} \quad v' = 5\,\text{GeV} \qquad & m_{H^\pm} = 700\,\text{GeV} \;\; |F^{LLH}|^2 \simeq 0.0085 \;\text{ and} \\ f = 2\,\text{TeV} \quad v' = 4\,\text{GeV} \qquad & m_{H^\pm} = 1560\,\text{GeV} \;\; |F^{LLH}|^2 \simeq 0.0054. \end{aligned}$$

For models with additional real and complex triplet fields, one may impose an additional symmetry $v_r' = v_c'(= v')$ to set the ρ parameter to 1 at tree level[3]. This custodial symmetry avoids the constraints mentioned above. Here, the existence of exactly one real and one complex triplet (in addition to the Standard Model's doublet field) is assumed. After electroweak symmetry breaking, the Higgs sector consists of a five-plet, a three-plet[4] and two singlets under the custodial symmetry. If the three-plet and the five-plet do not mix, the five-plet does not couple to fermions. The singly charged five-plet Higgs, $H_5^{\pm}$, couples to W and Z bosons. The relevant form factor is given by

$$F^{triplet} = \frac{1}{\cos\theta_W} \cdot \sqrt{\frac{8v'^2}{v^2 + 8v'^2}}.$$

The ratio v'/v can be constrained experimentally, but the constraints depend on the mass of the three-plet Higgs. The authors of [19] use $\frac{\sqrt{8}v'}{v} = 0.5$ and $m_{H_5^{\pm}} = 200\,\text{GeV}$ and find $|F^{triplet}|^2 \simeq 0.26$. In an extended study ([20]), they find

$$|F^{triplet}|^2 = 0.26 - 0.97.$$

In the studies described later on, $F = 1$ was used for simplicity.
Assuming no mixing between the three-plet and the five-plet, the $H_5^{\pm}$ will not couple to fermions. The $H_5^{\pm}W^{\pm}\gamma$ vertex is also zero at tree-level [8]. Hence, the charged five-plet Higgs may only decay into a WZ pair or a combination of scalar and/or massive vector bosons. In the context of this work, it is assumed that the other Higgs bosons are substantially more massive than the weak gauge bosons so that the other decays are kinematically suppressed. Hence they are not considered here; neither is the possibility of the charged Higgs decaying into fermions via loops.

2.5. Monte Carlo Methods

Monte Carlo (MC) integration is a way of numerically evaluating integrals using sequences of pseudo-random numbers. A similar method can also be used to obtain random number sequences following a given distribution, starting from any other distribution. In particle physics, so-called Monte Carlo generators use algorithms based on

[3] Here, $v_r(v_c)$ refers to the vev of the real (complex) triplet, resp.
[4] To avoid confusion with the representations under the electroweak $SU(2)$ gauge group, the representations under the custodial symmetry are referred to as three-plets etc. instead of triplets.

MC integration to calculate physical observables and simulate particle collisions.

2.5.1. Cross Section Calculation and Event Generation

Calculating observables like cross sections analytically is tricky due to the multi-dimensional integrals that have to be solved. Additionally, one often encounters divergences that have to be treated carefully. Due to this, Monte Carlo generators are often used to calculate (leading order or next-to-leading order) differential cross sections. Given the geometry of the experiment, they are also used to simulate collision events, including decays and even interaction of the decay products with a detector.
Roughly, the event generation process can be separated in two steps: First, phase space distributions for the desired processes have to be calculated (this may be done externally, depending on the event generator).
Then the event generator uses pseudo-random numbers to produce the 4-vectors describing a possible collision event. Each event is weighted with factors corresponding to the decay probabilities, the phase space density and (for proton collisions) the momentum distribution of the partons inside the proton[5]. Divergences have to be taken care of, usually by cutting away problematic phase space regions. These should be regions of phase space that cannot be detected by experiments, e.g. radiation of very soft particles. The weights should be normalised so that summing over all produced events gives the total cross section, or the number of expected interactions for a given luminosity.
To make it easier to compare Monte Carlo simulations to data, there is often an additional step, called unweighting, in which certain events are dropped (randomly, with probability inversely proportional to their weight). The events that are kept then all have the same weight. The kinematics of the sample produced in this way should correspond to the "true" distribution.

2.5.2. Showering and Hadronisation

Showering is a method that takes higher-order corrections to the produced processes into account by producing (mostly collinear) gluons and quarks radiating from colour-charged particles. This mimics the processes which happen in reality, leading to the observation of "jets" of hadrons instead of single quarks.

[5] described by parton distribution functions

Due to the so-called "confinement" property of QCD, only colour singlets can be observed macroscopically. Hence, all quarks and antiquarks have to combine to colourless mesons and baryons. This process cannot be described with perturbative calculations. Instead, one uses distributions measured from experiments to simulate that part. For more details, see [21, 22].

2.5.3. Detector Simulation

After passing through a showering and hadronisation algorithm, the particles should have roughly the same kinematic properties as the ones produced in an actual experiment. However, the measuring apparatuses (detectors) used by the experiments are not (and cannot be) perfect. For example, they cannot provide full angular coverage. Moreover, the detection efficiency and resolution depend on the properties of the particle. Hence, detector simulations are often used to be able to compare simulations to actual data, or to study the feasibility of a given analysis. There are many different approaches to detector simulations with varying computation times and levels of accuracy.
One extreme are fast simulations that only apply basic acceptance cuts and Gaussian smearing of energies and momenta, according to expected resolutions. This can be done quite fast and does not require any proprietary information about the detector setup. In chapter 5, the `pgs` software [23] is used for an approximate simulation of the ATLAS detector. On the other hand, there are full detector simulations (e.g. with the `GEANT` [24] package) that follow the paths of charged particles through the whole detector. They use a Monte Carlo approach to account for the statistical nature of decays and e.g. energy deposits in the material. They simulate the raw output of each detector channel, making it necessary to run a simulation of the detector readout/event reconstruction software. The full detector simulations take quite long time to run (longer than event generation steps) and require proprietary software as the precise layout of the detector and the readout/reconstruction software is not publicly available.

3. Experimental Overview

In the following, a short introduction of the experimental setup (proton colliders and detectors) will be given. The focus will be on the ATLAS detector at the LHC collider at CERN, as data taken with the ATLAS detector are used in chapter 6.

3.1. Collider Physics and Detectors

Particle accelerators are an important tool for experimental particle physicists. They are used to accelerate beams of charged particles (usually electrons or protons as well as their anti-particles). These beams can be used for two different types of experiments: fixed target experiments and colliding beam experiments where two high-energy beams collide. The latter type of experiments needs more fine tuning to ensure that the beams collide at the right place. They are widely used as they allow for higher center-of-mass energies to be reached.
At the collision point, particles can scatter off each other, possibly producing other particles. These collisions usually happen inside a detector so that the reaction products can be detected and their properties (e.g. energy and momentum) can be measured. Most detectors that are in use today follow a layered design. The innermost layer (around the beam pipe) is used to track charged particles using, for example, wire chambers or silicon sensors. As the tracking system is usually surrounded by a magnetic field, the tracks can be used to determine the charge and momentum of the measured particles as well as the location of the interaction point. The tracking system is set up so that particles interact minimally with the detector and do not lose much energy.
The calorimeters form the next layers. Most particles deposit all of their energy in them. The energy deposited can be measured and the energy of the particle determined. Most calorimeters are split into two parts. The first one is the electromagnetic

calorimeter, in which electrons, photons, and neutral pions (which quickly decay into photons) deposit most of their energy. Electrons emit bremsstrahlung (photons) when interacting with a nucleus, photons split into electron-positron pairs which in turn radiate photons again. This process results in a shower of electrons and photons, growing exponentially, and stopping when the photons reach energies of $2 \cdot m_e$ or less and do not have enough energy for pair production. The remaining electrons and photons still deposit energy via bremsstrahlung, ionization and Compton scattering. The resulting radiation can be detected and amplified, e.g. using photo-multipliers.
Hadrons are heavier than electrons and take longer to deposit their energy via bremsstrahlung (neutral hadrons do not emit any bremsstrahlung at all, of course). They deposit most of their energy in the second part of the calorimeter, the hadronic calorimeter, where they form showers similar to the electrons. The shapes of the showers differ because hadrons mainly interact strongly with the atomic nuclei. During those interactions, other hadrons such as pions, kaons or protons can be produced. Some of them (e.g. neutral pions) decay electromagnetically, causing small electromagnetic showers inside the hadronic shower. This makes hadronic calorimetry more difficult than electromagnetic calorimetry and is one cause of the uncertainties on jet energies.
Muons are heavier than electrons and do not interact strongly. Most muons produced at the LHC will have energies between $1\,\text{GeV}$ and $1\,\text{TeV}$. They are so-called minimum ionizing particles, which means they deposit little energy in the calorimeters (up to a few GeV per muon). Muons are the only particles reaching and interacting with the outermost detector layers, the muon chambers, which are tracking chambers similar to those in the inner detector. If they are surrounded by a magnetic field, they can be used to measure muon momenta.
Neutrinos only interact weakly with matter. They leave no tracks in the inner detector and do not deposit any energy in the calorimeters. However, they can be detected indirectly: The magnitude of the vector sum of the transverse energies of all "visible" particles is defined as the *missing transverse energy* $\not{E}_T$. In hadron collisions, we do not know the initial state of the partons before the collision as we do not know their momentum fraction x. However, we can assume that their transverse momentum is negligible. If all particles in the final state are detected, the transverse energy should be balanced and the missing energy is zero (or close to zero, accounting for detector inefficiencies). If the missing energy is not zero, one knows that there was at least one undetected particle, e.g. a neutrino, that caused this imbalance. As we do not know

the longitudinal momentum of the partons in the initial state and we cannot measure the longitudinal momentum of the proton remnants in the final state, we can not use longitudinal missing energy. As the whole system may be boosted along the beam axis, projections to the transverse plane are often used as they are invariant under such boosts.

3.2. Important Physical Quantities

In this chapter, some physical quantities and coordinates that are often used in the description of high-energy particle physics experiments will be introduced.

3.2.1. Luminosity, Counting Rate and Cross Section

The luminosity L describes the flux density of particles in the beam. For synchrotrons it is given by

$$L = \frac{n_B \cdot f \cdot n_1 \cdot n_2}{A}. \tag{3.1}$$

where f is the synchrotron frequency, n_B is the number of bunches per beam, n_i is the number of particles per bunch in beam i and A is the effective bunch cross section at the interaction point [25]. However, determining the actual luminosity is not that trivial, especially for hadron colliders. In most cases, the luminosity is actually measured using eq. (3.2) and a process with a well known cross section. The integrated luminosity $L_{int} = \int L \mathrm{d}t$ is just the luminosity integrated over a certain period of time.
For each possible reaction, the cross section $\sigma(\sqrt{s})$ is a measure of the probability of that reaction happening. It can be calculated from Feynman rules and the available phase space.
Luminosity, cross section, and interaction rate $\frac{\mathrm{d}P}{\mathrm{d}t}$ (for a given process) are related by the formula

$$\frac{\mathrm{d}P}{\mathrm{d}t} = \sigma \cdot L. \tag{3.2}$$

The counting rate $\frac{\mathrm{d}N}{\mathrm{d}t}$ is again related to the interaction rate by a factor ϵ_{eff}, which depends on the acceptance of the detector as well as the efficiencies of the trigger, the reconstruction algorithms and the cuts used (see section 5.5.1).

3.2.2. Detector Coordinates

Because of the layout of the ATLAS detector, cylindrical coordinates are used to describe the positions and momenta of particles inside of it [26]. The z-axis follows the beam direction, so the $x - y$ plane (transverse plane) is perpendicular to the beam. The origin is located at the center of the detector at the planned interaction point. The x-axis points to the center of the LHC ring, the y-axis points upward. The azimuthal angle φ is measured in the transverse plane with respect to the x-axis, the polar angle θ is measured with respect to the z-axis. Instead of the polar angle, the pseudorapidity $\eta := -\ln\left(\tan\left(\frac{\theta}{2}\right)\right)$ is used. In the relativistic limit (i.e. for $\frac{m}{E} \ll 1$), this quantity is equal to the rapidity $y = \ln\left(\frac{E+p_z}{E-p_z}\right)$, which is is only affected by Lorentz boosts along the z-axis through an additive constant. The distance $\Delta\eta$ between two objects is then Lorentz-invariant (for boosts along the z-axis).
The angular distance ΔR between two objects is defined as $\Delta R = \sqrt{\Delta\eta^2 + \Delta\varphi^2}$.

3.3. The LHC

The Large Hadron Collider (LHC) is a proton-proton collider that started operating in winter 2009. In 2011, it operated at a center of mass energy of 7 TeV and is expected to eventually reach energies around 14 TeV at a design luminosity of $10^{34}\,\mathrm{cm}^{-2}\mathrm{s}^{-1}$ [27]. The protons are accelerated and brought to collision in bunches of up to $1.15 \cdot 10^{11}$ protons. The LHC can store and accelerate up to 2808 bunches per beam [27]. The beam tunnel has a circumference of 27 km and was previously used for the Large Electron-Positron Collider (LEP). The four main experiments are ATLAS, CMS, LHCb and ALICE.
As it is the particle collider with the highest center of mass energy to date, the LHC focuses on searching for new or unobserved physics, for example the predicted Higgs boson or hypothetical supersymmetric partners to known matter. There are also precision measurements of standard model quantities. In addition to proton-proton collisions, lead ion collisions are used to study the properties of quark-gluon plasma.

3.4. The ATLAS Experiment

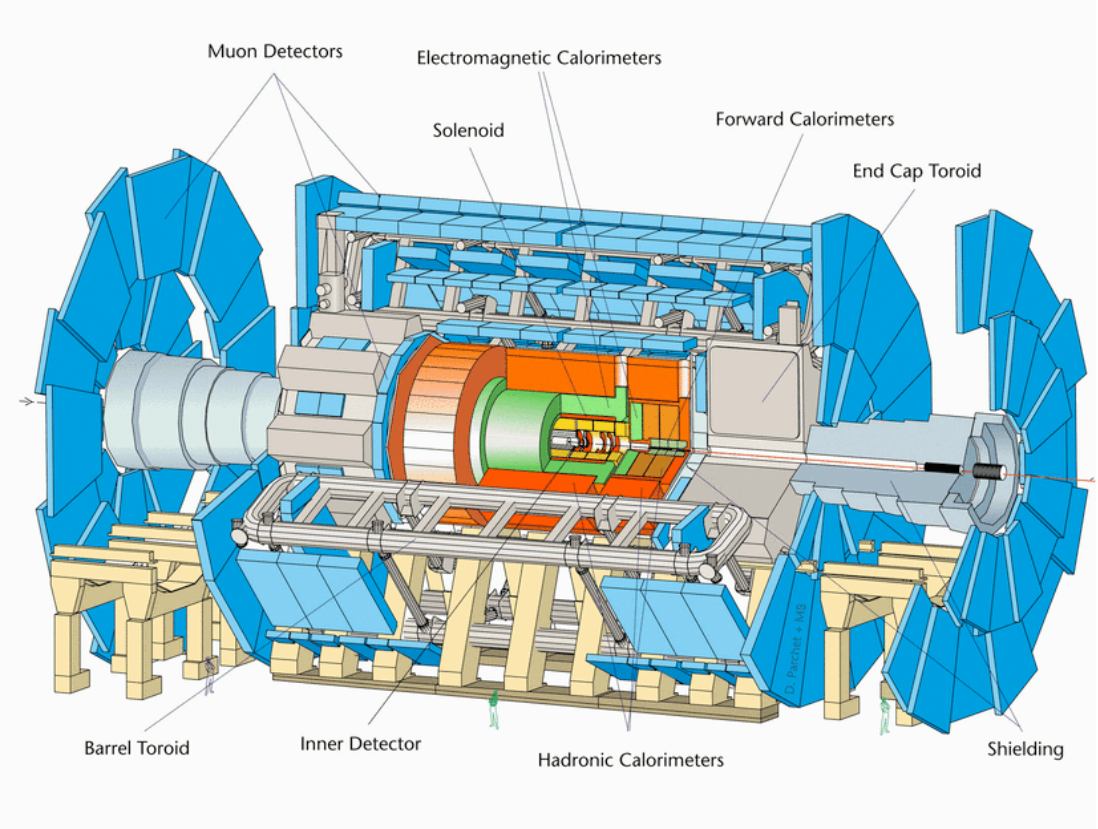

Figure 3.1.: The ATLAS experiment.

3.4.1. Design of the Detector

The ATLAS (A Toroidal LHC Apparatus) detector is one of the two multi-purpose detectors at LHC. For an in-depth discussion of its design, see [26]. It is composed of an inner detector inside a 2 T solenoidal magnetic field, electromagnetic and hadronic calorimeters and muon chambers. Its design is shown in Fig. 3.1.

The inner detector consists of the pixel detector, the silicon strip detector (SCT) and the transition radiation tracker (TRT). In the pixel detector, the approximately 80 million pixels are arranged in three barrel layers and six endcap disks. The closest barrel layer is only about 50 mm from the beam pipe. Following the pixel detector, the silicon strip detectors are arranged so that each track crosses eight strip layers. Charged particles will leave a small amount of energy in each pixel/strip layer, which can be used to re-

construct the particles' tracks. From the measurements of the curvature of these tracks in the magnetic field, the momenta of the particles with an absolute pseudorapidiy of up to 2.5 can be reconstructed. The TRT, made up of about $350,000$ "straw tubes", measures radiation that is produced when a charged particle crosses between two regions with different permittivities. This allows for the determination of the particle's velocity. It can therefore be used to distinguish between electrons and charged pions by way of determining a particles mass if its momentum has been measured independently.
There are two calorimeter layers (electromagnetic and hadronic). Electrons and photons deposit their energies in the inner layer, the electromagnetic calorimeter. This is constructed as a sampling calorimeter, using lead as an absorber and liquid argon as a sampling medium to measure the deposited energy. It has a barrel part and two endcap parts, covering a pseudorapidity region of up to 3.2. The liquid argon electromagnetic calorimeter is followed by the hadronic calorimeter, also a sampling calorimeter. In the endcap regions, the hadronic calorimeter uses liquid argon as well, but copper as the absorber. In the barrel region, it uses scintillating fiber tiles as the sampling medium and steel as the absorber. ATLAS also has two copper-tungsten/liquid argon forward calorimeters, covering a pseudorapidity range of up to 4.9. There are approximately $200{,}000$ readout channels from all of the calorimeters.
The muon system is immersed in a toroidal magnetic field to be able to reconstruct the muon momentum. There are four different kinds of muon chambers: Monitored Drift Tubes (MDTs) and Resistive Plate Chambers (RPCs) in the barrel region, as well as Cathode Strip Chambers (CSCs) and Thin Gap Chambers (TGCs) in the endcap regions. The RPCs and TGCs have fast readout times and are mainly used for triggering (see below) while the MDTs and CSCs are used for precision tracking. The muon chambers are arranged so that each muon passes through several chambers, allowing for the determination of the muon's momentum and charge.

3.4.2. Trigger System

Reading out the full ATLAS detector at each bunch crossing would lead to data rates that are too high to be able to be saved or analyzed. Apart from that, most events are expected to be simple QCD scattering events. "Interesting" physics makes up only a fraction of the reactions taking place. Because of these two facts, a trigger system is needed. ATLAS employs a three level trigger system (L1, L2, and event filter). Its

task is to select "interesting" events to reduce the recorded data rate to a manageable amount.

The *L1 triggers* look for high-p_T objects in certain regions of the detector, using muon chambers and calorimeter information. From their decisions, so-called *Regions of Interest* are identified which the *L2 trigger systems* investigate further. The *event filters* have access to information from all parts of the detectors, with simplified reconstruction algorithms. Their output rate is about $200\,\text{MHz}$, which is low enough to be written to tape for further offline analysis.

If the rate of triggered events is too high, a trigger may be *prescaled*, meaning that it only "fires" with a given probability (less than one) each time its conditions are fullfilled. This ensures a relatively unbiased recording of events.

There is a large menu of different triggers, to accomodate as many analysis groups as possible. Common trigger object are single high-p_T leptons, but there are also triggers that require several detector objects, like for example dielectron triggers, triggers on several high-p_T jets or on missing transverse energy. The benefit of using for example a dielectron trigger instead of a single electron trigger is that one can set lower p_T limits while keeping the output rate low.

3.4.3. Object Reconstruction

The full reconstruction of the event is done offline. *Vertices* are reconstructed using the track information from the inner tracker, projecting the tracks back to the beam axis. If several vertices are reconstructed, the one with the highest sum of track p_T^2 is classified as the *primary vertrex*.

Electrons are reconstructed from clusters in the electromagnetic calorimeter, with certain requirements on the shower shape, matched to a track in the inner detector to distinguish them from converted photons.

Jets of hadronic particles are reconstructed from clusters in the electromagnetic and hadronic calorimeters, which are sequentially combined into jets using so-called *jet algorithms*. The jets used for the analysis in chapter 6 were reconstructed using the anti-k_T algorithm (cf. [28]). Tracks pointing into the jet area are associated to the jets. Not all of the energy deposited in the calorimeter by hadronic jets is detected. The mean calorimeter response or *jet energy scale* has to be measured and calibrated. This is done both with test beams and in-situ methods[1]. It has been measured with an un-

[1] For more details, see [29].

certainty of less than 10% for the jets used in chapter 6, i.e. with a p_T of more than $30\,\text{GeV}$ and an absolute pseudorapidity less than 2.5. There are tools available inside the ATLAS collaboration that apply rescaling of the jet energies, and can also correct simulated jets to have the measured resolution.
Muons are reconstructed from tracks in the muon system, and possibly the inner detector.
The vectorial transverse energy deposited in the calorimeters, corrected for the energy of reconstructed objetcts[2] is added up. Its inverse is the missing transverse energy.
Due to the high rate of collisions in the detector, the reconstruction is complicated by pile-up, meaning the presence of objetcs in the detector that do not stem from the proton-proton collision in question, i.e. the one that was triggered on. Since "interesting" reactions are quite rare, most of these extraneous objects are hadrons from elastic/inelastic proton scattering. Their presence in the detector needs to be accounted for carefully, as it highly depends on run conditions like the rate of bunch crossings.
There are two sources for pile-up. The first, called out-of-time pile-up, is caused by particles produced during different bunch crossings being present in the detector at the same time. This can be suppressed by tight cuts on the timing of reconstructed signals. The second, called in-time pile-up, is caused by multiple interactions in the same bunch crossing. This can be suppressed by requiring charged leptons to come from the same primary vertex. To reduce the effect of pile-up on jets, the *jet vertex fraction* (jvf), the p_T-weighted fraction of tracks coming from the dominant primary vertex in the event, is introduced. Jets with too low a jvf can be removed. Remaining jets are corrected for mean pile-up activity, depending on run conditions.

[2] e.g. muons, which only deposit a small amount of their energy in the detector

4. Experimental Methods and Challenges

In the following chapters, methods to study the $H^{\pm}W^{\pm}Z$ vertex will be discussed. They all involve the observation of a charged Higgs decaying into a W and a Z boson with the ATLAS detector at the LHC, mostly in the $q\bar{q}'l^+l^-$ final state.
The process to be studied, $H^{\pm} \rightarrow W^{\pm}Z \rightarrow q\bar{q}'l^+l^-$, can obviously not be fully observed in the detector. Only the final decay products are accessible by experimentators. Their detection and the measurements of their properties are described in section 3.4.3. This detection is not one hundred percent accurate or efficient, which propagates to the final results.
Another problem is the fact that there are lots of other processes, some with a much higher cross section, that can have similar signatures in the detector as our signal process. These processes are referred to as "background". Some of this background can be removed during the analysis by using appropriate cuts that retain most of the signal (*reducible background*, e.g. leptons from mesonic decays can be removed by requiring leptons to be isolated in the detector). Others remain as *irreducible background*. There are different methods to treat this problem. The one employed here will be a mixture of additional requirements on some of the objects in the events (preselection cuts) and a multivariate method, boosted decision trees (see [30]), explained in section 4.1. In section 4.2, a procedure for setting limits on physical quantities is explained, with a focus on limits on cross sections from counting experiments.

4.1. Boosted Decision Trees

4.1.1. Manual Cut & Count

In traditional cut-based analyses, one develops and applies a series of requirements ("cuts") to the recorded events that are designed to let most of the signal pass while getting rid of most of the background events. One then estimates the number of background events passing all cuts using Monte Carlo simulations and measurements in background-dominated control regions, and compares this to the number of observed events. These methods work well for processes where the background can be easily reduced. However, by the "naive" cutting procedure, generally only simply connected, convex regions in the space of observables can be selected. This is not always optimal, since the signal might be distributed over several regions in the space of observables.

Especially for processes with a small number of expected signal events and a lot of background, such as when trying to discover a previously unobserved process or particle, it is useful to consider more versatile methods. Instead of a linear series of cuts, it is often necessary to use a *decision tree*. Each of the nodes in this tree contains a condition on one (or several) observables, and has two children. Each event starts at the top of the tree. For each node, the condition is evaluated and the event is moved to one of the children nodes, depending on whether or not it fulfills the condition. Finally, the ratio of expected signal and background events in each leaf is calculated using simulations. One can now e.g. assign each leaf as "background" or "signal" leaf and compare the observed number of events in the signal leaves to the expectation from background simulations. Effectively, one has replaced the fixed series of cuts by one where the cuts depend on the cuts that were passed/failed before. This approach is more versatile and allows to select more complex regions in the space of observables. The "naive" cut approach is retained as a special case where all nodes of a given depth contain the same cuts.

4.1.2. Optimal Decision Trees

The usefulness of both the "naive" cut method and the use of decision trees depend on the selected observables and cut values. However, for complex final states and several

background processes, it is not trivial to identify *optimal* or even *good* cuts[1]. It becomes necessary to automate the creation of the decision tree. More precisely, one uses an algorithm to generate an optimal decision tree, given a set of observables and a measure of separation power, as described e.g. in [30]. One common such measure is the *gini-index*, which is defined as follows. Given a training sample containing signal events with weights $w_{s,i}$ and background events with weights $w_{b,i}$, one defines the *purity* of a given node as

$$P = \frac{\sum\limits_{S} w_{s,i}}{\sum\limits_{S} w_{s,i} + \sum\limits_{B} w_{b,i}},$$

where the sums run over all signal resp. background events in the node. The gini-index for that node is now defined as

$$gini = \left(\sum_{S} w_{s,i} + \sum_{B} w_{b,i} \right) \cdot P \cdot (1 - P) = \frac{\left(\sum\limits_{S} w_{s,i} \right) \cdot \left(\sum\limits_{B} w_{b,i} \right)}{\sum\limits_{S} w_{s,i} + \sum\limits_{B} w_{b,i}}.$$

The algorithm starts with one empty node. For each node, the observable and cut value are selected that minimise $gini_{\text{left child}} + gini_{\text{right child}}$, i.e. that give the best separation power for the events that will pass by this node. If $gini_{\text{father}} \leq gini_{\text{left child}} + gini_{\text{right child}}$, the split tree would provide worse separation power than the unsplit one. In this case, the node is not split further and declared a leaf. Otherwise, the tree is split and the splitting procedure is repeated for each child node.
After the splitting procedure has terminated, each leaf is either assigned as "signal" if its purity is greater than a certain cutoff value, or "background" if it is not.

4.1.3. Boosting the Decision Trees

The method of training decision trees as described above was found to be powerful, but quite unstable, meaning that small changes in the training sample can lead to a large change in the discriminator. To alleviate this, a method was developed to train a large number of decision trees, building on the ones created previously. During this training process, events that were miss-classified by earlier trees are given a higher weight for future iterations. This is referred to as "boosting", the resulting trees are referred to as

[1] "Optimal" cuts are here somewhat vaguely defined as the ones to give us the maximal chance of discovery or the most precise estimator for the cross section for a given process/experiment.

boosted decision trees (BDTs). Each tree is also given a weight depending on the rate of miss-classifications.

One common boosting algorithm is AdaBoost [31]. For a given decision tree, one first defines the (weighted) miss-classification fraction

$$err = \frac{\sum_{\text{miss-classified events}} w_i}{\sum_{\text{all events}} w_i}.$$

The tree is then assigned the weight

$$\alpha = \beta \cdot \ln\left(\frac{(1-err)}{err}\right),$$

where β is a free parameter of the algorithm. Each miss-classified event is then re-weighted by the factor $\exp(\alpha)$. Then all events are reweighted by a common factor so that the sum of all weights is the same as before.

For the final classification, each event will be passed through all trees. If it is classified as signal (background), it is assigned a score of 1 (-1). From the scores of all produced decision trees, a final discriminant ("response") is calculated as the weighted average of the individual scores (weighted by the tree weights α). By definition, this variable peaks at higher values for signal events than for background events. However, there is generally some overlap. One can now cut on this value and count the expected background/observed data events as before, or fit the background/signal contribution (from simulations) to the observed BDT response.

Due to the pseudo-random nature of available simulations, it might happen that the BDT response becomes sensitive to apparent features in the signal (or background) that turn out to be statistical fluctuations. To check whether this "overtraining" happened and how much it influences the results, one usually divides the Monte Carlo samples in two parts. The first is used for the training as described above, the second for validation/checking. If the discriminant performs much worse on the second sample, one needs to either generate more simulation events or change parameters of the particular implementation of the training/boosting code to obtain a more stable (but possibly less efficient) discriminator, e.g. by limiting the number of nodes per tree. A detailed treatment of boosted decision trees and their application to an analysis of data recorded by the Miniboone experiment can be found in [30].

For this work, the TMVA [32] package was used to train, test and evaluate the trees. TMVA integrates into the ROOT framework and provides customisable interfaces to a variety of multivariate classifiers, like boosted decision trees.

4.2. Limit Setting

The interpretation of measurements done at modern high-energy physics experiments is not a straight-forward process. This is due to two factors:

1. Due to the probabilistic nature of the available theories of elementary particles, we can only predict the *probability* of a certain process to happen or the *distribution* of certain observables like energy and momentum of decay products, not how often the process actually takes place and in what directions the decay products move. This can be alleviated by recording a large number of events.

2. Each measurement has a certain uncertainty due to finite resolutions, inefficiencies etc., even with the best possible detector calibration.

To ensure a consistent treatment of these uncertainties, one has to ask very precise questions that can be answered in a statistical sense. Usually they can be formulated as "Is a given hypothesis $H(\alpha)$, depending on some parameters α, consistent with observations?" or "How probable are our observations, given $H(\alpha)$?". More details on statistics and the different interpretations of such measurements can be found e.g. in [33]. Here, we follow a mostly frequentist interpretation, i.e. drawing conclusions about the probability of a given outcome for a fixed hypothesis. The opposing approach is the Bayesian one, drawing conclusions on the probability or credibility of a theory, given some observations.
The kind of measurements that are treated here deal with discovering/setting limits on the production of a new particle. Here, there are two hypotheses that have to be considered. The first one is the standard model, "background only" hypothesis H_b, usually depending on parameters like cross sections of the different background processes. Uncertainties of the measurement process may be inserted here as "nuisance parameters". The second one is the "signal+background" hypothesis H_{s+b}, indicating new physics, depending on the same parameters and the expected signal cross section. To set a lower limit on the cross section σ of a new physics process, H_{s+b} will be taken to depend on this cross section. Then we can ask "For which values of σ is $H_{s+b}(\sigma)$

consistent with the observations? For which values of σ is $H_{s+b}(\sigma)$ not consistent with H_b?".

4.2.1. Hypothesis Testing

The treatment here will mostly follow [7, 33]. In general, an experiment will collect several observables. It is usually useful to combine them into one final *test statistic* Q, e.g. the number of events passing certain criteria for a counting experiment. In the following, Q will be taken to be larger for more "signal-like" samples. Otherwise, some of the signs will change.
For each hypothesis H, the probability density $g(Q|H)$ of the test statistic Q has to be calculated. Then, one chooses a range in Q so that the probability of measuring a value inside of this range, given that H is true, is at most α. H is said to be rejected with *significance* α if one measures Q inside this region. Now consider a counting experiment aiming at constraining new physics with an a priori unknown cross section. One obtains an infinite number of signal (plus background) hypotheses, $H_{s+b}(\sigma)$, depending on the signal cross section, and the background (only) hypothesis $H_b = H_{s+b}(\sigma = 0)$. The probability densities are given by Poisson distributions, convoluted with a Gaussian to account for systematic uncertainties. A given signal hypothesis should be rejected if $P(Q \leq Q_{obs}|H_{s+b}(\sigma)) := \int_{-\infty}^{Q_{obs}} g(Q|H_{s+b}(\sigma)\mathrm{d}Q \leq \alpha$, i.e. if the probability of measuring at most as many events as were observed is smaller than some chosen value, usually 0.05. (The background hypothesis should be rejected in the opposite case, if $P(Q \geq Q_{obs}|H_0) \leq \alpha$.) The probability of falsely rejecting a signal hypothesis is given by α. The quantity $1 - \alpha$ is called *confidence level*.
This method performs well for signal hypotheses that are well separated from the background hypothesis. But for small signal cross sections, signal hypotheses that the experiment is not sensitive to might still be rejected due to downward fluctuation of observed data.

4.2.2. The CL_s Method

One suggested way to mitigate this is the CL_s method [7, 34, 35]. Given a test statistic Q and a hypotheses H as above, one defines

$$CL_{s+b}(\sigma) = P(Q \leq Q_{obs}|H_{s+b}(\sigma)),$$

and

$$CL_b = P(Q \leq Q_{obs}|H_0).$$

Here, small values of CL_{s+b} indicate that the observations are not compatible with a given signal hypothesis. Very small values of CL_b indicate large downward fluctuations of the background or possible underestimation of systematic uncertainties. Values of CL_b close to one can be caused by large (upward) background fluctuations, underestimation of systematic uncertainties, or presence of signal events. To quantify this further, one introduces

$$CL_s(\sigma) := \frac{CL_{s+b}(\sigma)}{CL_b}.$$

A given signal hypothesis is considered rejected if $CL_s \leq \alpha$ for a given value α. This automatically takes the experiment's sensitivity to a given hypothesis into account. For small signal cross sections, CL_b will decrease if CL_{s+b} decreases, meaning that signal hypotheses to which the experiment is not sensitive are not rejected.
Obviously, $CL_s \leq CL_{s+b}$ in all cases. Thus, the condition on CL_s is stricter than the one for the simple hypothesis test. This means that the CL_s method is conservative, i.e. the probability of falsely excluding a true signal hypothesis is actually *smaller* than α.

4.2.3. Expected and Observed Limits

To set limits on the cross section of a new physics process, one now checks all possible signal hypotheses against the measured data. The lowest value of σ for which the signal hypothesis cannot be rejected is called the *observed upper limit* with a confidence level of $1 - \alpha$ on the cross section of this process, meaning that if the true cross section was in fact larger than this value, the probability of it being falsely rejected is less than α.
This can be compared to the *expected upper limit*, obtained as the mean of the observed exclusion limit of an ensemble of Monte Carlo simulations, where the "observed" number of events follows the background-only hypothesis. Expected and observed exclusion limits are often normalised by the predicted cross section of a certain model. If the expected upper limit is larger than the predicted cross section, that means that the experiment is not sensitive to this model. If the expected upper limit is lower than the predicted cross section, the experiment is sensitive to the model. If the observed upper

limit is also smaller than the predicted cross section, that specific model is excluded. If the observed upper limit is significantly larger than the expected limit and at least as large as the predicted cross section, this might be seen as a hint that the model is true.

5. Phenomenological Studies and Results

In this chapter, an understanding of the phenomenology of the $H^{\pm} \to W^{\pm}Z$ process at hadron colliders is developed. This is an important step that needs to be done before the search for such a process. Studies with simulated (Monte Carlo) signal events and a crude detector simulation are performed to study production modes, possible selection cuts, reconstruction of the charged Higgs mass from the kinematics of the decay products, and determination of its spin using angular variables. Not all of these studies have been implemented on data so far, and they still offer insight into possible future search efforts.
The results described in this chapter were obtained during my work with the THEP group at Uppsala Universitet, as part of my "Spezialisierungspraktikum" and "Forschungshauptpraktikum" (in preparation for my Master's thesis).
Most of the analysis in this and the following chapter was done using the ROOT framework developed at CERN.

5.1. Event Generation

For the generation of signal events, `MadGraph/MadEvent` [36, 37] (MadGraph/-MadEvent version 4.5.1, PyPgs version 2.1.8) is used together with packages based on `pythia` [21] (providing showering and hadronisation) and `pgs` [23] (providing a fast detector simulation, with an acceptance/resolution comparable to the ATLAS detector design parameters). The latter two programmes are called automatically from `MadGraph` depending on the configuration, with necessary parameters specified in so-called "run cards".

5.1.1. Signal Events

The purpose of this project is to study the $H^{\pm}W^{\pm}Z$ vertex, which does not exist in the standard model or the most common extension, the MSSM, and other two-Higgs-doublet models, and hence is not implemented in any of the standard MC generators. To be able to generate events containing this vertex, it has been added by hand into the existing 2HDM model file in `MadGraph`. As motivated in 2.4.1, a vertex with a purely scalar coupling has been added to the relevant subroutine. The form factor F described above is set to unity so as to stay relatively model-independent. The cross sections can be manually rescaled according to the predictions of the specific models to be studied.
The $H^{\pm} \to W^{\pm}Z$ decay channel is added to `pythia` via the `pylha` interface, which is automatically called from `MadGraph`. The branching ratio for this decay is set to 1, since this is the only decay of interest. The branching ratios for the leptonic/hadronic decays of the W and Z bosons are also set using the same interface, to obtain only the final states of interest.
The width of the charged Higgs boson is initially set to a very low value (1 MeV). However, later on, the width of the charged Higgs is also calculated using `MadGraph` and studies are done involving off-shell Higgs bosons.

5.1.2. Production Chain

The first step in the event production is to let `MadGraph` generate the Feynman diagrams contributing to the process to be studied. This is done by specifying the initial and final state, and any intermediate particles if necessary. `MadGraph` finds all contributing tree diagrams (loop diagrams are not included). Once that is done, one can ask `MadGraph` to calculate the cross section and generate events. `MadGraph` is configured to produce charged Higgs bosons (via W/Z boson fusion and via associated production, see below). The produced events are then automatically fed into `pythia`, which handles the decays of the Higgs, W and Z as well as showering/hadronisation of the quarks. It is possible to do the Higgs and even the W/Z decays within `MadGraph`. However, this takes a lot of time to run due to the large number of final state particles, hence this is considered impractical. After `pythia`, `pgs` is called to provide a crude detector simulation. Hadrons are clustered into jets, the momenta of visible objects (electrons, muons, jets) are smeared. Objects outside of the detector acceptance are

dropped and the rest are used to calculate the missing transverse energy.
After each stage in the production chain, the results are saved in the "lhe" format [38] and also copied into ROOT trees, for easy analysis.
The masses of the Higgs bosons are not known and generally not predicted by theory. There are bounds from direct searches as well as theoretical predictions using loop contributions to variables measured in electroweak precision measurements. These bounds and predictions are of course highly model-dependent. Most seem to favour Higgs masses in the range of several $10\,\text{GeV}$ to $1\,\text{TeV}$. Only decays of a charged Higgs boson into real W and Z bosons are considered here. Hence, only Higgs masses above the kinematic threshold of $m_W + m_Z \approx 172\,\text{GeV}$ are considered. All simulations are performed for seven different Higgs masses between 180 and $600\,\text{GeV}$. In the following, "low Higgs mass" will refer to Higgs masses just above the threshold, i.e. around $180 - 200\,\text{GeV}$.

5.2. Production Cross Section

There are several different production channels for the charged Higgs in a proton collider. To stay model-independent, I have focused on production mechanisms that do not involve couplings of the charged Higgs to fermions or neutral Higgs bosons. To achieve this, all relevant couplings (e.g.. H^+tb) are set to zero. The production channels that are investigated further are associated production of $H^\pm$ and $W^\pm/Z$, and vector boson fusion (VBF). Pair production via γ/Z is investigated briefly but does not contribute much.

5.2.1. Electroweak Pair Production

There are again several processes where a H^+H^- pair is produced. The only ones that do not depend much on the particular model and the other Higgs masses/couplings are pair production via an s-channel photon or Z boson (cf. Fig. 5.1a). The coupling of γ/Z to the charged Higgs is fixed, hence the cross section for this process only depends on the mass of the charged Higgs. The expected production cross section for the LHC running at $7\,\text{TeV}$ can be seen in Fig. 5.1b. As expected, it decreases for larger Higgs masses. But even for relatively small Higgs masses the cross section is so low ($7.7\,\text{fb}$ for $m_{H^\pm} = 180\,\text{GeV}$) that looking for these events at the LHC (running at $7\,\text{TeV}$) will

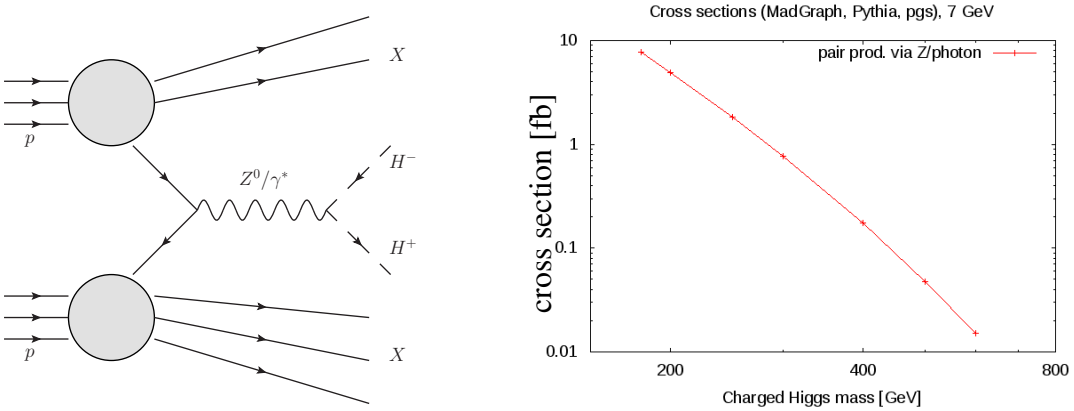

(a) **(b)**

Figure 5.1.: Left: Leading order Feynman diagram for charged Higgs pair production via s-channel photon. Right: Expected pair production cross section for production at a 7 TeV proton-proton collider for different Higgs masses, assuming $|F| = 1$.

probably prove futile: For an integrated luminosity of $1\,\text{fb}^{-1}$ one would expect less than ten Higgs pairs to be produced that way.

5.2.2. Vector Boson Associated Production

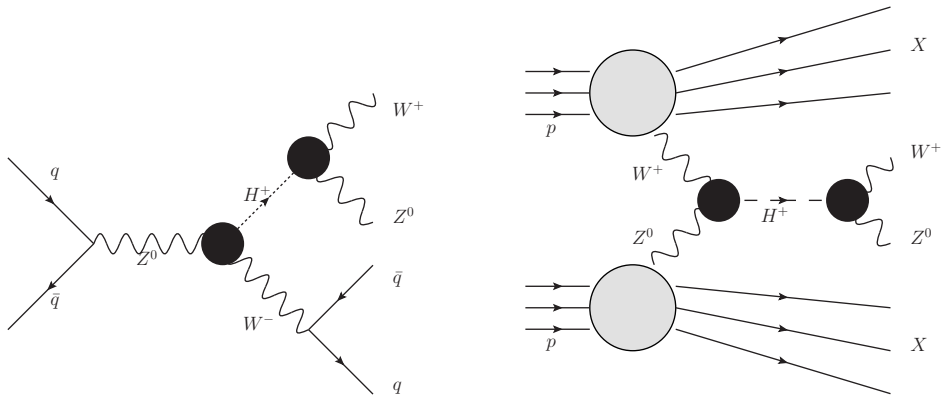

(a) **(b)**

Figure 5.2.: Left: Leading order Feynman diagram for charged Higgs production in association with a vector boson in the s-channel. Right: Leading order Feynman diagram for charged Higgs production in vector boson fusion.

In a theory containing the $H^\pm W^\pm Z$ vertex, charged Higgs bosons may be produced in association with a $W\pm$ (Z) boson via an s-channel off-shell Z ($W\pm$) boson (cf.

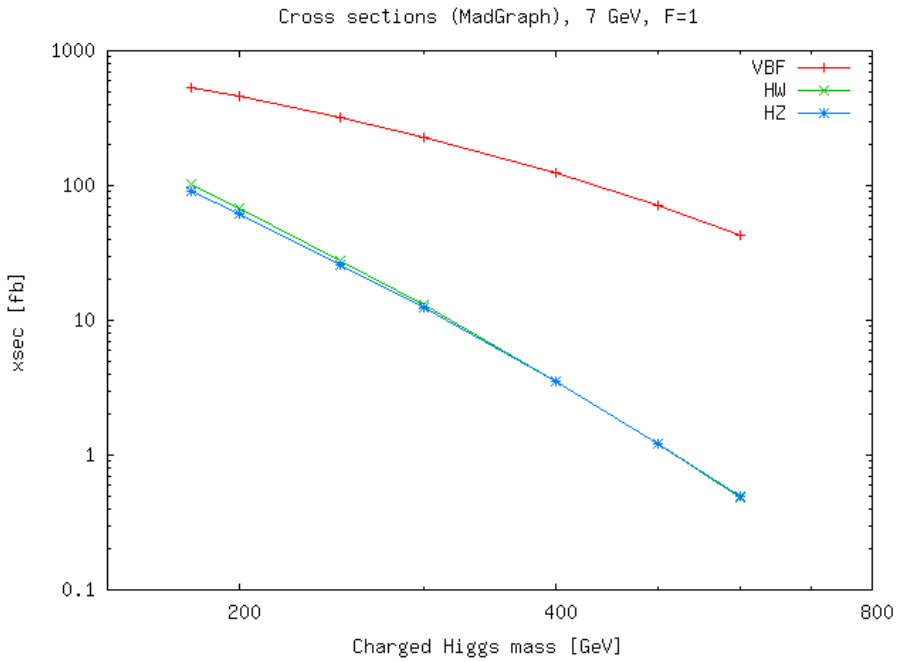

Figure 5.3.: Expected charged Higgs production cross section for the VBF (vector boson fusion), HW ($H^{\pm}$ and $W^{\mp}$ associated production) and HZ ($H^{\pm}$ and Z associated produced) processes, at a 7 TeV proton-proton collider, for different Higgs masses, assuming $|F| = 1$.

Fig. 5.2a). The cross section for this process then depends on the coupling constant associated with this vertex. In Fig. 5.3 the cross section calculated with `MadGraph` as described in 5.1.1 is shown, with the model-dependent form factor set to 1. (In models where the vertex only comes in via loops, the cross section is thus much lower than shown here.)

Again, the cross section decreases quickly with increasing Higgs mass. The cross section for both processes ($W^{\pm} \to H^{\pm}Z$ and $Z \to H^{\pm}W^{\mp}$) are of the same order of magnitude. Even for low Higgs masses, the cross section is less than 100 fb for each process.

5.2.3. Vector Boson Fusion

There is another way to produce a single charged Higgs via the $H^{\pm}W^{\pm}Z$ vertex: Vector boson fusion (cf. Fig. 5.2b). As in the case of neutral Higgs production, this process dominates over associated production with a vector boson (cf. Fig. 5.3). Since both processes contain the $H^{\pm}W^{\pm}Z$ vertex exactly once, their cross sections have to be multiplied with the same model-dependent form factor, so their ratio is (at leading

order) model-independent.
The cross section for the vector boson fusion process decreases less sharply with the Higgs mass than the associated production cross section does. For low Higgs masses, the cross section can reach several hundred fb, which means that this process could be observed at the LHC.
Vector boson fusion has a great advantage over most other production mechanisms: Since only colour singlets are exchanged between the two protons, there is no color connection between the beam remnants and hence one expects little hadronic activity in the central region (of course there will still be some due to hadronic decays, the underlying event and multiple interactions).

5.3. Decay

Process	Branching ratio	Process	Branching ratio
$W^+ \to e^+\nu_e$	$(10.75 \pm 0.13)\%$	$H^\pm \to e^+e^-q\bar{q}'$	$(2.27 \pm 0.01)\%$
$W^+ \to \mu^+\nu_\mu$	$(10.57 \pm 0.15)\%$	$H^\pm \to \mu^+\mu^-q\bar{q}'$	$(2.27 \pm 0.01)\%$
$W^+ \to q\bar{q}'$	$(67.60 \pm 0.27)\%$	$H^\pm \to e^+e^-e^+\nu_e$	$(0.362 \pm 0.004)\%$
$Z^0 \to e^+e^-$	$(3.363 \pm 0.004)\%$	$H^\pm \to e^+e^-\mu^+\nu_\mu$	$(0.355 \pm 0.005)\%$
$Z^0 \to \mu^+\mu^-$	$(3.366 \pm 0.007)\%$	$H^\pm \to \mu^+\mu^-e^+\nu_e$	$(0.362 \pm 0.004)\%$
$Z^0 \to q\bar{q}$	$(69.91 \pm 0.006)\%$	$H^\pm \to \mu^+\mu^-\mu^+\nu_\mu$	$(0.356 \pm 0.005)\%$

Table 5.1.: W, Z, and charged $H^\pm$ boson decays, assuming BR($H^\pm \to W^\pm Z$)=1, excluding τ. From [7].

As explained above, only decays of the charged Higgs into a $W^\pm$ and a Z boson are considered. The decays can be further classified according to the decays of the weak bosons. Some factors should be considered when choosing decays channels for further studies:

- Hadronic decays of the weak bosons have a larger branching ratio than leptonic decays (cf. Tab. 5.1).
- Muons and to some degree electrons can be detected and reconstructed better and more precisely than jets.
- At least one lepton in the final state makes it easier to trigger on the desired events.
- In events with leptonically decaying W bosons, as well as events containing τ leptons, some information will be lost due to neutrinos carrying away momentum.

Only decay channels where the Z boson decays into electrons or muons are chosen to be used here. Both leptonic and hadronic decays of the W boson are considered. The resulting branching ratios can be found in Tab. 5.1.

5.4. Finite Width

In the simulations described above, `MadGraph` is configured to generate on-shell Higgs bosons. Their width is assumed to be negligibly small (1 MeV). However, it is

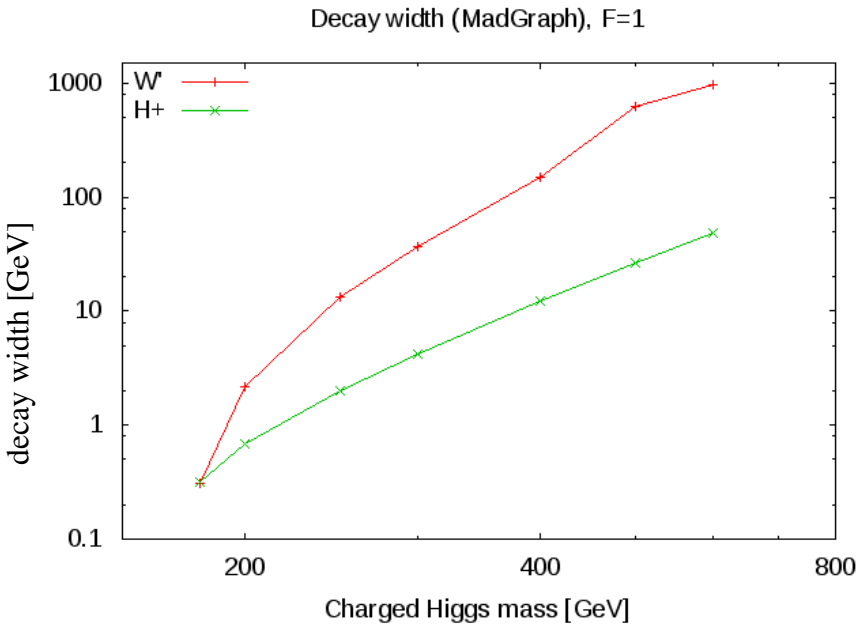

Figure 5.4.: Predicted decay width in GeV of a charged Higgs boson of a given mass (green), compared to the partial width of a hypothetical heavy gauge boson decaying in the same manner ($W' \rightarrow WZ$) (red).

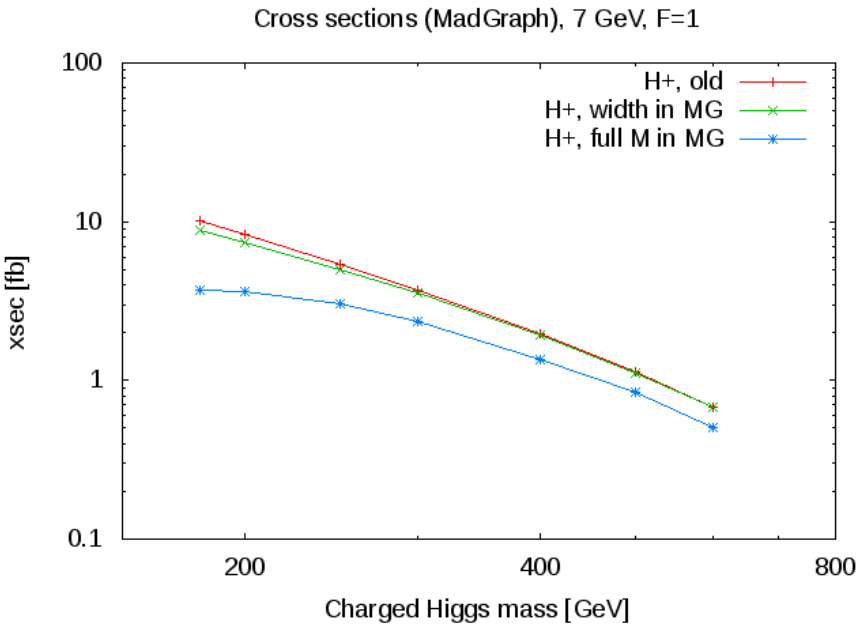

Figure 5.5.: Predicted cross sections (times branching ratio) for the process $H^{\pm} \rightarrow W^{\pm}Z \rightarrow q\bar{q}'l^{+}l^{-}$. Red: Width fixed to 1 MeV. Green: Including the previously calculated width in `MadGraph`/`pythia`, all decays via `pythia`. Blue: Full matrix element calculated in `MadGraph`.

possible to use MadGraph to calculate the partial width associated with a certain decay by asking for the cross section of a $1 \to 2$-process. If one assumes that the charged Higgs only couples to the weak bosons, the partial width of the process $H^\pm \to W^\pm Z$ is equal to the total width of the Higgs[1]. This partial width of course again depends on the coupling coefficient assigned to the vertex. This means that rescaling the cross section is unfortunately not the only thing one has to do when considering different models. This is only relevant for Higgs masses and coupling constants where the width is larger than the expected uncertainty in the mass measurements caused by detector effects (e.g. uncertainties in the energy measurements). If the width is smaller than that, its effects on the mass distribution and other kinematic observables will be negligible. However, the width of the Higgs boson also influences the total cross section close to the kinematic threshold.

The predicted decay width assuming no other decay channels than $H^\pm \to W^\pm Z$ is shown in Fig. 5.4. It can be seen that for masses larger than about $400\,\text{GeV}$ the width is of the order of $10\,\text{GeV}$ or larger, which is large enough to be expected to influence mass measurements.

One can now include the previously calculated width as a fixed parameter in the MadGraph model and redo the cross section calculations. In Fig. 5.5, the results are compared to the previous calculations using a small width. The difference is negligibly small.

One can also use MadGraph to calculate the full process, including all decays, with this width information. This will include off-shell W and Z bosons. The resulting cross sections can also be seen in Fig. 5.5. There is a rather large deviation of more than 50% for small Higgs masses, but also for larger Higgs masses one can observe that the cross section obtained this way is about 20% smaller than the one quoted previously. This seems to indicate that simulating all decays in pythia is insufficient for our needs, as e.g. turn-on effects are not accounted for here. To get the best possible approximation, one should have used MadGraph to simulate the full decay chain. However, that proved impossible as MadGraph had trouble with the unweighting and could not produce the full number of events required. Hence, for the following plots shown in this chapter, MadGraph was always configured to produce an on-shell Higgs with a small width, and the decays were done in pythia, as there is little difference

[1] If one also considers non-zero couplings to e.g. fermions, the total width will be slightly larger, as one has to add the partial widths corresponding to the fermionic decays, while the partial width corresponding to the $H^\pm \to W^\pm Z$ decay will not be affected.

between this and having the full width information present.

5.5. Kinematic Properties, Event Selection Rules and Efficiencies

For each mass point and decay channel, a separate sample with 100.000 events is generated. Each has a positively charged Higgs boson, its decay products, and (simulated) detector information. In the following, "truth" will refer to the simulation results obtained from the `pythia` run, with all decays but before showering and hadronisation. "Measured" will refer to the results obtained after the detector simulation.

5.5.1. The Dilepton Channel

The results presented here are obtained using $\mu^+\mu^-$+jets final states. As only a limited detector simulation was available for these studies, the results for electrons+jets are not expected to be drastically different.
Events are selected using the following selection cuts:

- Exactly two muons, of opposite signs, with $p_T \geq 20\,\text{GeV}$ ("μ cut").
- Dimuon mass between 60 and $100\,\text{GeV}$ ("Z mass cut").
- At least two jets with $p_T \geq 15\,\text{GeV}$, $|\eta| < 2.5$ ("jet cut").

Each pair of such jets with $60\,\text{GeV} \leq m_{jj} \leq 95\,\text{GeV}$ is defined as a W candidate; only events with at least one W candidate are kept ("W mass cut"). Each W candidate combined with the Z candidate gives a Higgs candidate, thus some events might have more than one Higgs candidate. In this case, histograms are filled once for each Higgs candidate. In a final cut, only events with exactly one Higgs candidate are kept ("1 Higgs"). The cut acceptances (number of events passing this and all previous cuts divided by the total number of events) and cut efficiencies (number of events passing this cut divided by the number of events passing the previous cut) can be found in Tables 5.2 and 5.3. One can see that only about one quarter to one third of the events have at least one Higgs candidate. Requiring exactly one Higgs candidate, one loses approximately a further quarter to third of the events. This shows that using this method of assigning jet pairs as W candidates if they combine to the right mass, one gets a

$m_{H^\pm}$ [GeV]	μ cut	Z mass cut	jet cut	W mass cut	1 Higgs
180	0.456	0.430	0.386	0.247	0.150
200	0.492	0.458	0.414	0.264	0.163
250	0.553	0.511	0.467	0.303	0.198
300	0.587	0.542	0.499	0.330	0.224
400	0.631	0.580	0.536	0.366	0.257
500	0.656	0.604	0.550	0.357	0.260
600	0.680	0.626	0.552	0.298	0.219

Table 5.2.: Cut acceptances for different Higgs masses. All acceptances were calculated using a sample with 50000 events each, hence the statistical uncertainties can be approximated by $\sqrt{\frac{(acc)\cdot(1-acc)}{50000}} \leq \sqrt{\frac{1}{50000}} \approx 0.0044$.

$m_{H^\pm}$ [GeV]	μ cut	Z mass cut	jet cut	W mass cut	=1 Higgs
180	0.456	0.942	0.897	0.641	0.608
200	0.492	0.932	0.904	0.637	0.619
250	0.553	0.925	0.914	0.649	0.653
300	0.587	0.923	0.920	0.662	0.678
400	0.631	0.918	0.925	0.684	0.702
500	0.656	0.920	0.911	0.649	0.728
600	0.680	0.920	0.883	0.540	0.736

Table 5.3.: Cut efficiencies (cut flows) for different Higgs masses. All efficiencies were calculated using a sample with 50000 events each, hence the statistical uncertainties can be approximated by $\sqrt{\frac{(eff)\cdot(1-eff)}{50000}} \leq \sqrt{\frac{1}{50000}} \approx 0.0044$.

lot of combinatorial background, i.e. jets that do not come from a common "parent" particle, but still combine to some mass close to the W mass.

The p_T cuts used here are kept as loose as possible without getting to regions where object identification is unreliable.

5.6. Mass Measurements

Here, a **direct** method of measuring the mass of the charged Higgs boson is considered, simply combining the 4-momenta of the decay products to obtain the 4-momentum $p_{H^\pm}$ of the Higgs boson. Its mass is then given by the relativistic mass energy relation, $m^2_{H^\pm} = E^2_{H^\pm} - \vec{p}^2_{H^\pm}$.

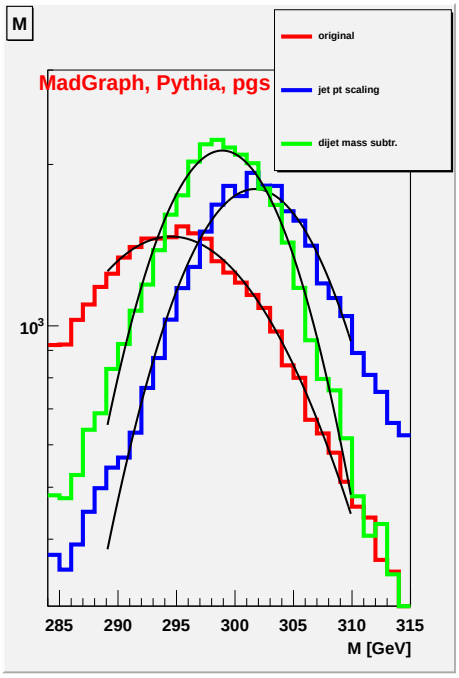

Figure 5.6.: Reconstructed Higgs mass in the dilepton channel, $m_{H^\pm} = 300\,\text{GeV}$ in the simulation. Red: original 4-object mass. Blue: 4-object mass after applying the jet energy rescaling method. Green: Mass after applying the dijet mass subtraction method.

The dileptonic channel is best suited for this approach since it does not have any neutrinos in the final state. All the decay products can in principle be detected and their energy and momentum measured. In the trilepton channel, only three out of four final state particles can be detected. However, the neutrino's transverse momentum can be determined from the energy balance in the detector (missing transverse energy $\not{E}_T$). Since the mass of the W boson is known, the longitudinal momentum of the neutrino can then be determined up to a twofold ambiguity. However, this approach relies on a precise and accurate measurement of the missing energy, which is affected heavily by pileup/multiple interactions etc. However, the trilepton channel is expected to have less contributions from e.g. combinatorial background, hence making it an interesting channel for mass measurements, as well.

5.6.1. The Dilepton Channel

Higgs candidates are selected according to the criteria given in section 5.5.1 and the so called "4-object mass" is calculated as the mass of the sum of the four decay products,

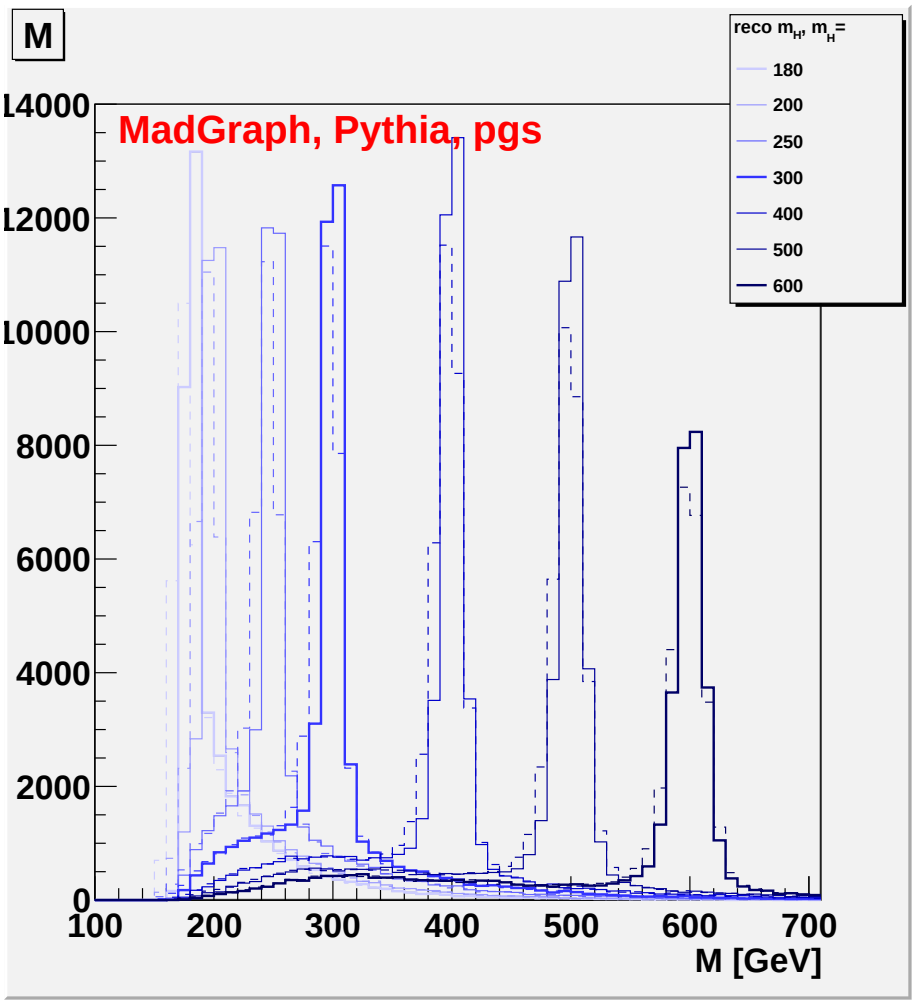

Figure 5.7.: Reconstructed Higgs masses in the dilepton channel ($H^{\pm} \to W^{\pm}Z, Z \to \mu\mu, W^{\pm} \to q\bar{q}'$) for seven different simulated Higgs masses (in GeV). Dashed lines: original mass before corrections. Solid lines: after applying dijet mass subtraction method.

all of which are visible to the detector:

$$M_{\mu\mu jj} := \sqrt{(p_{\mu^+} + p_{\mu^-} + p_{j_1} + p_{j_2})^2}. \tag{5.1}$$

This method of measuring the Higgs mass is limited by the uncertainty of the jet energy measurement, which is generally much less precise than the muon energy measurement. The uncertainty comprises both mis-calibration of the jet energy scale and the finite resolution of the jet energy measurements. However, since we assume that the two jets come from the decay products of the W boson, it is possible to improve on the naive combination of the four object momenta by using information of the mass

of the W.

Two methods of improving the Higgs mass resolution by taking into account our knowledge of the mass of the W boson are tested. Both rely on the assumption that the jet energy scale uncertainty is larger than the width of the W boson. In other words, one can assume that (for hadronically decaying Ws) "most" of the deviation of the dijet mass from the known W mass, and hence "most" of the deviation of the measured 4-object mass from the true (but unknown) Higgs mass, comes from a mis-measurement of the jet energy. Therefore, the measurements of the Higgs mass may be corrected by constraining the dijet mass to the W mass. However, the constraint is not unique since there are two jets with partially uncorrelated uncertainties contributing to the measurement. There are in principle continuously many ways to correct the jet energies that will result in the "correct" W mass. Two methods that can be applied easily, without knowledge of the η- and p_T-dependence of the jet energy scale and with no additional computing time, are studied.

It should be noted that, while not significantly biasing the signal, the correction methods presented here will probably bias the mass distribution due to background events (both combinatorial background and other processes with the same final state), as the dijet mass distribution is not expected to be symmetric about the W mass.

The first method considered here is used by other analysis groups, see the $H \to ZZ$ analysis in [39]. The dijet mass is constrained to the known W mass by rescaling both jet energies by a common factor $\frac{M_W}{M_{jj}}$, where $M_W = 80.4\,\text{GeV}$ is the W mass and $M_{jj} := \sqrt{(p_{j_1} + p_{j_2})^2}$ is the originally measured mass of the dijet system. The "re-scaled" Higgs mass M_{scale} is then calculated as before, but using the rescaled jet momenta. This method gives the most likely correction under the assumption that the relative energy mis-calibration is the same for both jets.

In the second method, the measured 4-object mass is corrected by subtracting the measured dijet mass and adding the known W mass: $M_{sub} := M_{\mu\mu jj} - M_{jj} + M_W$. This is only physically correct to first order (in the deviation of the measured from the true momenta).

In Fig. 5.6, both the original 4-object mass distribution and the two corrected masses are plotted for a Higgs mass of $300\,\text{GeV}$, with a Gaussian distribution fitted around the mass peak. All three distributions are well described by a Gaussian function. Both corrections lead to a higher mass peak with a smaller standard deviation. In addition, the mean is moved closer to the nominal value. The subtraction method seems to per-

form slightly better than the scaling method, hence it is used in the following studies. However, studies with full detector simulation will be needed to make a definite claim that one of these methods works better than the other.
In Fig. 5.7, the mass distributions for the seven studied Higgs masses can be seen. The original 4-object masses have dashed lines, the masses after applying the subtraction correction have solid lines. These distributions have been made using the 100000 events per mass point generated previously, and have not been rescaled according to the cross section. It can be seen that all masses except for $m_{H^\pm} = 180\,\text{GeV}$ feature a Gaussian mass peak and some (negligible) amount of combinatorial background. For $m_{H^\pm} = 180\,\text{GeV}$, the peak of the combinatorial background and the mass peak overlap, but one can still see a prominent Gaussian peak.
Both methods can slightly improve the mean mass resolution, but one needs a considerable number of observed Higgs decays for these methods to be useful.

5.6.2. The Trilepton Channel

The studies shown here are made in the $Z \rightarrow \mu\mu$, $W \rightarrow e\nu_e$ channel, but studies in other trileptonic channels are expected to show similar results. In this channel, the preselection for the $Z \rightarrow \mu\mu$ part was kept (two opposite-charge muons with $p_T > 20\,\text{GeV}$, dimuon mass between 60 and $100\,\text{GeV}$). For the W part, one electron with $p_T > 20\,\text{GeV}$ was required, and the missing transverse energy was required to be above $20\,\text{GeV}$ as well.

Mass measurements in the trilepton channels are challenging. A full reconstruction of the event kinematics is impossible due to the "missing energy" carried away by the neutrino. Still, these channels are expected to have less background and lower systematic uncertainties as the jet energy scale does not enter directly. Hence, mass measurements in this channel should be studied.

The Z candidate is reconstructed from the two muons as in the dilepton channel. The W candidate cannot be fully reconstructed. It is assumed that the only contribution to the missing energy comes from the neutrino (plus some smearing due to finite detector resolution).

Due to the neutrino in the final state, calculating the 4-object mass as in the analysis above is of course impossible. Hence, different variables related to the Higgs mass are studied:

Transverse mass

The transverse mass of an object is defined as

$$m_T := \sqrt{E_T^2 - p_T^2},$$

where $p_T := \sqrt{p_x^2 + p_y^2}$ is the transverse momentum and E_T is the transverse energy (i.e. the projection of the energy onto the transverse plane, $E_T := \cos(\theta) \cdot E$). The transverse 4-object mass is then defined as in eq. 5.1, only using transverse quantities. The transverse momentum and energy of the neutrino, assumed to be given by the missing transverse energy, is used instead of one of the charged lepton momenta. This is a very useful variable for final states containing one neutrino because it can be assumed that the transverse momentum of the neutrino is given by the "missing transverse energy" (the negative sum of all transverse energies of all detector objects), because events should be balanced in the transverse plane. The transverse mass is al-

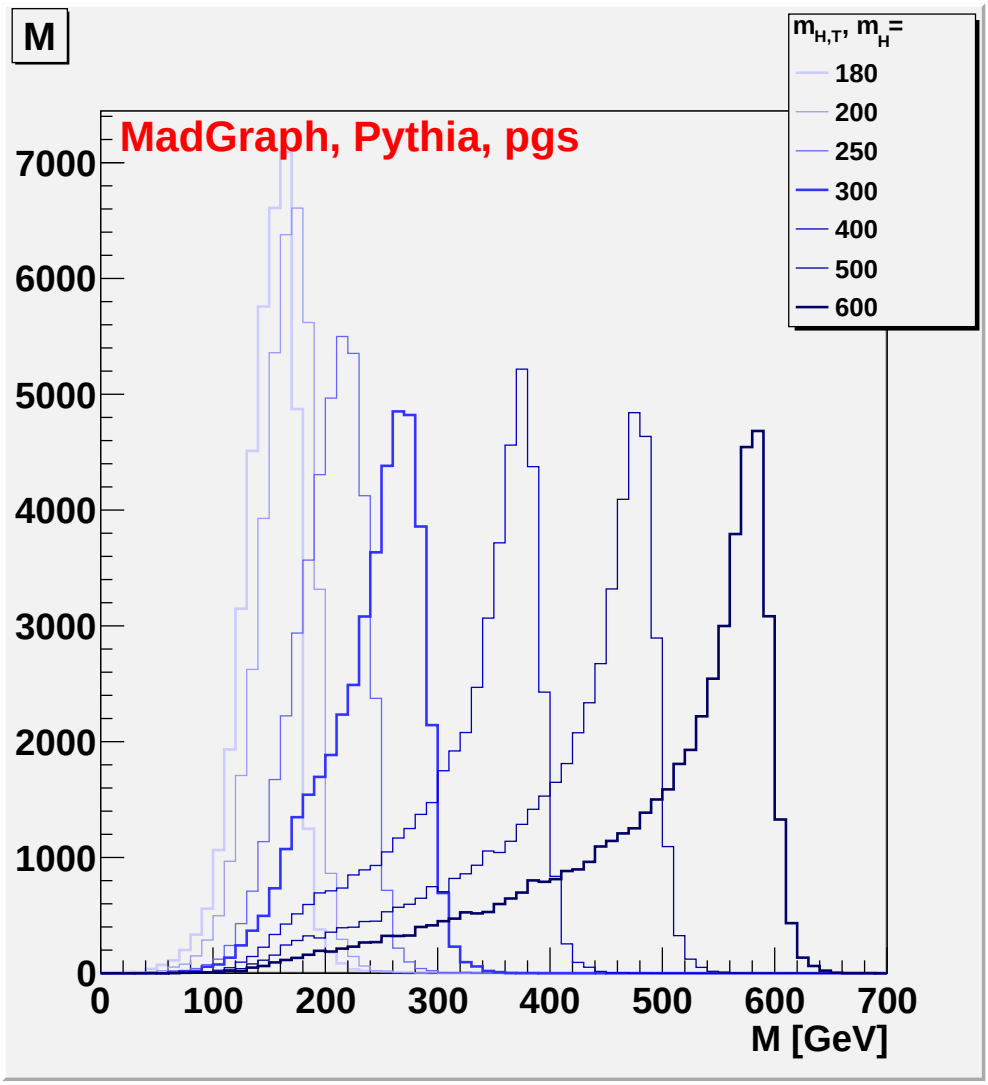

Figure 5.8.: Reconstructed transverse Higgs masses for seven different simulated Higgs masses (in GeV), trilepton channel ($H^{\pm} \to W^{\pm}Z$, $Z \to \mu\mu$, $W \to e\nu_e$).

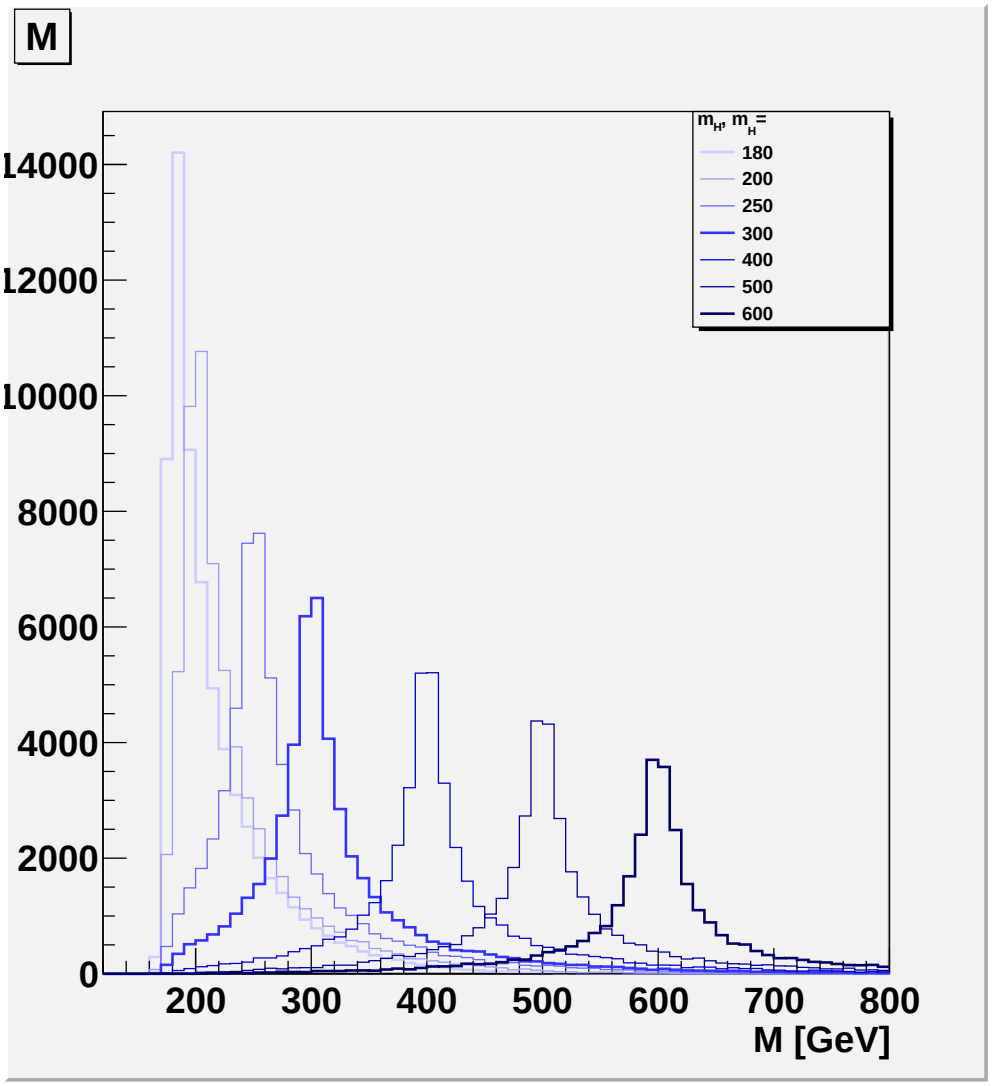

Figure 5.9.: Reconstructed Higgs masses, using the neutrino p_z from the W mass constraint, for seven different simulated Higgs masses (in GeV), trilepton channel ($H^\pm \to W^\pm Z$, $Z \to \mu\mu$, $W \to e\nu_e$).

ways smaller than the nominal mass. Due to the finite energy resolutions, one usually sees a steeply falling slope at the nominal mass of the parent particle.

In Fig. 5.8, the reconstructed transverse mass distribution is plotted for the different simulated Higgs masses. As expected, there is a steep slope around the nominal mass and a visible peak below that. If the position of this slope can be measured accurately, it is easy to determine the Higgs mass.

Measuring the neutrino p_z

The transverse momentum of the neutrino can be determined from "missing energy" because the event is expected to be balanced on the transverse plane (due to momentum conservation). This argument cannot be used for the longitudinal part of the momentum of a neutrino in a hadron collider: The fraction of the proton's longitudinal momentum carried by the partons that are involved in the "hard collision" is unknown. The proton remnants are too close to the beam pipe to be detected, leaving us unable to balance the event in the longitudinal direction. However, in the case of a W decaying into a charged lepton and a neutrino, there is an additional constraint that can be exploited: Neutrino and lepton must combine to an object with the (known) W mass. This can be expressed as

$$M_W^2 = (E_l + E_\nu)^2 - (\vec{p}_{T,l} + \vec{p}_{T,\nu})^2 - (p_{z,l} + p_{z,\nu})^2 . \tag{5.2}$$

If one assumes that the transverse momentum of the neutrino is given by the missing transverse energy, the only unknown quantity left is $p_{z,\nu}$, which can be solved for:

$$p_{z,\nu} = \frac{-b \pm \sqrt{b^2 - 4ac}}{2a}, \tag{5.3}$$

where

$$a = 4p_{z,l}^2 - 4E_l^2,$$

$$b = 4p_{z,l} \cdot \left(2\vec{p}_{T,l} \cdot \vec{p}_{T,\nu} + M_W^2\right),$$

and

$$c = \left(M_W^2 + 2\vec{p}_{T,l} \cdot \vec{p}_{T,\nu}\right)^2 - 4E_l^2 \vec{p}_{T,\nu}^2$$

(and with the approximation $m_l = \sqrt{E_l^2 - \vec{p}_{T,l}^2 - p_{z,l}^2} \approx m_\nu = \sqrt{E_\nu^2 - \vec{p}_{T,\nu}^2 - p_{z,\nu}^2} \approx 0$).

There are in general two solutions for the neutrino momentum, and it is impossible to determine which is the correct physical solution. For the following study, both solutions (if real) are kept and used to calculate the Higgs mass. If the solution turned out to be complex (due to mis-measured energies/momenta), the event is thrown out.

The reconstructed masses are plotted in Fig. 5.9. It can be seen that the mass distributions peak at the nominal mass. However, due to the large uncertainties and combinatorial background, the peaks are quite broad. Additionally, especially for larger Higgs

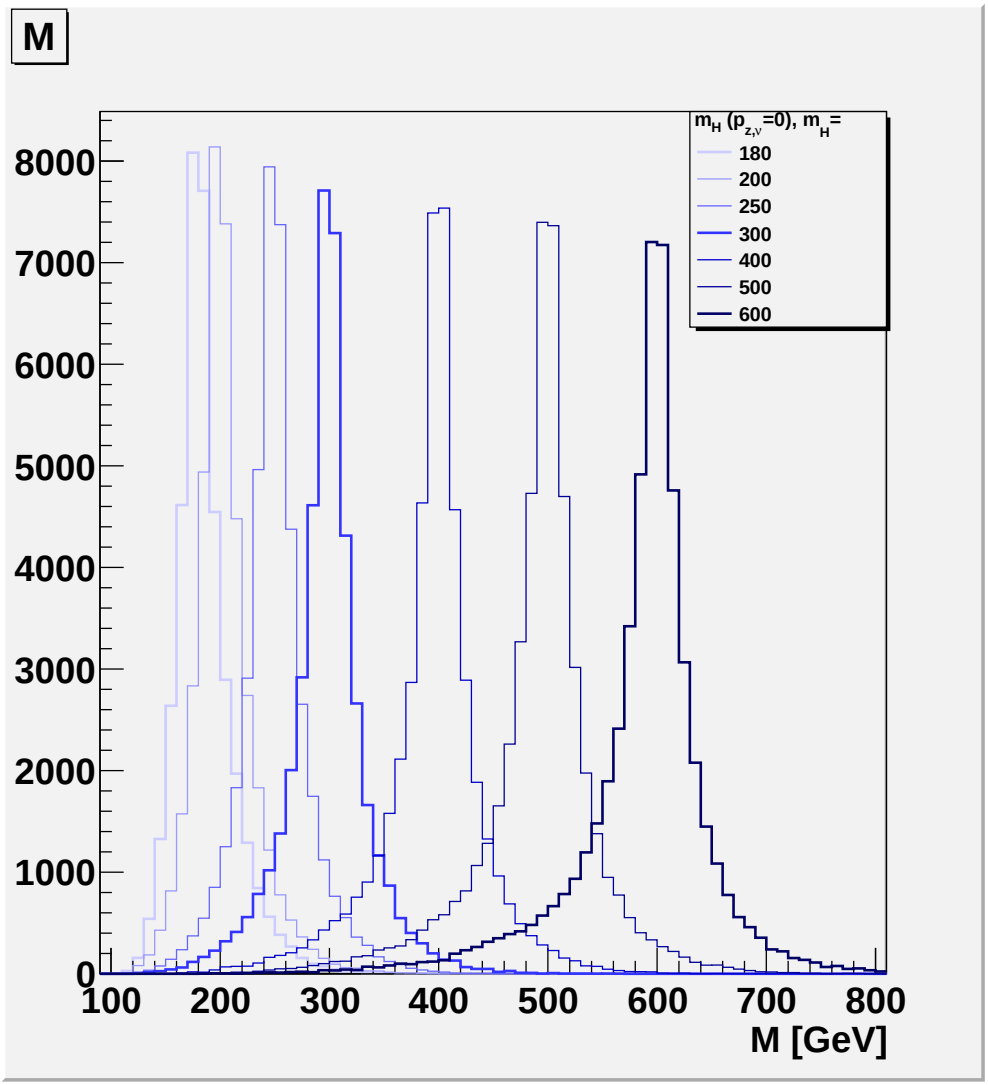

Figure 5.10.: Reconstructed Higgs masses, using the neutrino p_z set to 0, for seven different simulated Higgs masses (in GeV), trilepton channel ($H^{\pm} \to W^{\pm}Z$, $Z \to \mu\mu$, $W \to e\nu_e$).

masses, there are large losses due to non-real solutions for $p_{z,\nu}$. Further examination and use of full detector simulation is needed to determine if these losses will get bigger if the real detector resolution and pile-up effects are taken into account.

Neglecting the neutrino p_z

Since measuring the longitudinal momentum of the neutrino often leads to unphysical results (i.e. complex values), a third variable, m_0, is defined as the 4-object mass with the neutrino p_z set to 0. This is of course unphysical but in principle it should not lead

to large deviations from the nominal mass. In Fig. 5.10, the resulting mass distributions are shown. They do not peak at the nominal masses, but at slightly larger values. The peaks are not Gaussian, but narrow peaks with wide tails. Due to the bias, it would be challenging to use this method for an actual mass measurement. However, the sharp peaks might make it useful for a cross section measurement because they should be easily seen above the background.

5.7. Angular correlations

There are several angular observables in the final state whose distributions depend on the spin of the parent particles. In our case, the Higgs is a scalar particle decaying into two massive vector bosons. The final state particles are all (nearly) massless fermions. Observation of a new heavy particle and its decay modes is not all that has to be done to claim the discovery of a Higgs boson. The measurement of its properties is also very important to distinguish a Higgs from other new physics phenomena. If e.g. evidence for a massive particle decaying into a W and a Z boson is indeed found, it will need to be shown that the parent particle is indeed the predicted charged Higgs. A necessary part of that would be a measurement of the observed particle's spin, e.g. by exploiting angular observables. Here, several angular correlations have been examined to see if they would be useful in distinguishing a scalar charged Higgs from e.g. a new heavy vector boson (W').
Since no spin information is read in by `pythia`, the setup used for the generation of the previously studied samples cannot be used for studies of the angular observables of interest. Hence, new samples are generated where the full $H^{\pm} \rightarrow W^{\pm}Z \rightarrow \mu\mu jj$ decay is simulated with `MadGraph/MadEvent`. However, `MadGraph` seemed to have trouble filling the whole phase space and only produced a few thousand events, even after several days of run time. As a result, the Higgs samples suffer from low statistics. In addition, samples with the same final state, but with a heavy charged vector boson W' (having the same properties as the SM W boson, except for its mass) instead of the Higgs boson, are generated, using the same mass points for the W' as for the Higgs.
For the following studies, the samples described above are used. In order to see if any of the angular observables can be used to distinguish a hypothetically observed Higgs from other exotic particles, samples with W's with the same masses, decaying into W and Z bosons, are produced and studied. Several observables are studied, as motivated by the author of [40], who studied $H \rightarrow ZZ$ in four-lepton final states.

5.7.1. Decay plane angle

The decay plane angle ϕ is defined as the angle between the decay plane of the W boson and that of the Z boson *in the charged Higgs rest frame*. [40] also fix the orientation of the angle using the charge of the leptons. That cannot be done here as the

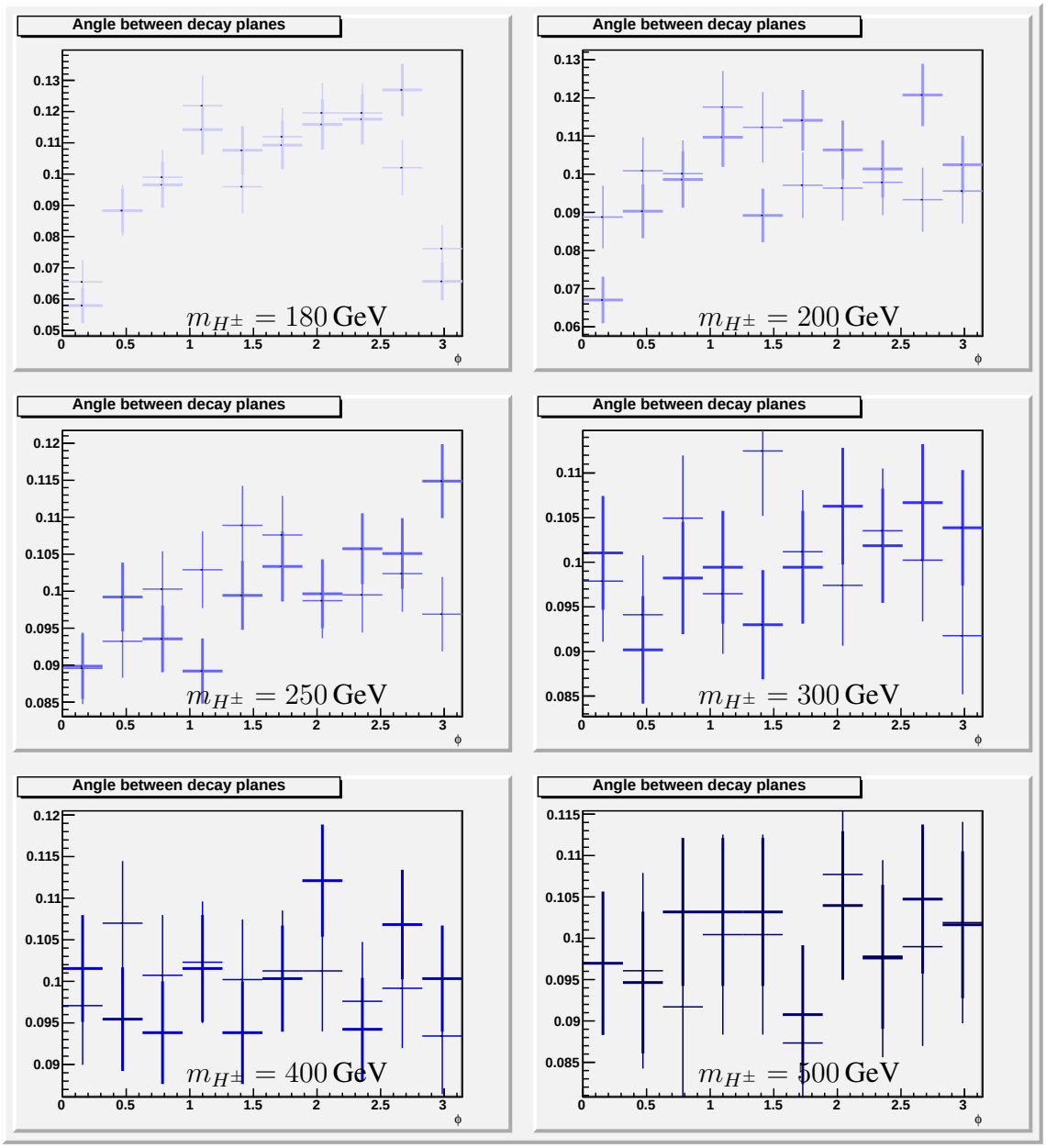

Figure 5.11.: Decay plane angle ϕ in the dilepton channel ($H^\pm \to W^\pm Z$, $Z \to \mu\mu$, $W^\pm \to q\bar{q}'$) for m_H =180, 200, 250, 300, 400, 500 GeV (left to right, top to bottom). Thick lines: truth distribution, parton level (`MadGraph`). Thin lines: after `pgs` simulation.

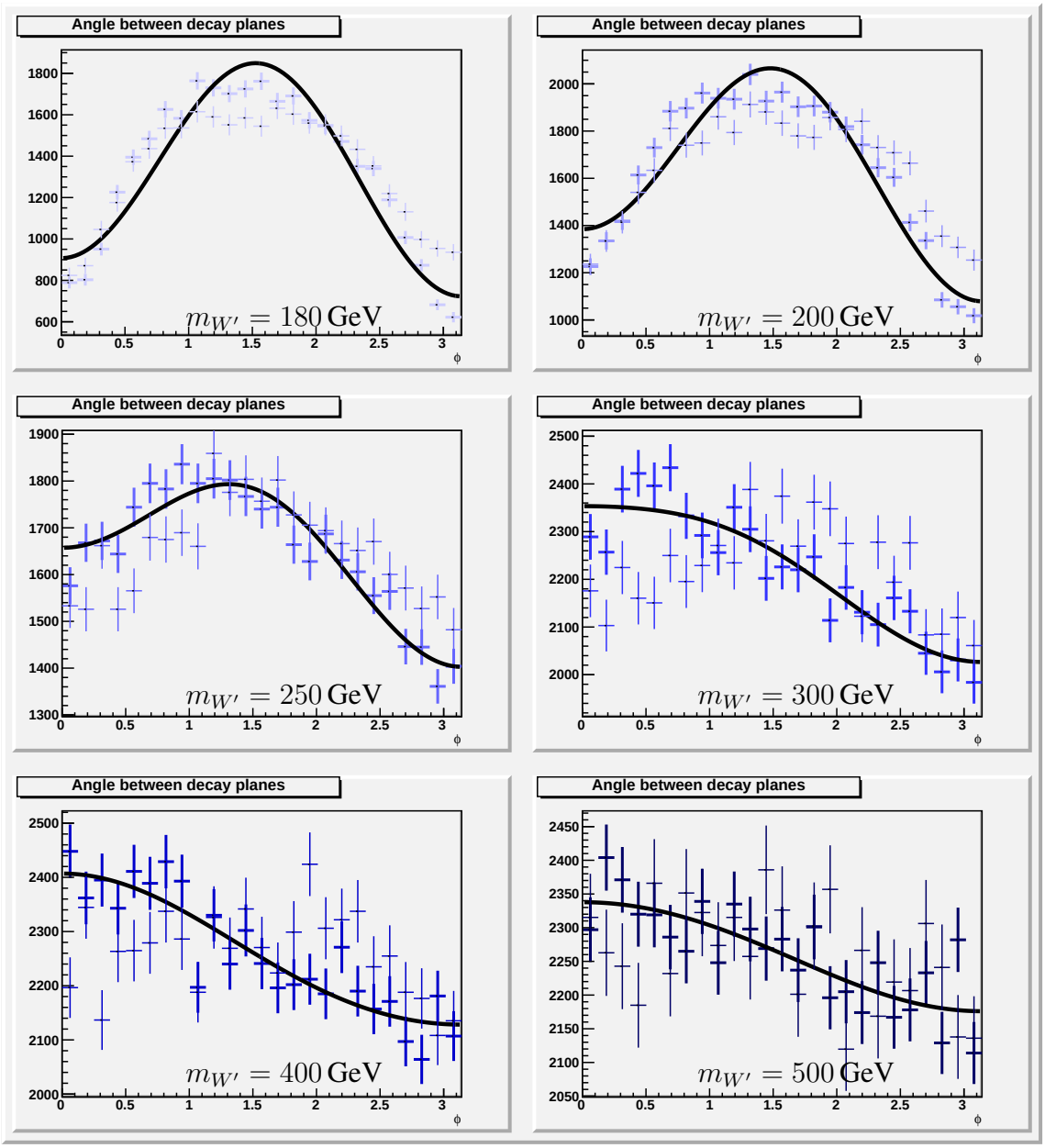

Figure 5.12.: Decay plane angle ϕ in the dilepton channel ($W' \to WZ$, $Z \to \mu\mu$, $W \to q\bar{q}'$) for $m_{W'}$ =180, 200, 250, 300, 400, 500 GeV (left to right, top to bottom). Thick lines: truth distribution, parton level (`pythia`). Thin lines: after `pgs` simulation.

jet charge cannot be measured accurately. Hence, ϕ is always chosen from the interval $[0, \pi)$. According to [40], the decay plane angle is distributed according to

$$F(\phi) = 1 + \alpha \cdot \cos(\phi) + \beta \cdot \cos(2\phi). \tag{5.4}$$

For the case of W', they calculate $\alpha \approx 0.017$ and $\beta = 0$. For the Higgs, α and β depend on the Higgs mass. They are both positive and tend to 0 for larger Higgs masses.

The decay plane angle distributions simulated with `MadGraph`/`pythia` are plotted in Fig. 5.11 for the Higgs and in Fig. 5.12 for the W', both on parton level (i.e., using truth quark information, before parton shower and hadronisation) and after the detector simulation. Due to the low statistics, it is almost impossible to make any definite statement about the distributions. It seems that the detector simulation noticeably changes their shapes. No further analysis has been attempted for the Higgs case. The distributions for the W' case are fitted according to eq. 5.4. The results have been plotted in Fig. 5.13. It can be seen that they do not correspond to the expected values. The reason for that is unclear. It might point to an inconsistency in the configuration/use of `MadGraph`.

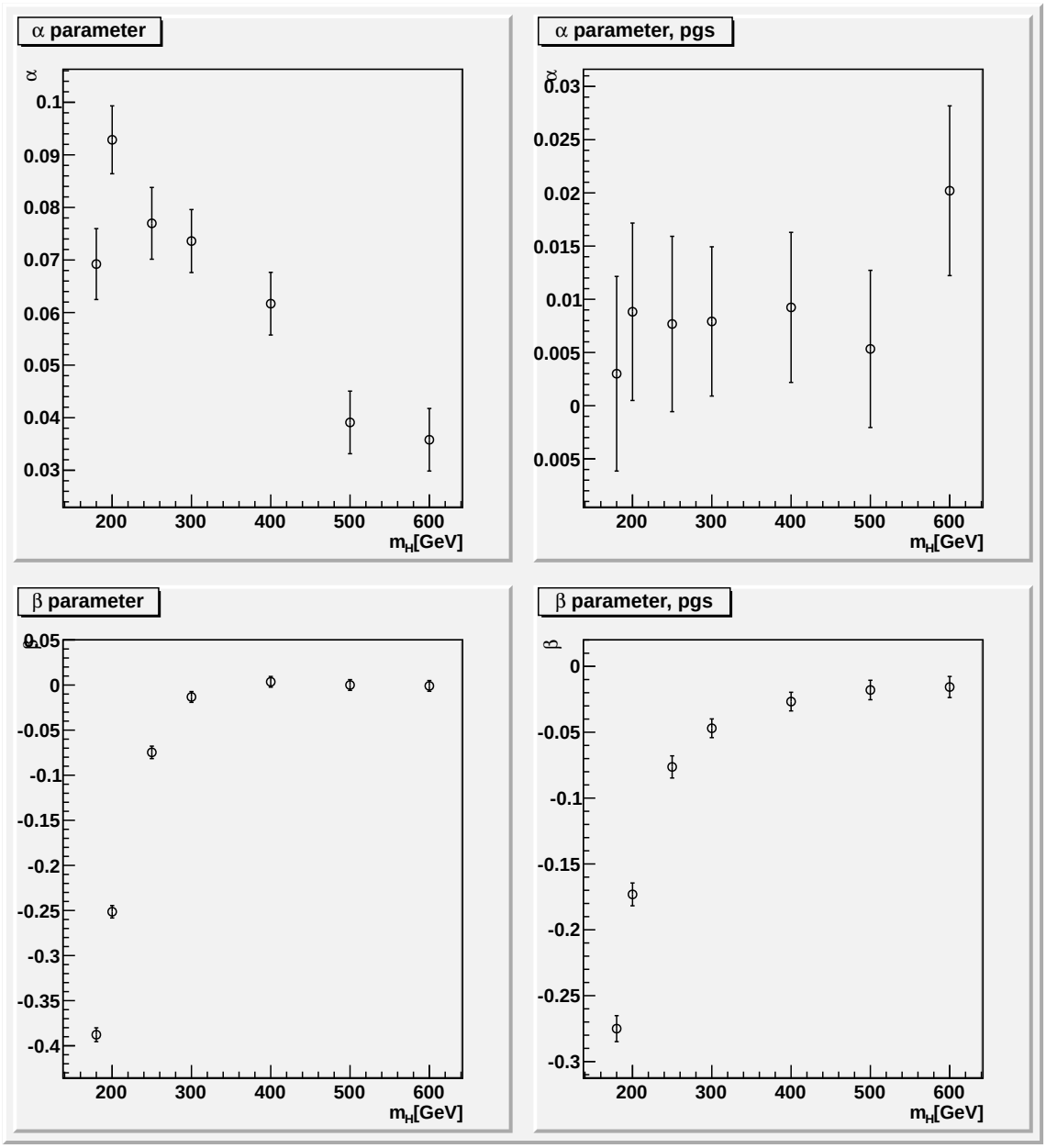

Figure 5.13.: α and β parameters plotted against $m_{W'}$. (Left: truth distribution, parton level (`pythia`). Right: after `pgs` simulation.)

5.7.2. Angle between Z boson and muon

The angle θ is defined as the angle between the Z boson (in the Higgs rest frame) and the μ^- in the Z rest frame. The authors of [40] parametrise its distribution as

$$G(\theta) = T \cdot (1 + \cos^2(\theta)) + L \cdot (\sin^2(\theta)). \tag{5.5}$$

Since the overall normalization is not important for this study, one defines the ratio

$$R := \frac{L - T}{L + T}. \tag{5.6}$$

According to [40], $R = \frac{1}{3}$ for the W' case. For the Higgs case, R grows with $m_{H^\pm}$ and tends to 1 for large Higgs masses.

One can define a corresponding angle on the W side as well. However, it is not possible to measure the charge of the jets accurately enough to discriminate between quark and anti-quark, so one would have to use the absolute value of the angle. Also, one expects a higher energy uncertainty on the W side. Hence, only the Z side is studied here.

In Fig. 5.14, the $\cos(\theta)$ distribution obtained from the `MadGraph` samples for the Higgs case is plotted for different Higgs masses. Again, it can be seen that one suffers from low statistics, but the shape looks more stable w.r.t. smearing than is the case for the ϕ distribution. Fits corresponding to eq. 5.5 are performed and the ratio R is calculated for each Higgs mass. The resulting values of R are plotted in Fig. 5.16. The values on parton level are consistent with the ones after the detector simulation. R is quite low (ca. 0.3) for low Higgs masses and compatible with 1 for larger Higgs masses.

In Fig. 5.15, the $\cos(\theta)$ distribution obtained from the `MadGraph` samples for the W' case is plotted for different W' masses. Fits corresponding to eq. 5.5 are performed and the ratio R is calculated for each W' mass. The resulting values of R are plotted in Fig. 5.17. The values on parton level are similar to the ones after the detector simulation. For $m_{W'} = 200\,\text{GeV}$ there are larger deviations. For both cases, the overall shape does not conform to the expectations. The shape is not flat, but definitely rising (at least for low W' masses). In addition, the ratio tends to roughly 0.8 for large W' masses, not $\frac{1}{3}$ as predicted.

Lacking time for further studies, it is not possible to draw a final conclusion from these studies of two angular observables. In particular, the simulation of the spin correlations

using MadGraph has to remain unverified. It is possible that they are not simulated correctly, or that MadGraph has not been configured properly. Alternatively, the angular distributions might be different for the charged Higgs w.r.t. the neutral Higgs studied by [40], necessitating further studies and eventual measurements to verify the validity of this model. However, it is doubtful that a measurement of the spin correlations will even be possible in the near future as a large amount of observed events will be needed.

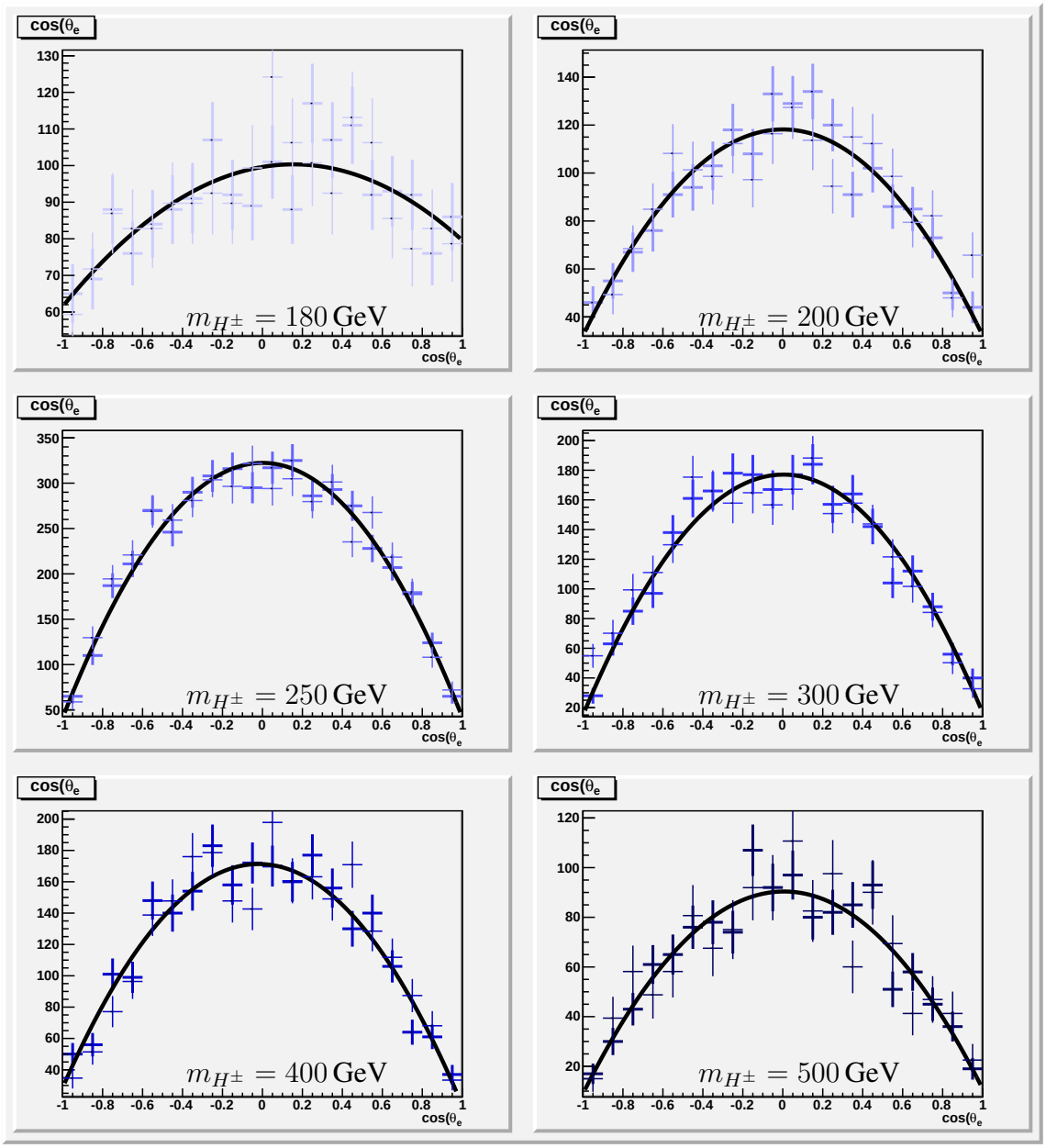

Figure 5.14.: $\cos(\theta)$ distribution in the dilepton channel ($H^{\pm} \to W^{\pm}Z$, $Z \to \mu\mu$, $W \to q\bar{q}'$) for $m_{H^{\pm}} = 180$, 200, 250, 300, 400, 500 GeV (left to right, top to bottom). Thick lines: truth distribution, parton level (`pythia`). Thin lines: after `pgs` simulation.

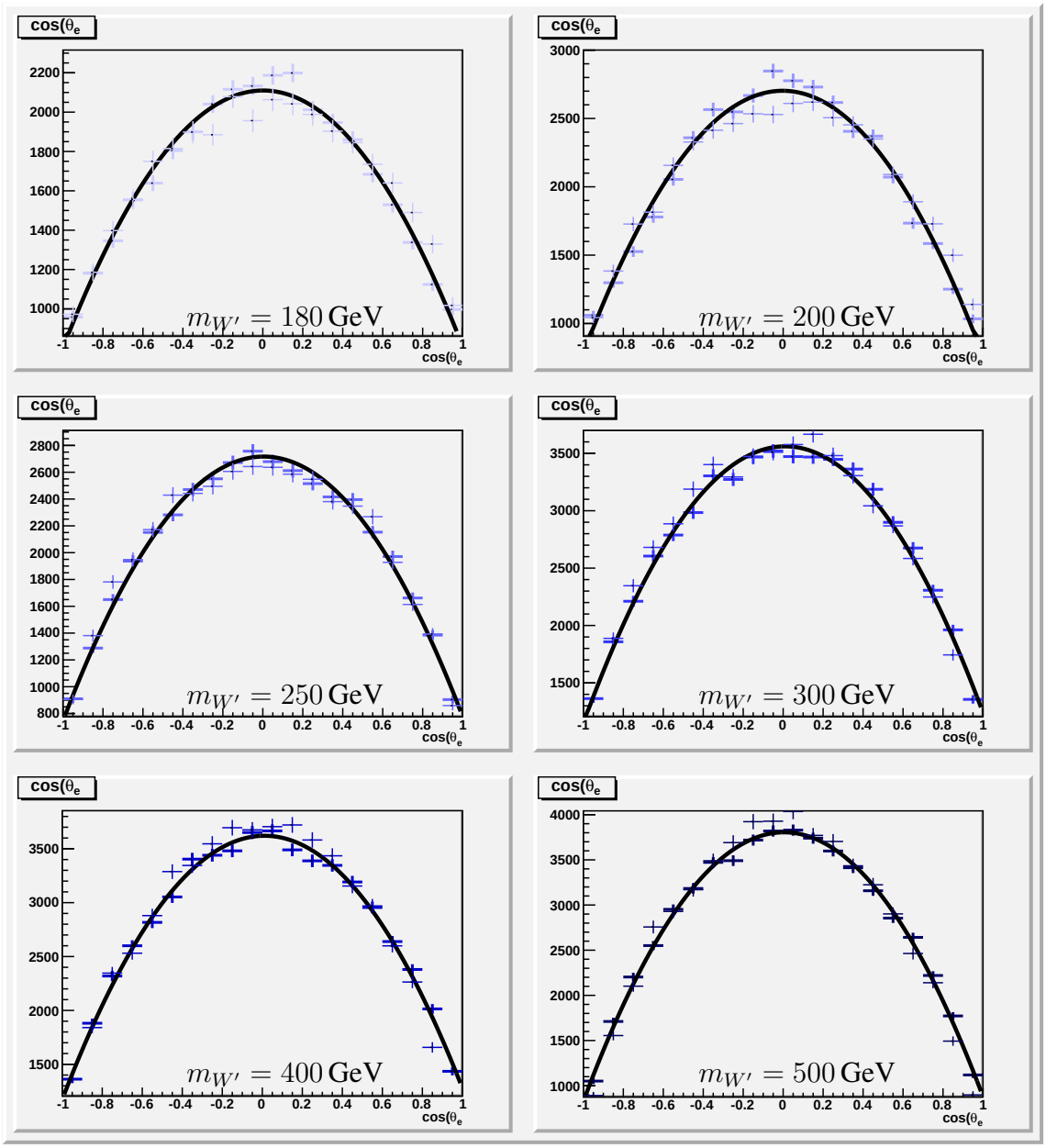

Figure 5.15.: $\cos(\theta)$ distribution in the dilepton channel ($W' \to WZ$, $Z \to \mu\mu$, $W \to q\bar{q}'$) for $m_{W'}$ =180, 200, 250, 300, 400, 500 GeV (left to right, top to bottom). Thick lines: truth distribution, parton level (`pythia`). Thin lines: after `pgs` simulation.

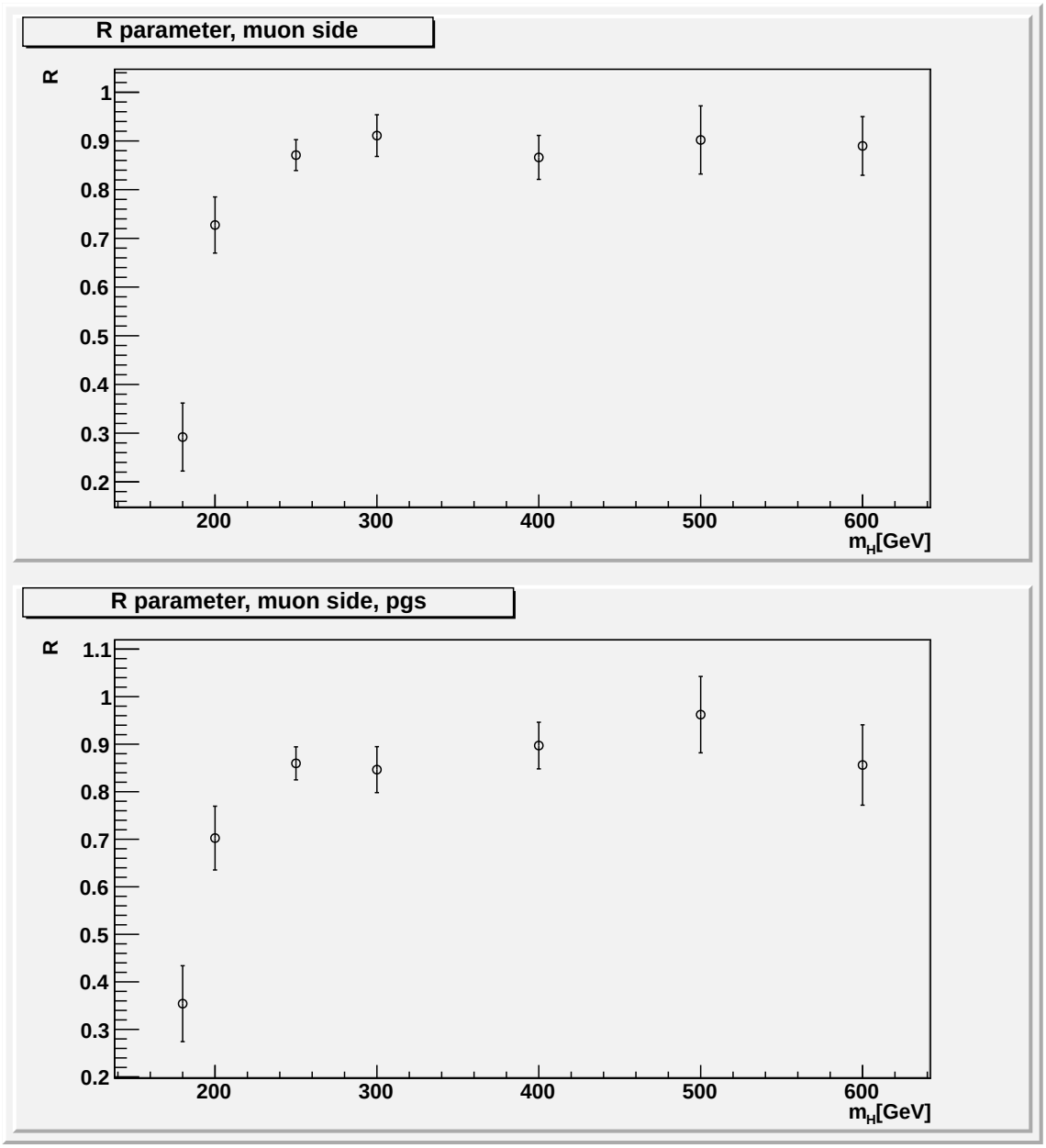

Figure 5.16.: R parameter plotted against $m_{H^\pm}$. (Top: truth distribution, parton level (`pythia`). Bottom: after `pgs` simulation.)

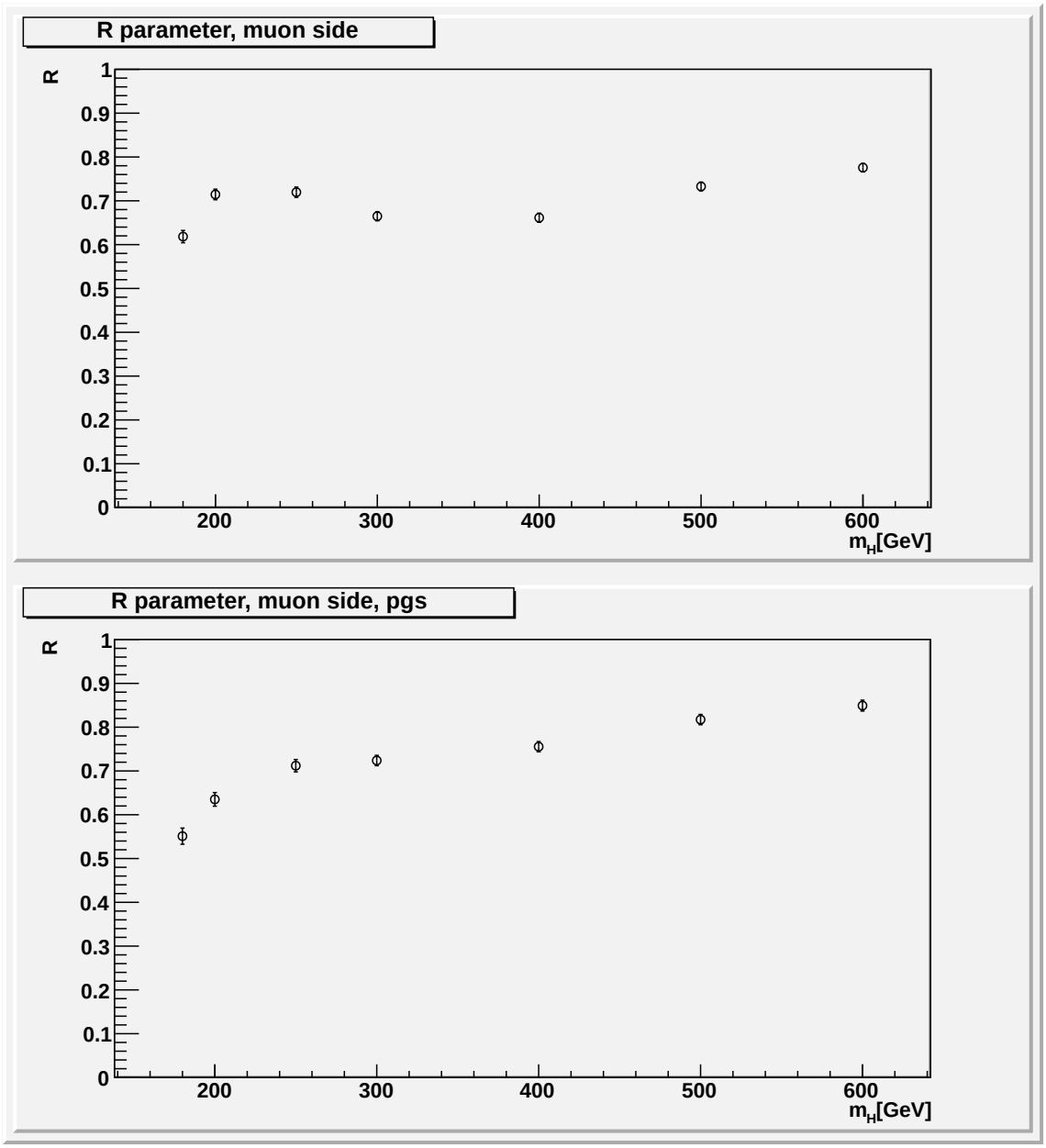

Figure 5.17.: R parameter plotted against $m_{W'}$. (Top: truth distribution, parton level (`pythia`). Bottom: after `pgs` simulation.)

6. Studies within the ATLAS experiment

This chapter describes the results obtained at the 2. Physikalisches Institut at the Georg-August-Universität Göttingen, as part of the ATLAS collaboration. ATLAS software, data and simulations were used to obtain the plots and results presented here. All studies presented here were done in the jje^+e^- final state.

6.1. Background Processes

The process to be studied later on is the production of a charged Higgs boson which decays into a W and a Z boson. Both hadronic and leptonic decays of the W are considered, with emphasis placed on the hadronic modes. For the Z, only decays into charged leptons l^+l^- (l will stand for e or μ in the following) are considered. As described in section 5.2, the production predominantly happens by the vector boson fusion (VBF) process, leading to two additional jets in the forward region of the detector. If all particles are reconstructed perfectly, the final state should contain:

hadronic W (dilepton channel) : Two leptons combining to the invariant Z mass, two jets combining to the invariant W mass (and two energetic forward jets). The transverse energy should be roughly balanced.

leptonic W (trilepton channel) : Two leptons combining to the invariant Z mass, one additional lepton, some amount of missing transverse energy (and two energetic forward jets).

There are lots of processes that produce a similar final state. As most of the work focuses on the $l^+l^-q\bar{q}'$ final state (i.e. the hadronic W case, only backgrounds to this process are covered here in detail.

1. **Production of a $Z/\gamma^* \rightarrow l^+l^-$ in association with jets (from initial/final state radiation, underlying event etc.)**. This is the dominant background and is largely irreducible. To distinguish it from the signal events, some features of the jets kinematics, e.g. angular distributions, may be employed.

2. **Production of a $W^\pm Z$ or ZZ pair, with one Z decaying leptonically and the other vector boson decaying hadronically**. These events have similar features to the signal events and are thus another source of irreducible background. To distinguish the two, one would have to look at e.g. the invariant mass spectrum of the two bosons.

3. **Production of a $Z/\gamma^* \rightarrow \tau^+\tau^-$ in association with jets, where the τs decay leptonically**. However, leptons from these decays do usually not combine to the Z mass. Additionally, these events have some missing energy due to the neutrinos from the τ decays.

4. **Production of a $W^\pm W^\mp$ pair, with both $W^\pm$s decaying leptonically**. Leptons from these decays do again usually not combine to the Z mass. Additionally, these events have some missing energy due to the neutrinos.

5. **Production of a $t\bar{t}$ pair, with both top quarks decaying leptonically**. This is analogous to the $W^\pm W^\mp$ case. In addition, there are two b-jets from the top decays, which can be tagged due to the relatively large life-time of the b-mesons.

6. **Production of a $W \rightarrow l\nu$ or $t \rightarrow l\nu b$ in association with jets, with one additional "fake"[1] lepton from a jet**. Here we would again expect some amount of missing energy. Also, the second lepton should not be isolated in the detector, but surrounded by other tracks/energy depositions from hadrons in the jet, and the leptons do generally not combine to the Z mass.

7. **Multijet production (via QCD processes) with two "fake" leptons**. Again, these leptons do generally not combine to the Z mass and are not isolated.

Generally, some of the background can be removed by requiring the dilepton mass to be close to the Z mass and the dijet mass to be close to the W mass. In addition, one

[1] This expression denotes a detector object that passes lepton identification criteria, but does in fact originate from a jet. In particular, this could be a real lepton from a leptonic decay of a meson, or a pion misidentified as an electron in the calorimeter.

could veto events with large missing energy, one or more jets tagged as b-jets, and consider only isolated leptons. However, some background events will probably still pass these cuts, e.g. due to detector inefficiencies or because they can not be distinguished in principle. Understanding and further reducing the background events is a large part of the work presented here.

6.2. Samples and Datasets

A detailed description of the software and datasets used is given in Appendix A. For the results shown here, the full 2011 dataset recorded by ATLAS is used ($L \approx 4.7\text{fb}^{-1}$).
For the signal sample, 50000 events $H^{\pm} \rightarrow W^{\pm}Z \rightarrow jje^{+}e^{-}$ were generated with MadGraph, using the procedure described in section 5.1, but with a full simulation of the ATLAS detector. This was done separately for seven mass points between 180 and 600 GeV. Both VBF and associated production processes were considered. In the case of associated production with a W or Z boson, the additional vector boson was forced to decay hadronically.
For the background samples, official ATLAS samples of the following processes are used:

- $Z \rightarrow e^{+}e^{-}$+jets
- $Z \rightarrow \tau^{+}\tau^{-}$+jets
- $W \rightarrow e\nu_{e}$+jets
- $t\bar{t}$ pair production (with at least one top quark decaying leptonically)
- single top production
- Diboson production: $W^{\pm}W^{\mp}$, $W^{\pm}Z$, ZZ (inclusive, i.e. with all possible final states).

QCD background with two "fake" electrons was not simulated. Instead, isolation criteria for the electrons were chosen so tight that this source of background can be neglected.
Monte Carlo events were reweighted by an overall factor (depending on the process) to reflect the measured luminosity of the data. The simulated events were further reweighted by μ, the average number of inelastic proton-proton collisions per bunch crossing,

to have the same pile-up conditions as found in data [41], and by a factor correcting the electron identification/reconstruction efficiency [42]. $Z \rightarrow e^+e^-$+jet events are also reweighted by the p_T of the Z candidate to have the same distribution as found in data after subtracting the other background contributions.

6.3. Object Selection and Triggers

In the selection of reconstructed objects used in the analysis, some requirements on the object quality are made. Only objects passing these criteria are considered during the analysis.

Electrons are required to pass `medium++` requirements on the shower shape and the quality of the matched track (similar to the old `medium` criterion described in [43]). To avoid the "crack" region between barrel and endcap calorimeters, electrons are required to have a pseudorapidity of $|\eta| < 1.37$ or $1.52 < |\eta| < 2.47$. To further suppress electrons from hadronic decays, electrons are required to be isolated both in the tracker and in the calorimeter, via the two flags `Eiso98ptcone20` and `Eiso98Etcone20`, each being constructed to have 98% efficiency for truly isolated electrons. `Eiso98ptcone20` requires isolation in the tracker, i.e. makes a cut on the p_T sum of the tracks in a cone of radius 0.2 around the electron. `Eiso98Etcone20` requires isolation in the calorimeter, i.e. makes a cut on the deposited energy in a cone of radius 0.2 around the electron. To be well above the trigger threshold, only electrons with $p_T > 20\,\text{GeV}$ are considered.

Jets are reconstructed from calorimeter clusters, using the anti-k_T algorithm [28] with angular resolution parameter of 0.4. Because of the large uncertainties of the background prediction, some difficulty of removing pile-up and some discrepancy between data and background simulation seen in the forward regions, only jets with $|\eta| < 2.5$ are considered. Contribution from pile-up is removed by requiring the jet vertex fraction to be above 0.75 if there are associated tracks. Only jets with $p_T > 30\,\text{GeV}$ are considered.

Jets and electrons are ordered according to their p_T. For some later studies, the first three or four jets (according to p_T) were ordered by η.

The exact trigger configuration depends on the run number. The three triggers used (`EF_2e12_medium`, `EF_2e12T_medium`, and `EF_2e12vh_medium`) are very similar, each requiring two electrons passing medium quality cuts with a $p_T > 12\,\text{GeV}$.

In events with exactly two electrons, the Z candidate is reconstructed as the sum of the two electrons.

6.4. Observables and Preselection Cuts

The final state that is of interest here contains two high-p_T electrons from the Z decay, two high-p_T jets from the W decay, and two forward-jets due to the VBF process (or two more jets from the additional vector boson). The following preselection requirements were used, based on [44]:

- Good run list, at least one good vertex with more than two tracks.
- Trigger pass.
- Veto on error flags to veto events with malfunctioning calorimeter cells.
- Exactly two electrons of opposite charge.
- Invariant dielectron mass in window around Z mass: $66\,\text{GeV} < m_{ee} < 116\,\text{GeV}$.
- At least two jets.

The expected number of signal- and background events passing these cuts can be found in Tables 6.1 and 6.2. For events passing this preselection, several observables were defined and computed. Some of them were used for validation of the MC simulation, others were used as input variables to train a set of boosted decision trees.

- p_T and η of the leading, second, third, and fourth leading jet.
- p_T and η of the leading and second leading electron.
- p_T of the Z candidate.
- Invariant mass of all jets in the event.
- Maximal pseudorapidity difference $\Delta(\eta)_{max}$ amongst the first up to four jets in the event.
- Invariant mass and combined p_T of different combinations of jets and electrons.

For events with three or more jets, the first up to four jets are also ordered by η. For signal events, we expect two more central jets from the W, combining to a mass of around $80\,\text{GeV}$, and two forward jets from the VBF process. Ordering in η, thus, the first and the last jet should come from the VBF process and combine to a relatively large mass. The central two jets should be the decay products of the W. In the following, M_{ij} will refer to the combined mass of the ith and jth jet, ordered by η. M_{eeij} will refer to the combined mass of the ith and jth jet, ordered by η, and the two electrons making up the Z candidate. Correspondingly, $p_{T,ij}$ will refer to the combined p_T of the ith and jth jet, ordered by η.

none	$1665330^{+111061}_{-110931}$	6092^{+684}_{-721}	1986^{+129}_{-129}	6880^{+467}_{-467}	8048^{+532}_{-532}	1219^{+81}_{-81}	996^{+66}_{-66}	1417^{+94}_{-94}	$1691970^{+112355}_{-112224}$	3052610 ± 1747
vertex	$1665330^{+111061}_{-110931}$	6092^{+684}_{-721}	1986^{+129}_{-129}	6880^{+467}_{-467}	8048^{+532}_{-532}	1219^{+81}_{-81}	996^{+66}_{-66}	1417^{+94}_{-94}	$1691970^{+112355}_{-112224}$	3052610 ± 1747
trigger	$1581890^{+105558}_{-105434}$	5667^{+637}_{-672}	1740^{+115}_{-115}	4997^{+356}_{-356}	7373^{+489}_{-488}	556^{+37}_{-37}	956^{+64}_{-64}	1356^{+90}_{-90}	$1604540^{+106651}_{-106525}$	2160840 ± 1470
LAr error	$1581890^{+105558}_{-105433}$	5667^{+637}_{-672}	1740^{+114}_{-114}	4997^{+346}_{-346}	7373^{+489}_{-488}	556^{+37}_{-37}	956^{+64}_{-64}	1356^{+90}_{-90}	$1604540^{+106651}_{-106525}$	2154800 ± 1468
hfor	$1575160^{+105110}_{-104986}$	5667^{+637}_{-672}	1740^{+114}_{-114}	4997^{+346}_{-346}	7373^{+489}_{-488}	556^{+37}_{-37}	956^{+64}_{-64}	1356^{+90}_{-90}	$1597810^{+106203}_{-106078}$	2154800 ± 1468
electron mult	$1200980^{+81739}_{-81625}$	3277^{+375}_{-395}	417^{+41}_{-41}	913^{+146}_{-146}	2808^{+210}_{-211}	372^{+26}_{-26}	660^{+45}_{-45}	911^{+62}_{-62}	$1210330^{+82179}_{-82065}$	1220170 ± 1105
electron charge	$1179300^{+80226}_{-80116}$	3226^{+368}_{-388}	389^{+32}_{-32}	496^{+66}_{-66}	2740^{+201}_{-201}	364^{+25}_{-25}	645^{+44}_{-44}	852^{+58}_{-58}	$1188010^{+80627}_{-80517}$	1200920 ± 1096
dilepton mass	$1128250^{+76636}_{-76533}$	1156^{+137}_{-143}	147^{+13}_{-13}	155^{+40}_{-39}	695^{+61}_{-61}	138^{+10}_{-10}	608.0^{+41}_{-41}	775^{+53}_{-53}	$1131930^{+76783}_{-76679}$	1131840 ± 1064
LAr hole jet	$1127280^{+76570}_{-76467}$	1150^{+133}_{-139}	146^{+12}_{-12}	155^{+21}_{-20}	694^{+54}_{-54}	138^{+10}_{-10}	605.2^{+41}_{-41}	771^{+53}_{-53}	$1130940^{+76716}_{-76613}$	1130940 ± 1063
jet mult	30561^{+3986}_{-3307}	798^{+97}_{-100}	$44^{+5.9}_{-6.1}$	$8.3^{+17.4}_{-17}$	20^{+17}_{-17}	$2.4^{+2.3}_{-2.2}$	167.6^{+19}_{-17}	199^{+23}_{-20}	31802^{+3980}_{-3271}	29724 ± 172
Δr jet	28882^{+3593}_{-2969}	764^{+92}_{-95}	$41^{+4.4}_{-4.6}$	$7.6^{+2.7}_{-2.7}$	$17.5^{+3.8}_{-3}$	$2.3^{+0.6}_{-0.4}$	159.0^{+18}_{-16}	188^{+22}_{-19}	30061^{+3667}_{-3030}	27865 ± 167
$N_J \geq 3$	5614^{+900}_{-702}	282^{+45}_{-43}	$10^{+2.9}_{-2.7}$	$1.2^{+1.7}_{-1.8}$	$3.1^{+1.8}_{-1.5}$	$0.2^{+0.2}_{-0.2}$	$29.5^{+5.2}_{-4.4}$	$38.9^{+6.4}_{-5.2}$	$5979.3^{+938.8}_{-732}$	5387 ± 73
$N_J \geq 4$	1056^{+206}_{-160}	73^{+16}_{-16}	$2^{+1.4}_{-1.3}$	$0.0^{+0.8}_{-0.8}$	$0.6^{+0.8}_{-0.7}$	$0.0^{+0.1}_{-0.1}$	$4.0^{+1.2}_{-1.1}$	$5.6^{+1.6}_{-1.3}$	$1140.1^{+213.6}_{-166}$	1056 ± 32
$N_J \geq 5$	187^{+42}_{-35}	17^{+7}_{-8}	$0.5^{+0.6}_{-0.7}$	$0.0^{+0.0}_{-0.0}$	$0.0^{+0.3}_{-0.3}$	$0.0^{+0.0}_{-0.0}$	$0.5^{+0.4}_{-0.4}$	$0.8^{+0.5}_{-0.4}$	$205.6^{+43.2}_{-36}$	200 ± 14

Table 6.1.: Expected number of background events by process and measured number of events, after cuts.

Cut	$m_{H^\pm} = 180\,\text{GeV}$	$m_{H^\pm} = 200\,\text{GeV}$	$m_{H^\pm} = 250\,\text{GeV}$	$m_{H^\pm} = 300\,\text{GeV}$	$m_{H^\pm} = 400\,\text{GeV}$	$m_{H^\pm} = 500\,\text{GeV}$	$m_{H^\pm} = 600\,\text{GeV}$
none	346^{+14}_{-13}	280^{+11}_{-11}	$176.61^{+6.90}_{-6.89}$	$121.02^{+4.73}_{-4.73}$	$62.55^{+2.45}_{-2}$	35^{+1}_{-1}	$21.05^{+0.83}_{-0.83}$
vertex	346^{+9}_{-9}	280^{+7}_{-7}	$176.59^{+4.73}_{-4.72}$	$121.01^{+3.35}_{-3.34}$	$62.54^{+1.78}_{-2}$	35^{+1}_{-1}	$21.05^{+0.63}_{-0.63}$
trigger	220^{+9}_{-9}	181^{+7}_{-7}	$117.44^{+4.70}_{-4.70}$	$83.36^{+3.33}_{-3.33}$	$44.29^{+1.77}_{-2}$	26^{+1}_{-1}	$15.67^{+0.63}_{-0.63}$
LAr error	220^{+9}_{-9}	181^{+7}_{-7}	$117.44^{+4.70}_{-4.70}$	$83.36^{+3.33}_{-3.33}$	$44.29^{+1.77}_{-2}$	26^{+1}_{-1}	$15.67^{+0.63}_{-0.63}$
hfor	220^{+5}_{-5}	181^{+4}_{-4}	$117.44^{+2.81}_{-2.81}$	$83.36^{+2.07}_{-2.07}$	$44.29^{+1.16}_{-1}$	26^{+1}_{-1}	$15.67^{+0.44}_{-0.44}$
electron mult	106^{+5}_{-5}	92^{+4}_{-4}	$65.21^{+2.75}_{-2.75}$	$48.67^{+2.03}_{-2.03}$	$27.53^{+1.14}_{-1}$	17^{+1}_{-1}	$10.44^{+0.43}_{-0.43}$
electron charge	105^{+5}_{-5}	91^{+4}_{-4}	$64.50^{+2.73}_{-2.73}$	$48.09^{+2.02}_{-2.02}$	$27.20^{+1.13}_{-1}$	16^{+1}_{-1}	$10.31^{+0.43}_{-0.43}$
dilepton mass	105^{+4}_{-4}	91^{+4}_{-4}	$64.21^{+2.71}_{-2.71}$	$47.83^{+1.99}_{-1.99}$	$27.06^{+1.12}_{-1}$	16^{+1}_{-1}	$10.26^{+0.42}_{-0.42}$
LAr hole jet	104^{+4}_{-4}	90^{+4}_{-3}	$63.56^{+2.46}_{-2.39}$	$47.24^{+1.77}_{-1.77}$	$26.75^{+1.00}_{-1}$	16^{+1}_{-1}	$10.14^{+0.39}_{-0.38}$
jet mult	75^{+4}_{-4}	68^{+3}_{-3}	$51.49^{+2.37}_{-2.31}$	$39.49^{+1.69}_{-1.69}$	$23.12^{+0.90}_{-1}$	$14.21^{+0.46}_{-0.45}$	$9.03^{+0.25}_{-0.24}$
Δr jet	73^{+1}_{-1}	66^{+1}_{-1}	$49.99^{+0.64}_{-0.63}$	$37.87^{+0.44}_{-0.46}$	$20.64^{+0.25}_{-0}$	$10.51^{+0.12}_{-0.12}$	$5.62^{+0.06}_{-0.06}$
$N_J \geq 3$	35^{+2}_{-1}	33^{+2}_{-1}	$27.52^{+1.16}_{-0.94}$	$21.76^{+0.83}_{-0.67}$	$12.50^{+0.43}_{-0.35}$	$6.74^{+0.23}_{-0.19}$	$3.71^{+0.12}_{-0.10}$
$N_J \geq 4$	$9.75^{+0.43}_{-0.35}$	$9.64^{+0.41}_{-0.34}$	$8.69^{+0.32}_{-0.31}$	$7.02^{+0.28}_{-0.23}$	$4.31^{+0.16}_{-0.14}$	$2.38^{+0.08}_{-0.07}$	$1.31^{+0.05}_{-0.04}$
$N_J \geq 5$	$1.34^{+0.10}_{-0.10}$	$1.52^{+0.09}_{-0.09}$	$1.56^{+0.07}_{-0.07}$	$1.27^{+0.06}_{-0.06}$	$0.85^{+0.03}_{-0.03}$	$0.45^{+0.02}_{-0.02}$	$0.25^{+0.01}_{-0.01}$

Table 6.2.: Expected number of signal events, $|F| = 3$, after cuts.

6.5. Treatment of Uncertainties

As mentioned before, there are several sources of uncertainties that have to be treated carefully. The sources of uncertainty that were considered for this study are the following:

- Statistical uncertainties on the data and Monte Carlo (Poisson uncertainties).
- An uncertainty on the luminosity measurement of 3.7%.
- Uncertainties on the predicted cross sections of the background processes, given in Table A.2.
- Uncertainties on the jet energy scale. These were treated by using the `MultijetJESUncertaintyProvider` tool [45] to recalibrate the jet energies, and re-doing the analysis with the new jet energy scales. The new histograms were compared bin-by-bin to the one obtained from the nominal jet energy scale. If the nominal bin content was between the two error histograms, the differences to the nominal histogram were taken as the upper and lower uncertainty. Otherwise, the maximal difference was taken as the uncertainty in one direction, and the uncertainty in the other direction was set to 0.
- The uncertainty on the jet energy resolution was also dealt with using the `MultijetJESUncertaintyProvider` tool [45]. However, it is only possible to smear the jet energies, not to unsmear them. Each histogram was filled after smearing the jets. Then the absolute difference to the nominal histogram was taken as both upper and lower uncertainties. Unfortunately, the jet energy scale and resolution uncertainties, as well as the recalibration constants, were only extracted from 2010 data, not from the 2011 data that was used here. The 2010 values were used as a conservative estimate for the uncertainties.
- The uncertainties on the electron energy scale/resolution and electron identification/reconstruction efficiencies were treated in the same way as the jet energy scale uncertainties above, using the tools `EnergyRescaler` [46] and the `egammaSFclass` [42].

The uncertainties on the jet energy scale are the dominant uncertainties after requiring at least two jets.

All background uncertainties but the statistical uncertainties and uncertainties on the background cross section were taken to be correlated between the samples, meaning that these uncertainties were simply added to obtain the uncertainty on the background prediction. All sources of uncertainties were taken to be uncorrelated amongst each other and hence added in quadrature. The statistical uncertainty on the data is not added to the Monte Carlo uncertainties, but shown separately.

6.6. Comparison between Data and Simulation

In order to validate the MC simulations and check that all important kinematical features of the background processes are reproduced correctly in the simulation, a number of comparisons has been performed in regions of the phase space where it is expected that background processes are dominant, i.e. where any signal contribution should be well within the systematic uncertainties of the simulations. These background processes can be found colour-coded in Fig. 6.1a. The backgrounds are plotted as stacked histograms, with a grey band showing the systematic uncertainty of the sum of all backgrounds. At the bottom of the plots, the ratio of observed data over background prediction is shown, with the systematic uncertainties in yellow. The signal distributions are plotted on top of the background expectations, but not added to them. Here, a form factor of $|F| = 3$ was chosen so that the signal would still be visible.

6.6.1. Pile-up Reweighting

To ensure that pile-up conditions were reproduced correctly in the simulations, the simulated events were reweighted according to the average number of interaction vertices per run period, μ. As a cross check, μ is plotted in Fig. 6.1b. It can be seen that data and MC simulations agree well within systematic uncertainties. There were no simulations available for $\mu < 2.5$ and $\mu > 17$. However, the number of data points in these ranges is small compared to the rest, so the missing simulations can be neglected safely.

6.6.2. Mass and Momentum of the Z candidate

Fig. 6.2a shows the invariant mass of the Z candidates (opposite-sign electron pairs), before any requirements on the jet multiplicity. The observations agree quite well with

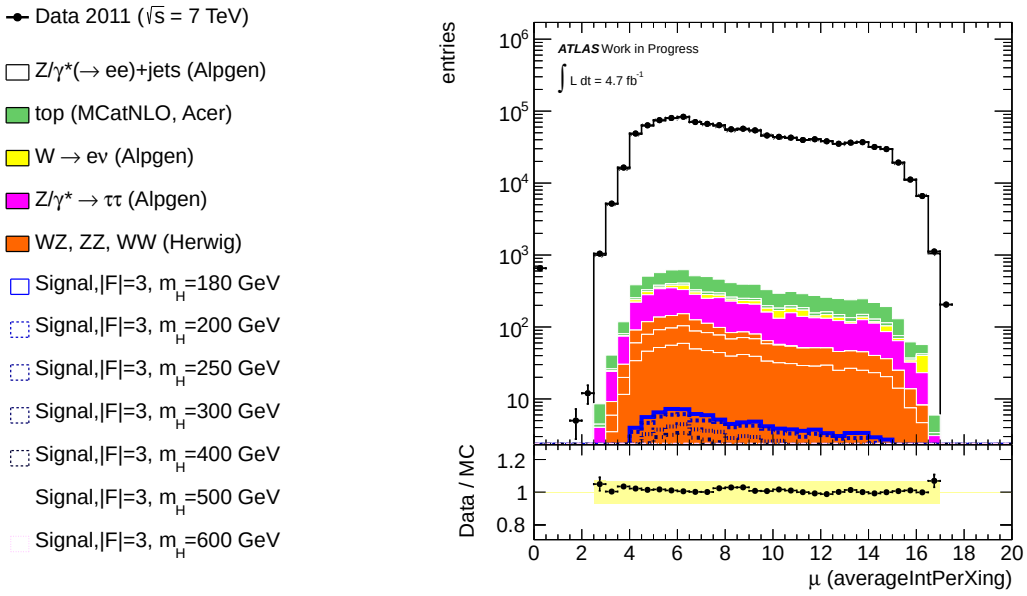

(a) **(b)**

Figure 6.1.: Left: Legend, valid for all plots in this section. Right: Measured and simulated distributions for the average number of interaction vertices per bunch crossing.

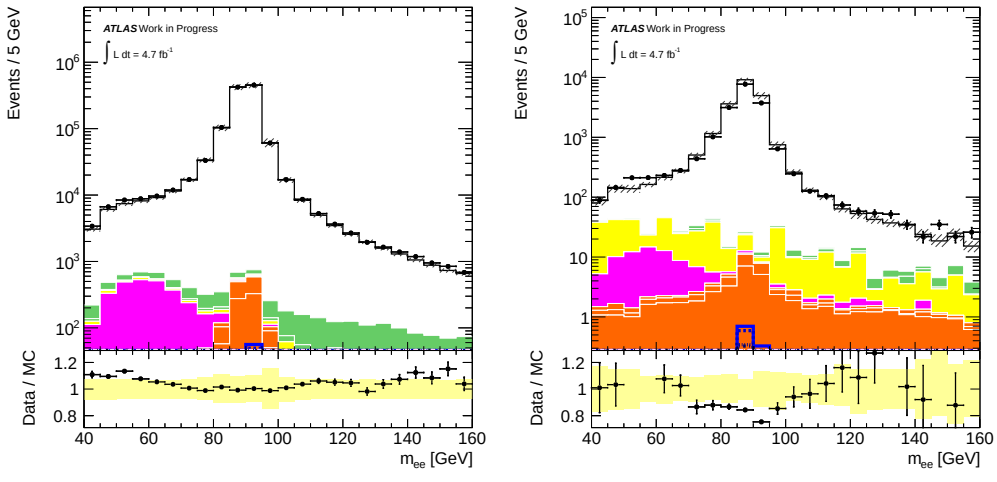

(a) **(b)**

Figure 6.2.: Measured and simulated distributions for the dielectron mass, no jet requirements. Left: Opposite sign electron pairs. Right: Same-sign electron pairs.

the data within the uncertainties, especially for the mass range that was used for the later analysis. The background is dominated by $Z \rightarrow e^+e^-$ events, as expected.
In Fig. 6.2b, the corresponding contribution for *same-sign* electron pairs is shown. One can again see a peak around the Z mass, even though the overall number of events is much smaller than in the opposite-sign case. The background is dominated by $Z \rightarrow e^+e^-$ events (where the charge of one electron was misidentified). Again, one can see a reasonable agreement between simulation and data in most regions, accounting for the large statistical uncertainties on the data. Around the Z mass of about $90\,\text{GeV}$, there is actually a small dip in the data compared to simulations, indicating that the charge misidentification rate might have been overestimated slightly. Together, these two plots show that the QCD-background processes, where one observes two electrons from hadronic jets, have been successfully suppressed by the isolation requirements and one is justified in neglecting them. If a non-neglegible amount of "fake" electrons had been present here, one would have expected a flat shape of the dielectron spectrum, which should have the same size for the same-sign as for the opposite-sign case. This flat offset to the dielectron mass distribution is *not* observed in data.
In Fig. 6.3a, the transverse momentum of the Z candidate is plotted after the cut on the Z mass, but again before any requirements on the jet multiplicity. The simulated p_T distribution agrees well with the data after the reweighting procedure. The deviations for larger p_T are statistical fluctuations: Due to the low number of events in this range, larger bins were chosen for the p_T reweighting for events with a Z candidate p_T larger than $100\,\text{GeV}$.
The rapidity distributions of the Z candidate are shown in Fig. 6.3b. There is a slight hint that the data tend to have more central Z than the simulation, but simulation and data also agree within the systematics.

6.6.3. Electron Kinematics

The transverse momenta of the leading and second leading electron are shown in Fig. 6.4a and 6.5a, after the Z mass cut but before any jet requirements. There seems to be a slight excess in data in the lowest bin. However, this is not present anymore after requiring at least one jet in the event (see Fig. 6.4b and 6.5b). With this requirement, the background still dominates over the signal and the background simulations agree with the data within systematic uncertainties.
The corresponding pseudorapidity distributions are shown in Fig. B.2a to B.3b in the

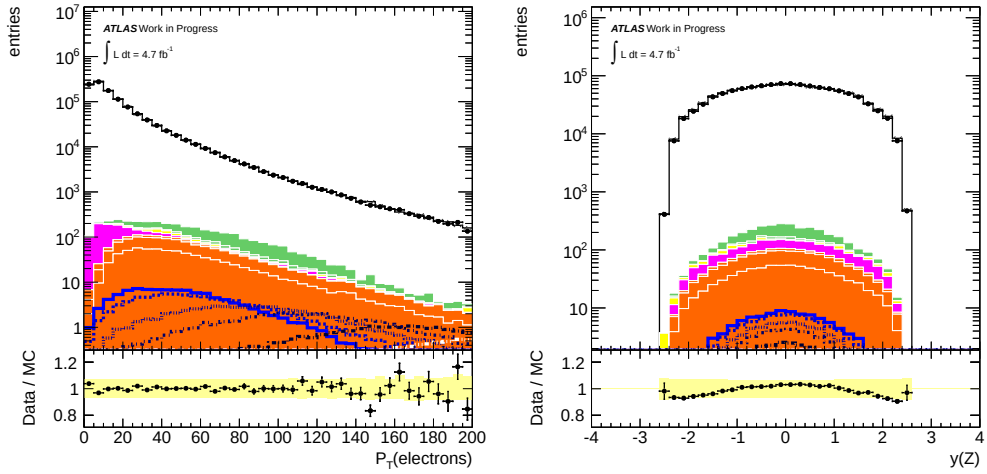

(a) **(b)**

Figure 6.3.: Measured and simulated distributions for the Z candidate p_T and Y, after Z mass cut, no jet requirements.

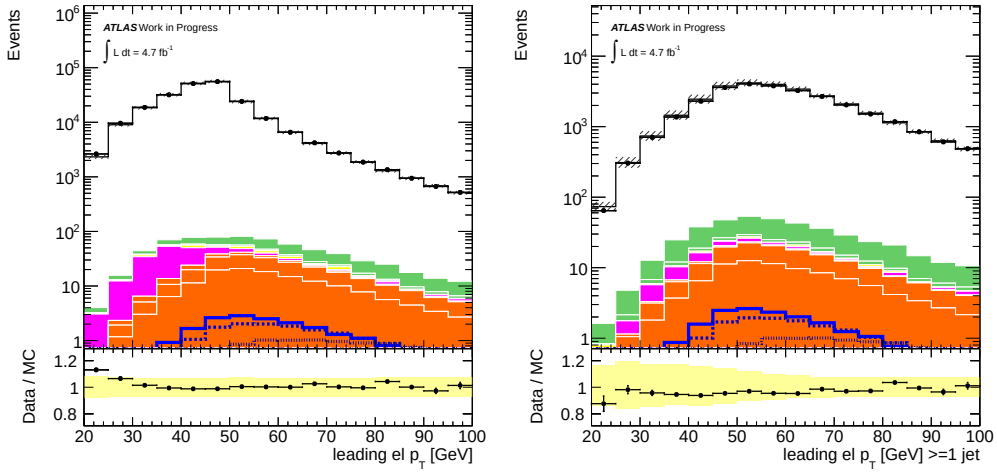

(a) **(b)**

Figure 6.4.: Measured and simulated distributions for the p_T of the leading electron, after Z mass cut. Left: no jet requirement. Right: at least one jet.

appendix. Again, data and simulations agree quite well, except for the area around the cracks in the calorimeter. However, this only affects a negligibly small number of events.

6.6.4. Jet Multiplicity and Kinematics

The jet multiplicity distributions are shown in Fig. 6.6a. The simulations predict slightly more jets than are observed, but data and simulation agree within systematics.
The transverse momentum distributions for the four leading jets are shown in Fig. 6.7a to 6.7d. Generally, the simulations tend to overestimate the number of jets, which was also seen in the jet multiplicity distribution. This is slightly problematic since many of the variables used for the BDT analysis of section 6.7 depend on the correct simulation of the jet p_Ts. Other combinations of MC generators (`Sherpa` [47] and `Alpgen+pythia`) were tested, but do not describe the measured jet p_T spectrum better. However, data and simulations agree within statistical and systematic uncertainties, which are quite large, especially for larger jet p_T.
The corresponding pseudorapidity distributions are shown in Fig. B.4 in the appendix. Again, data and simulations agree quite well within systematics.

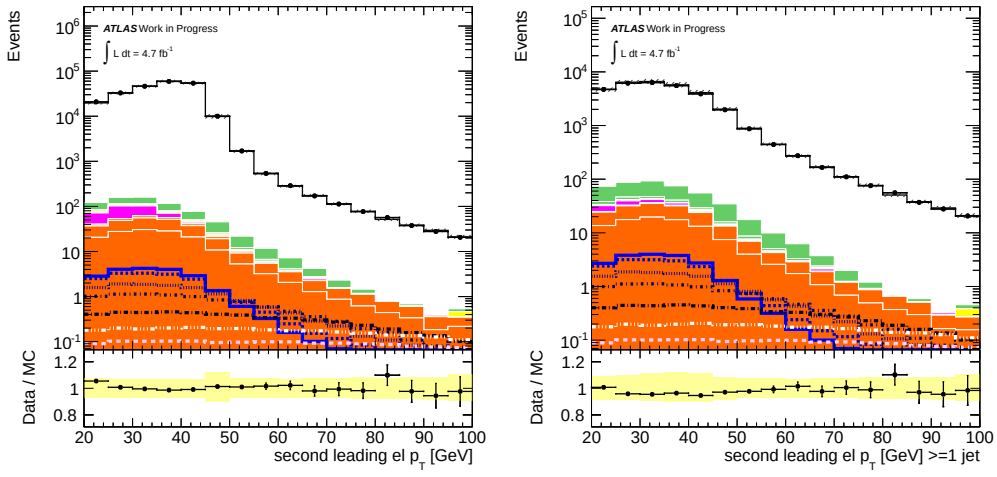

(a) **(b)**

Figure 6.5.: Measured and simulated distributions for the p_T of the second leading electron, after Z mass cut. Left: no jet requirement. Right: at least one jet.

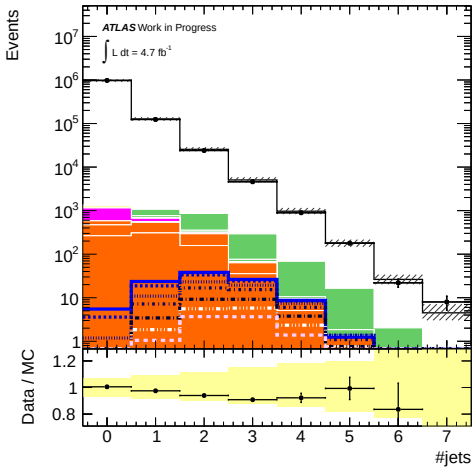

(a)

Figure 6.6.: Measured and simulated distributions jet multiplicity, after Z mass requirement.

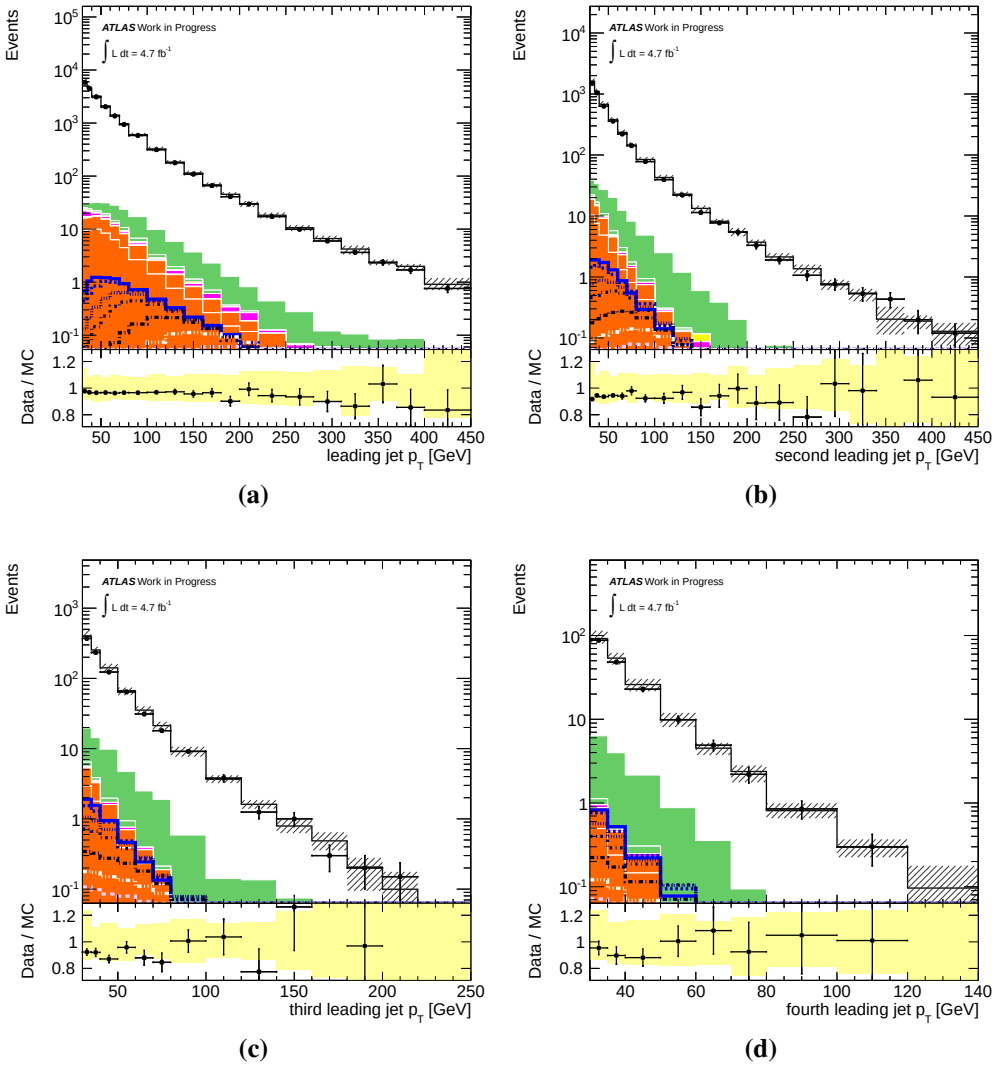

Figure 6.7.: Measured and simulated distributions of the p_T of the first four leading jets, after Z mass requirement.

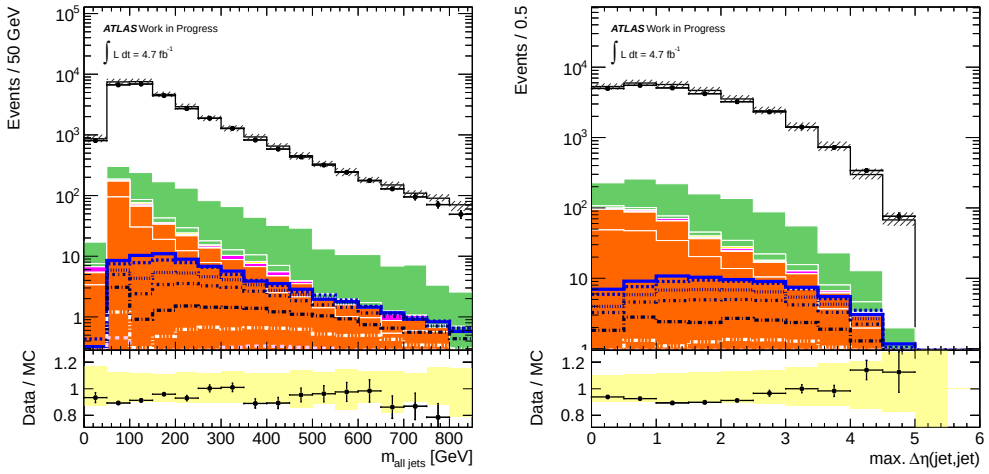

Figure 6.8.: Control distributions, after Z mass requirement; at least two jets. Left: Invariant mass of the up to four jets with the highest p_T in the event. Right: Maximal η difference amongst the four jets with the highest p_T in the event.

6.6.5. Other BDT Input variables

The invariant mass of all jets in the event is shown in Fig. 6.8a. Fig. 6.8b shows the maximal η difference amongst the four jets with the highest p_T in the event. Both observables are used in the BDT analysis, as the signal events are expected to have larger combined invariant masses and larger $\Delta(\eta)_{max}$. In the plots shown here, all events with at least two jets were used, to ensure that the background still dominates. One can see that the background simulations agree well with the data within the uncertainties. The $\Delta(\eta)_{max}$ shape seems to be slightly different for data and simulated background, with an excess in data for large $\Delta(\eta)_{max}$, where one would also expect a signal. However, this excess lies well within the systematic and statistical uncertainties.

The other variables used for the BDT analysis, M_{13} and $p_{T,13}$ for events with three jets, as well as M_{14}, $p_{T,14}$, M_{23}, and $p_{T,23}$ for events with four or more jets, are shown in Fig. B.1 and Fig. B.5 in the appendix. One can see that data and simulations agree within the uncertainties. However, both statistical and systematic uncertainties are large, especially in the regions where one might expect some signal events. This was one of the reasons why it was decided not to unblind the data yet.

Fig. 6.9 shows the distribution of the invariant mass of the inner two jets and the two electrons from the Z candidate in events with at least four jets, after the Z mass requirement. For signal events, this should and does peak around the Higgs mass used

for the simulations, while it peaks at lower masses for the background. Again, the systematic and statistical uncertainties are rather large.

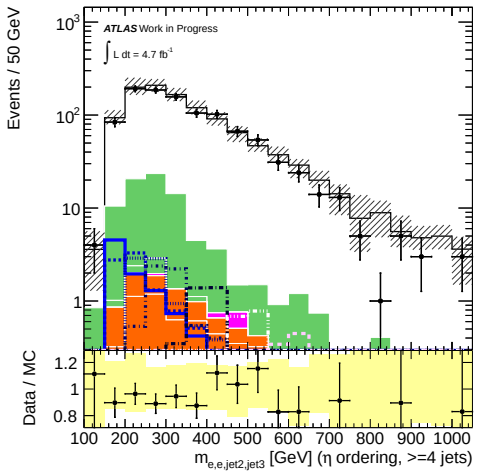

Figure 6.9.: Measured and simulated distribution of the invariant mass of the inner two jets and the two electrons from the Z candidate in events with at least four jets, after Z mass requirement.

6.7. Boosted Decision Tree Analysis

This part of the analysis was conducted using the TMVA package [32].The samples were split into two disjoint subsamples each; one with exactly three jets, one with four or more jets. For each Higgs mass, two sets of boosted decision trees were trained with a slightly different variable selection depending on the number of jets. The variables used were:

- For the three-jet selection: p_T of the two jets with the highest p_T and the two electrons, $\Delta(\eta)_{max}$, M_{13}.
- For the four-jet selection: p_T of the two jets with the highest p_T and the two electrons, $\Delta(\eta)_{max}$, M_{14}, M_{23}, M_{ee23}

The trees were trained against all the background processes. The relevant options used for this analysis are:

- `Trees=850`: Total number of decision trees to be created.
- `nEventsMin=150`: Minimum number of events required in a leaf.
- `MaxDepth=3`: Maximal depth of each decision tree.
- `BoostType=AdaBoost`: Using the AdaBoost algorithm.
- `AdaBoostBeta=0.5` β-parameter of AdaBoost algorithm.
- `SeparationType=GiniIndex`: Using the Gini-index as a measure of separation power.
- `nCuts=20`: Number of steps during node cut optimisation when creating each decision tree.
- `PruneMethod=NoPruning`: No pruning (i.e. removal of branches with too few events).

To check for overtraining, each sample was again split into two parts. One half was used for training and the other as a testing sample. The responses of the testing and training samples for $m_{H^\pm} = 180\,\text{GeV}$ can be seen in Fig. 6.10 for the four-jet channel. One can see that there is indeed some overtraining, but it is not a big problem in

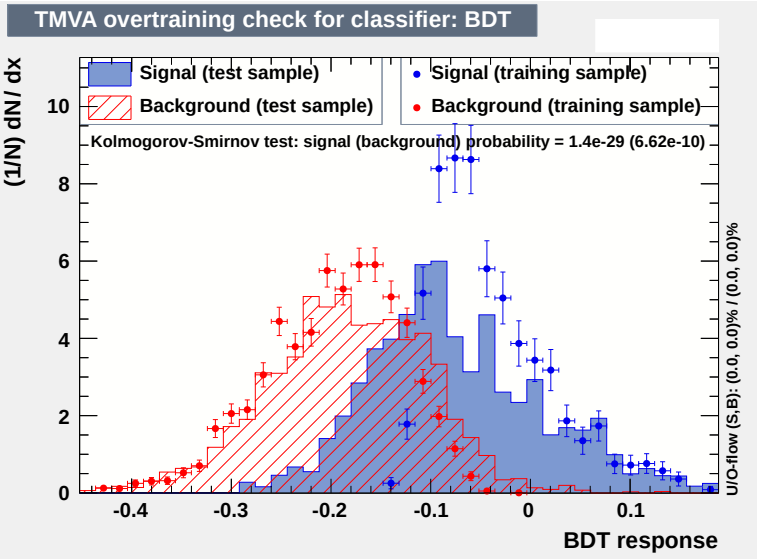

Figure 6.10.: BDT output for training and testing samples, four-jet channel, $m_{H^\pm} = 180\,\text{GeV}$.

relevant cut region. However, samples with more statistics are needed to make sure that there is no bias in the simulated output response. Additional samples have been requested but are not available at the time that this text is written. The control plots for the other Higgs masses and channels can be found in section B.2 in the appendix.

To obtain limits on the cross section, a cut value for the BDT response needs to be specified. One can then do a counting experiment, taking the expected number of background events from the simulations, and obtain an estimate on how may signal events there might be.

In a first look at the output of the decision trees, only the statistical significance was considered, given by $Z = \sqrt{2 \cdot \left((S+B)\log\left(1+\frac{S}{B}\right) - S\right)}$ (from [48]), where S is the expected number of signal events (after the cut) and B is the expected number of background events (after the cut). One can now choose the cut value so that Z is maximised, to obtain the best possible limits on S. This approach assumes that the background is known perfectly, as well as the signal shape, and can therefore be used to obtain the *best possible* significance.

This measure for the significance was just used for a preliminary study. For the observed limits, the full systematic uncertainties were taken into account.

Fig. B.9a (in the appendix) shows the statistical significance for the three-jet channel, $m_{H^\pm} = 180\,\text{GeV}$, $|F| = 3$. Fig. 6.11 shows the same for the four-jet channel. It can be seen that the three-jet channel proves to be rather inefficient: The statistical

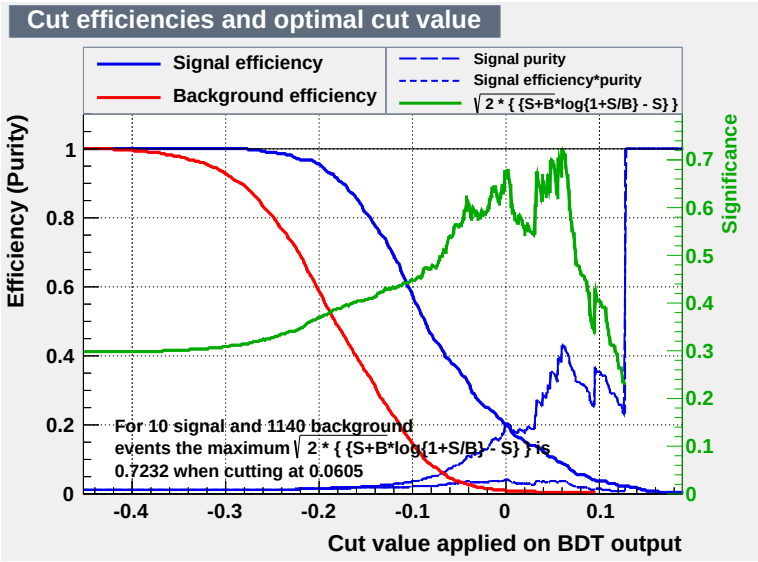

Figure 6.11.: BDT output for training and testing samples, four-jet channel, $m_{H^\pm} = 180\,\text{GeV}$.

significances for the optimal cut is approximately 0.35, while for the four-jet channel it is about 0.7. The results for the other masses can be found in section B.3 in the appendix. They all show similar performance differences. *As a result, the three-jet channel was not used for further analysis.*

All decision trees for the four-jet channel were then run on all signal and background samples, including the samples with varying scales etc., to obtain the systematic uncertainties on the output of the boosted decision trees. The results are shown in section B.4. It can be seen that the total uncertainty is quite large. This may be a hint that the chosen procedure (treating all uncertainty sources as independent and uncorrelated) is not applicable here, since the BDT output is not necessary a smooth function of the input values (meaning that a small change in the input might lead to a drastically different response from the BDT).

In particular, at the endpoints of the BDT response spectrum, the lower limit for the expected number of events often becomes negative for some bins. This is obviously unphysical. Since the software used for the limit setting can only deal with symmetric errors, the cut values for the BDT response were chosen to give the lowest expected limit, under the conditions that the uncertainties were less than 100% and such that they were approximately symmetric. Tab. 6.3 gives the expected number of background and signal events after the cuts, as well as the symmetrised relative uncertainties.

$m_{H^\pm}$ [GeV]	cut value	B_{exp}	σ_{exp} [fb]	$CL_{s,exp}$	$\lvert F\rvert_{exp}$
180	-0.04	38.5 ± 19.8	289.5	0.04972	5.92
200	-0.04	22.78 ± 13.71	263.5	0.04921	6.29
250	-0.04	8.64 ± 10.31	135.4	0.04991	5.66
300	-0.02	4.54 ± 7.22	114.8	0.04839	6.32
400	-0.08	24.34 ± 16.8	85.1	0.04947	7.58
500	0	3.61 ± 4.67	66.1	0.04915	8.89
600	0	3.32 ± 4.21	51.0	0.04940	10.12

Table 6.3.: Cut value on BDT response, expected number of background events after BDT cut, expected limit on signal cross section, expected CL_s and expected limit on $|F|$, assuming no other production or decay mode than via the $H^\pm W^\pm Z$ vertex.

6.8. Limits

The expected results of the counting experiment were converted into expected upper limits on the signal cross section, assuming that no signal is present. This was done by using the `TLimit` class within the ROOT framework, following the CL_s technique presented in [34]. The expected upper limit is defined as the smallest signal cross section for which $CL_s < 0.05$.

Under the assumption that there are no fermionic couplings of the charged Higgs and that the other Higgs bosons are too heavy to play a role in either production or decay, the cross section is simply proportional to $|F|^2$ and limits on the form factor $|F|$ can be obtained by dividing the expected limit by the expected cross section for $|F| = 1$. The results can be found in Tab. 6.3.

In contrast to the results from [19, 20], we do not find any sensitivity to $|F| \approx 1$. However, this is reasonable due to the fact that they assumed a much higher luminosity, and had no way to thoroughly treat detector effects or background processes.

6.9. Conclusion

In this chapter, it has been shown that it is possible to search for the process $H^{\pm} \rightarrow W^{\pm}Z^{0}$ with the ATLAS detector at the LHC. The observed data has been shown to agree with background simulations in regions dominated by background processes. No evidence for a charged Higgs boson decaying into $W^{\pm}$ and Z bosons was observed and expected limits for this process have been derived using boosted decision trees to combine several observables. However, due to large uncertainties on the background simulations, the expected limits are very large compared to theory expectations and no final conclusions can be drawn on the presence of signal in the data.
Especially the jet kinematics need to be studied further before one can take steps to unblind the data. It might be that the updated jet calibrations and jet energy scale/resolution uncertainties will reduce some of the discrepancies in the jet p_T spectrum. If this is not the case, one would have to find a way to estimate the main background contribution, $Z \rightarrow e^{+}e^{-}$+jets, from data, or to improve the simulations.
More statistics, especially at higher center-of-mass energy as they are expected for the 2012 run of the LHC, might also help to be more sensitive to the process.

7. Summary and Outlook

7.1. Summary

In this thesis, the phenomenology of the $H^{\pm}W^{\pm}Z$ vertex in the context of charged Higgs production and decay at the Large Hadron Collider at CERN has been examined. First, an introduction into the theoretical framework, the Standard Model of particle physics, was given. The basic setup of a detector at a hadron collider was explained, with a focus on the ATLAS detector at the LHC at CERN.

The "Boosted Decision Tree" technique, a multivariate analysis method used later on, was introduced and motivated. In addition, a limit setting procedure based on the CL_s technique was introduced.

The $lljj$ final state (where l can be an electron or muon) offers a search channel where the mass and the kinematics of the Higgs boson can be fully reconstructed. The features of this channel, especially the mass reconstruction, were explored in detail, using Monte Carlo simulations of $H^{\pm} \rightarrow W^{\pm}Z$ events. Some studies were also made in the trilepton (plus neutrino) final state, which has less background, but is not fully reconstructible.

The dominant background processes for the $l^{+}l^{-}jj$ final state at the ATLAS detector are summarised and analysed using Monte Carlo simulations. Looking at data, no evidence for the existence of a charged Higgs was found; all data seems to be described by the background simulations. Expected limits on the charged Higgs coupling to W and Z have been derived. However, due to large systematic and statistic uncertainties, no attempt at deriving limits from data has been made.

7.2. Outlook

The work in this search channel is far from over. This study has shown that the dominant background, $Z \rightarrow e^+e^-$ production with additional jets, is not well enough understood. In addition, the systematic uncertainties are still large, especially in the interesting regions. Improvements in understanding the jet energy measurements might help here, as might improved Monte Carlo predictions of the $Z \rightarrow e^+e^-$ background. More statistics in the Monte Carlo samples is needed to reduce overtraining of the boosted decision trees.

Another direction one could go in is to search for variables like ratios or angles that have small systematic uncertainties *and* are well described by the simulations, which so far have not been found.

After the $Z \rightarrow ee$ background has been understood, it will also be important to have a closer look at the SM diboson backgrounds, which have not been measured in this channel so far. Only when we are sure that all background sources are well understood can we unblind the data and actually look for the charged Higgs in the $H^{\pm}WZ^{\pm}$ vertex.

A. Software and Datasets

A.1. Data

Data from periods D to M from the 7 TeV proton-proton run of 2011, recorded with the ATLAS detector at the LHC, was used.

A.2. Signal Monte Carlo

A detailed listing of the MC samples used for the signal prediction can be found in Tab. A.1.

A.3. Background Monte Carlo

A detailed listing of the MC samples used for the background prediction can be found in Tab. A.2.

Higgs mass [GeV]	data set	σ [fb] $\cdot BR$	no. events
180	128560	8.27	50000
200	128561	6.67	50000
250	128562	4.23	50000
300	128563	2.87	50000
400	128564	1.48	50000
500	128565	0.837	50000
600	128566	0.498	50000

Table A.1.: Properties of Monte Carlo samples used for signal prediction, generated with `MadGraph` +`pythia`. σ refers to the leading order cross section, the branching rate is approximately 2.27%.

Process	N_p	data set	σ [pb]	$\frac{\Delta\sigma}{\sigma}$	k-factor	no. events	Note
Alpgen+Jimmy [49, 50]							
$Z \to ee$	0	107650	668.32	5%	1.25	6618284	$m_{ll} > 40$ GeV
	1	107651	134.36	5%	1.25	1334897	$m_{ll} > 40$ GeV
	2	107652	40.54	5%	1.25	809999	$m_{ll} > 40$ GeV
	3	107653	11.16	5%	1.25	220000	$m_{ll} > 40$ GeV
	4	107654	2.88	5%	1.25	60000	$m_{ll} > 40$ GeV
	5	107655	0.83	5%	1.25	20000	$m_{ll} > 40$ GeV
$Z \to ee + b\bar{b}$	0	109300	6.57	5%	1.25	150000	$m_{ll} > 40$ GeV
	1	109301	2.48	5%	1.25	100000	$m_{ll} > 40$ GeV
	2	109302	0.89	5%	1.25	40000	$m_{ll} > 40$ GeV
	3	109303	0.39	5%	1.25	10000	$m_{ll} > 40$ GeV
$Z \to \tau\tau$	0	107670	668.40	5%	1.25	10613179	$m_{ll} > 40$ GeV
	1	107671	134.81	5%	1.25	3334137	$m_{ll} > 40$ GeV
	2	107672	40.36	5%	1.25	1004847	$m_{ll} > 40$ GeV
	3	107673	11.25	5%	1.25	509847	$m_{ll} > 40$ GeV
	4	107674	2.79	5%	1.25	144999	$m_{ll} > 40$ GeV
	5	107675	0.77	5%	1.25	45000	$m_{ll} > 40$ GeV
$W \to e\nu$	0	107680	6921.60	5%	1.20	3458883	
	1	107681	1304.30	5%	1.20	2499645	
	2	107682	378.29	5%	1.20	3768632	
	3	107683	101.43	5%	1.20	1008947	
	4	107684	25.87	5%	1.20	250000	
	5	107685	7.00	5%	1.20	69999	
Herwig+Jimmy [22]							
WW		105985	11.50	5%	1.52	2489244	
WZ		105986	3.43	5%	1.58	999896	
ZZ		105987	0.97	5%	1.41	249999	
AcerMC [51]							
t, s-channel		117363	0.50	4.1%	1.00	199899	
t, t-channel		117360	6.94	4.2%	1.00	84353	
Wt		105500	15.74	6.7%	1.00	994897	
McAtNlo [52, 53]							
$t\bar{t}$		105200	90.57	$^{+10.3\%}_{11.0\%}$	1.00	1158183	not fully hadronic

Table A.2.: Properties of Monte Carlo samples used for background prediction. N_p refers to the number of additional partons in the Alpgen samples. σ refers to the leading order cross section (next-to-leading order for MCatNLO). The k-factor is used to correct the leading order cross section (from the MC generator) to the NLO cross section.

B. Tables and Plots

B.1. Data-MC Comparison

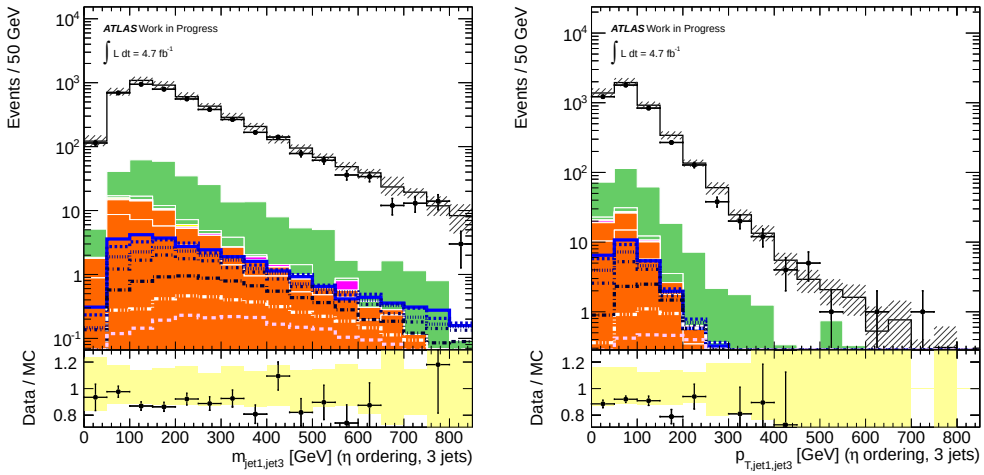

(a) **(b)**

Figure B.1.: Measured and simulated distributions for events with exactly tree jets, after Z mass cut. Left: invariant mass of the outer two jets. Right: combined p_T of the outer two jets.

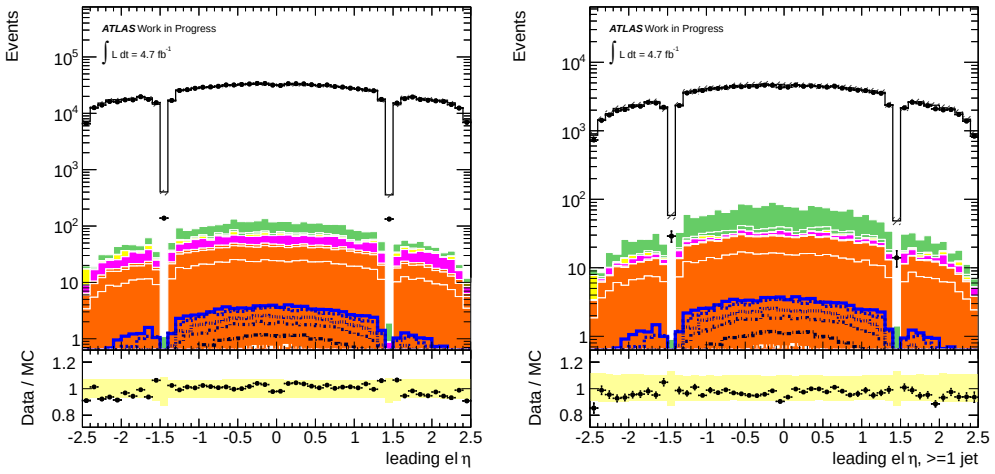

(a) **(b)**

Figure B.2.: Measured and simulated distributions for the η of the leading electron, after Z mass cut. Left: no jet requirement. Right: at least one jet.

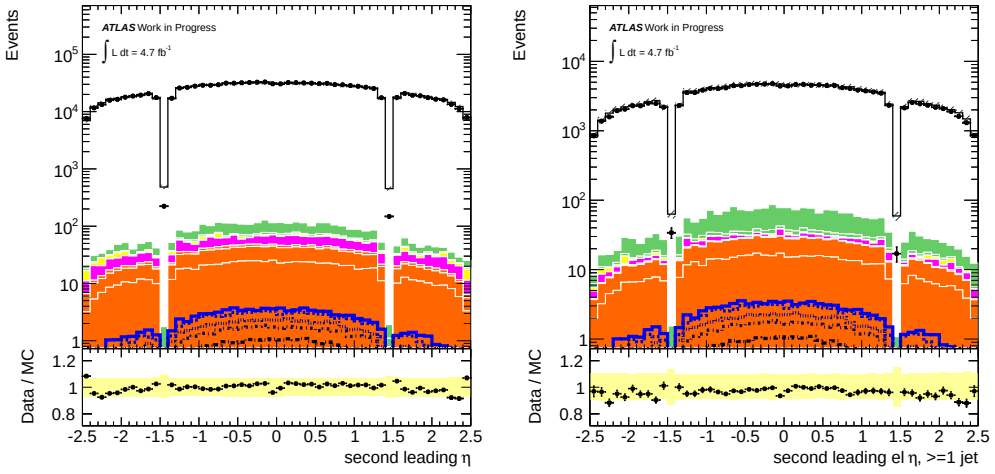

(a) **(b)**

Figure B.3.: Measured and simulated distributions for the η of the second leading electron, after Z mass cut. Left: no jet requirement. Right: at least one jet.

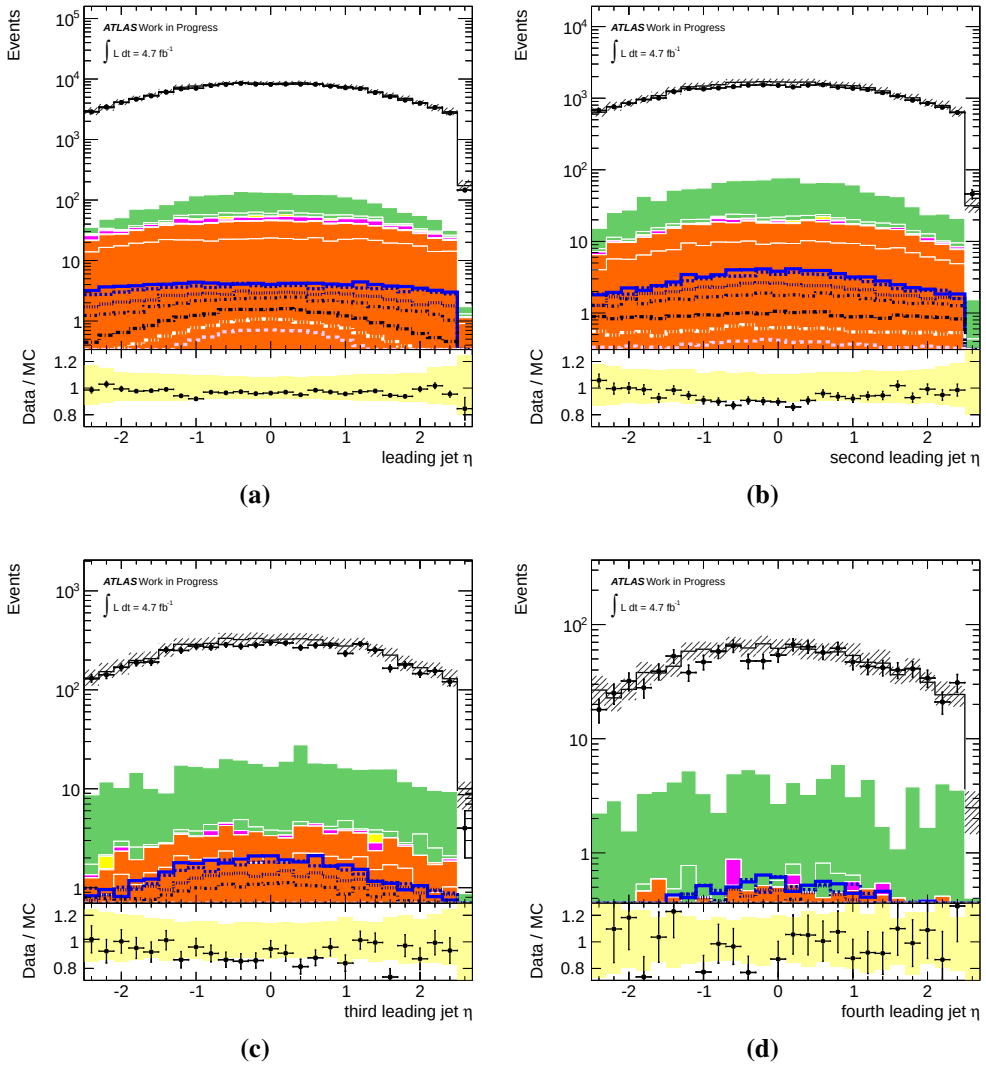

Figure B.4.: Measured and simulated distributions for the pseudorapidity of the first four jets, after Z mass requirement.

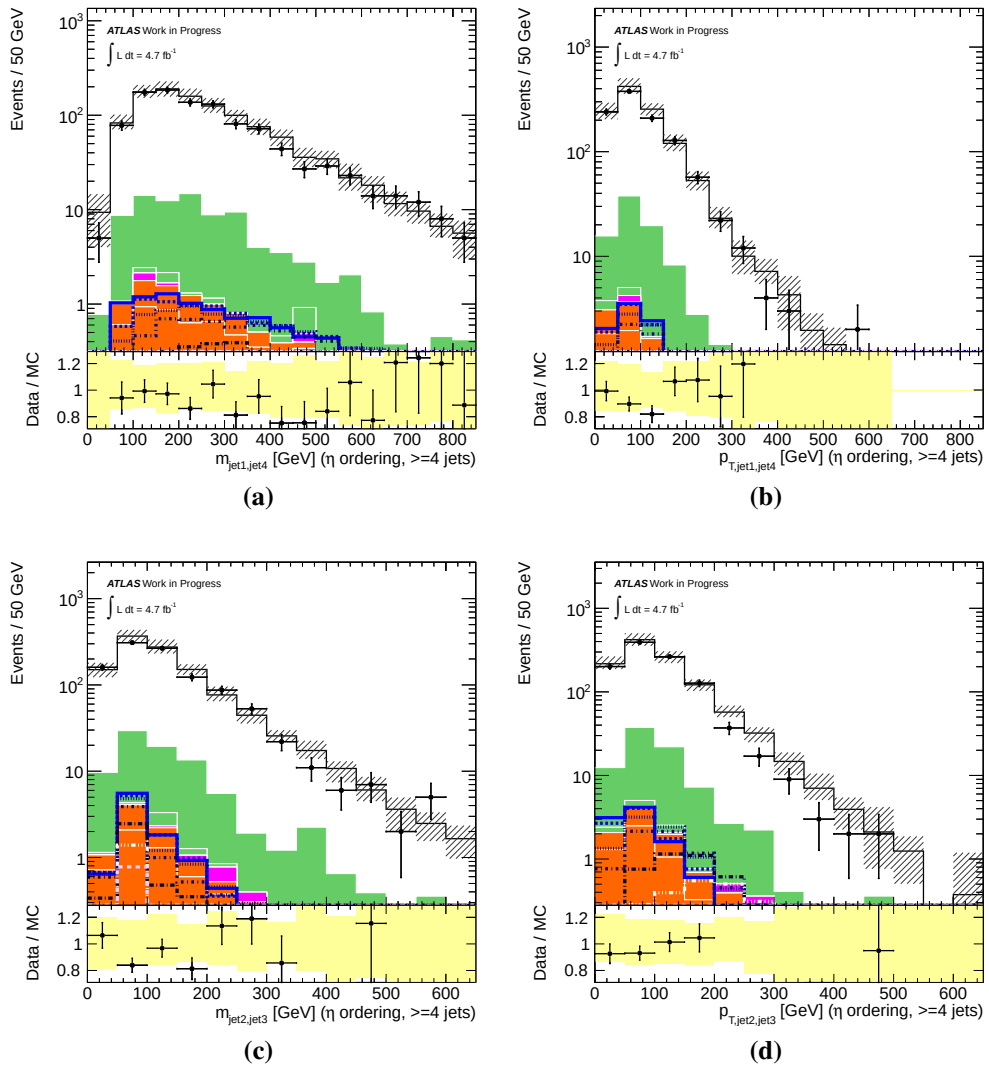

Figure B.5.: Measured and simulated distributions of event with at least four jets, after Z mass requirement. Top left: invariant mass of the outer two jets. Top right: combined p_T of the outer two jets. Bottom left: invariant mass of the inner two jets. Bottom right: combined p_T of the inner two jets.

B.2. BDT Control Plots

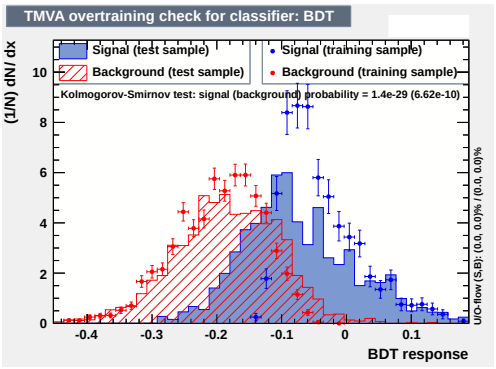

(a) $m_{H^\pm} = 180\,\text{GeV}$

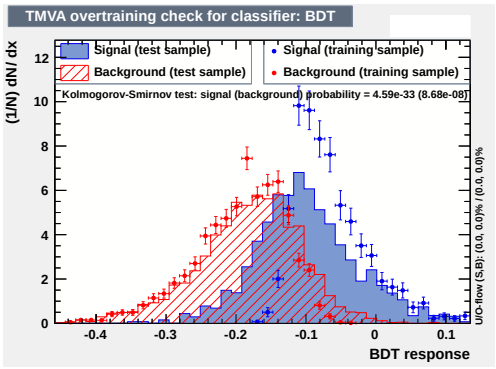

(b) $m_{H^\pm} = 200\,\text{GeV}$

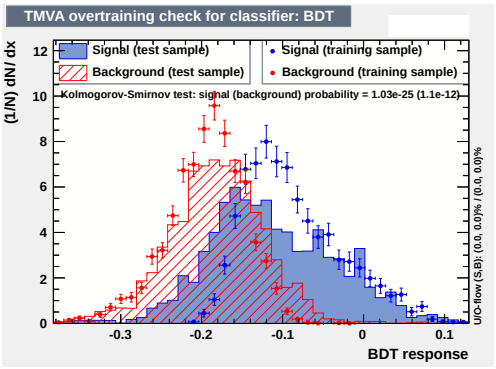

(c) $m_{H^\pm} = 250\,\text{GeV}$

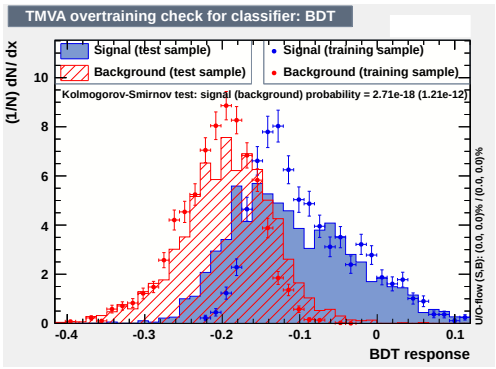

(d) $m_{H^\pm} = 300\,\text{GeV}$

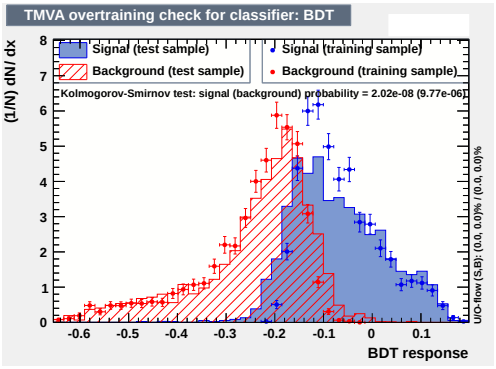

(e) $m_{H^\pm} = 400\,\text{GeV}$

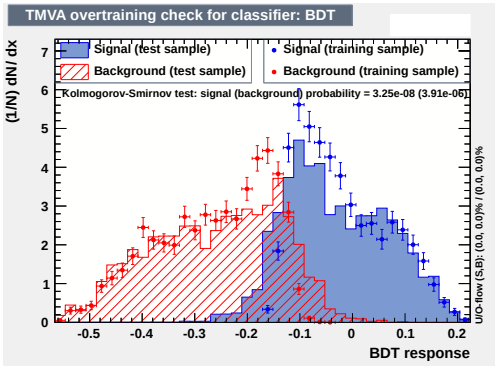

(f) $m_{H^\pm} = 500\,\text{GeV}$

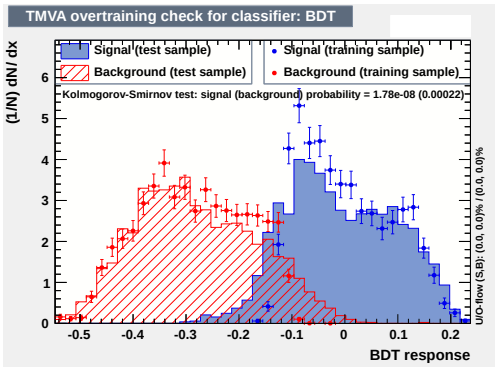

(g) $m_{H^\pm} = 600\,\text{GeV}$

Figure B.6.: BDT output for training and testing samples, four-jet channel.

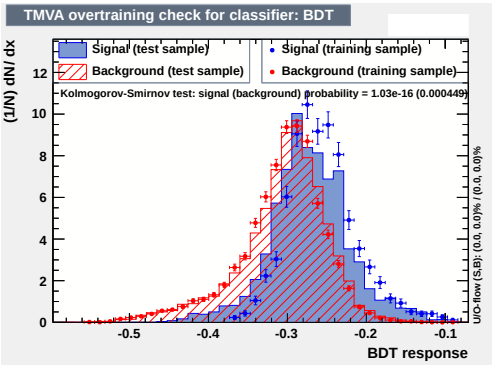

(a) $m_{H^\pm} = 180\,\text{GeV}$

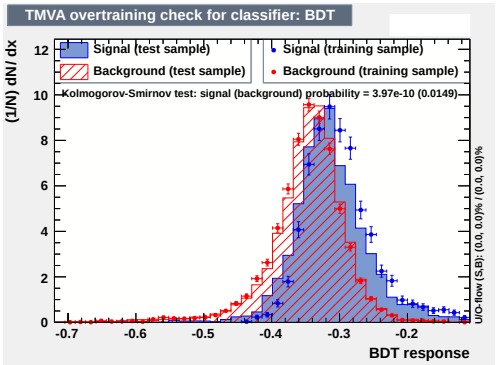

(b) $m_{H^\pm} = 200\,\text{GeV}$

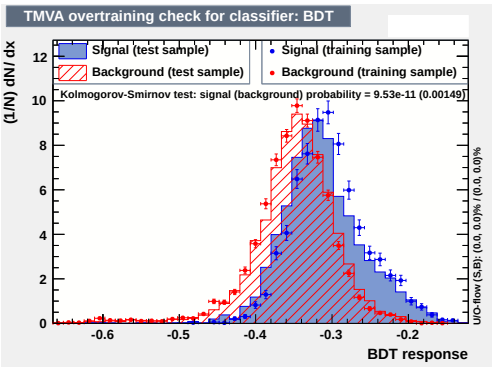

(c) $m_{H^\pm} = 250\,\text{GeV}$

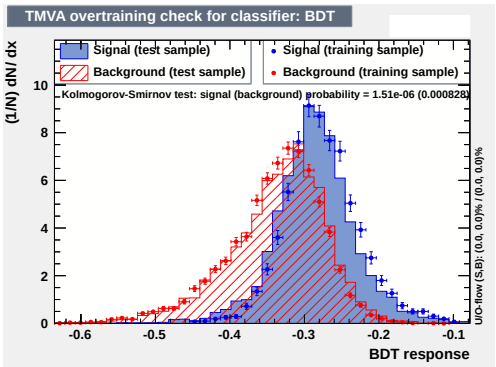

(d) $m_{H^\pm} = 300\,\text{GeV}$

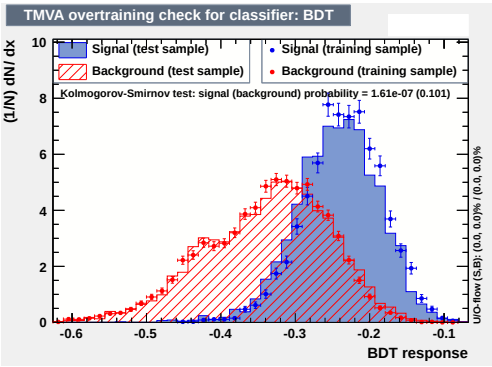

(e) $m_{H^\pm} = 400\,\text{GeV}$

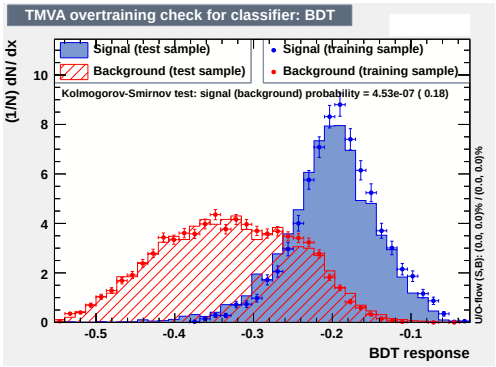

(f) $m_{H^\pm} = 500\,\text{GeV}$

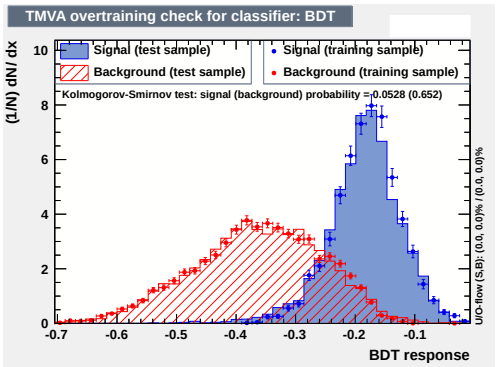

(g) $m_{H^\pm} = 600\,\text{GeV}$

Figure B.7.: BDT output for training and testing samples, three-jet channel.

B.3. BDT Cut Efficiencies

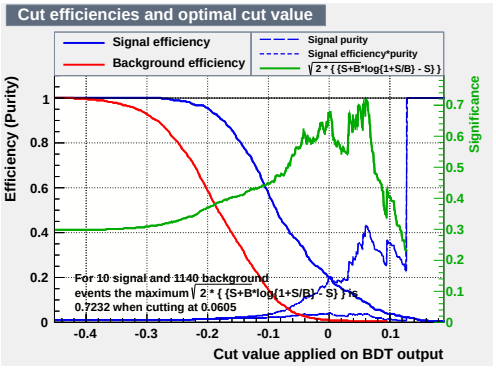

(a) $m_{H^\pm} = 180\,\text{GeV}$

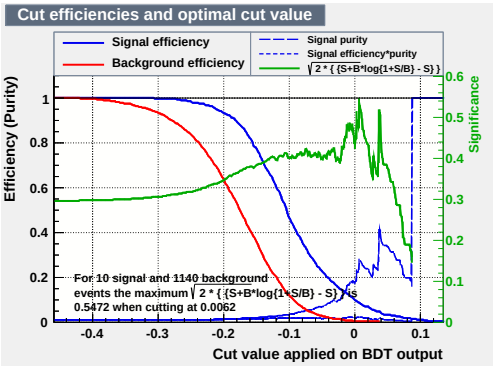

(b) $m_{H^\pm} = 200\,\text{GeV}$

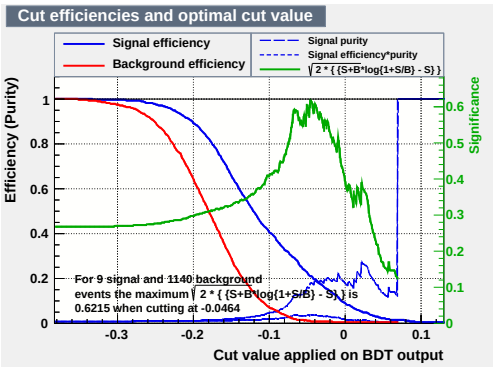

(c) $m_{H^\pm} = 250\,\text{GeV}$

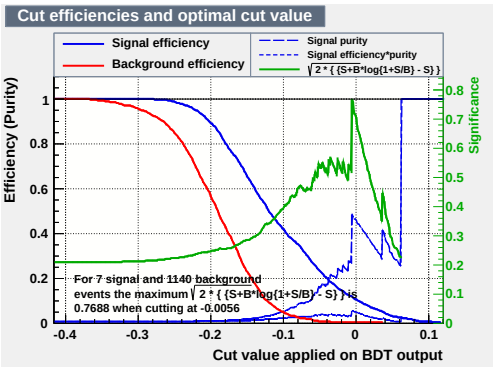

(d) $m_{H^\pm} = 300\,\text{GeV}$

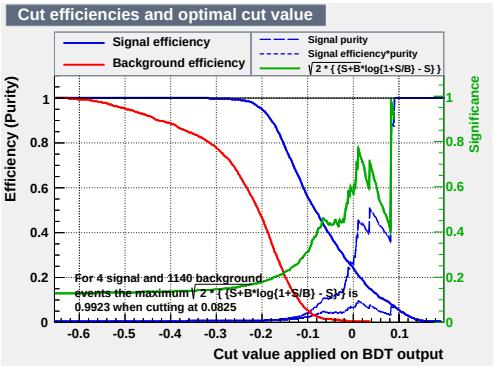

(e) $m_{H^\pm} = 400\,\text{GeV}$

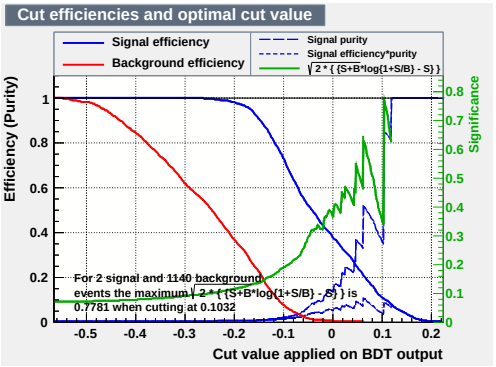

(f) $m_{H^\pm} = 500\,\text{GeV}$

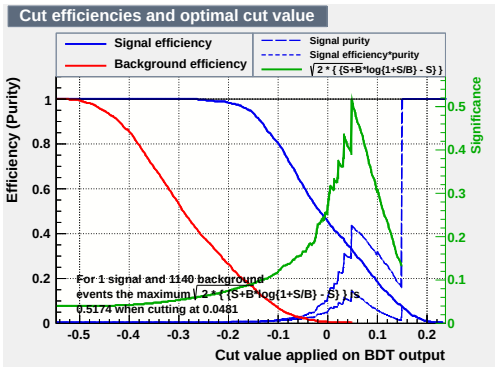

(g) $m_{H^\pm} = 600\,\text{GeV}$

Figure B.8.: BDT cut efficiencies, four-jet channel.

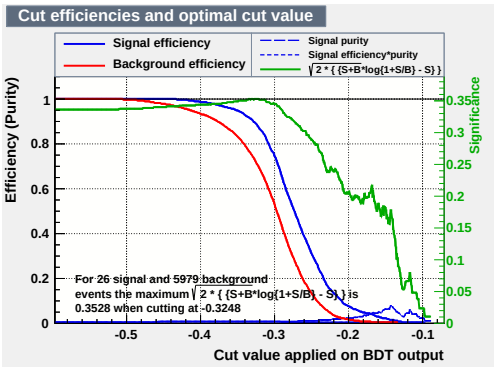

(a) $m_{H^\pm} = 180\,\text{GeV}$

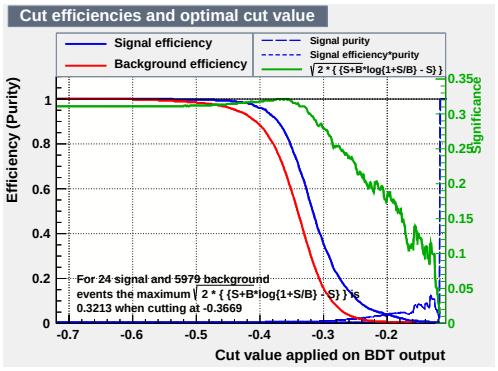

(b) $m_{H^\pm} = 200\,\text{GeV}$

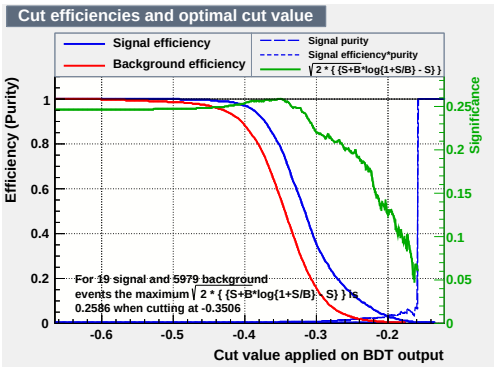

(c) $m_{H^\pm} = 250\,\text{GeV}$

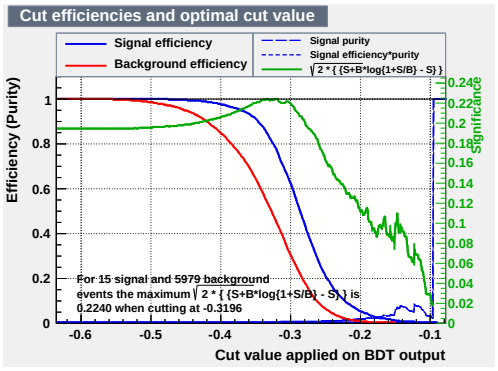

(d) $m_{H^\pm} = 300\,\text{GeV}$

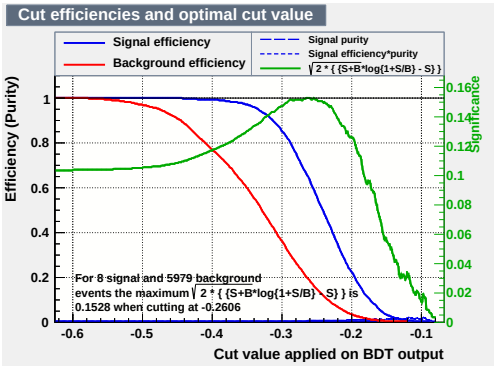

(e) $m_{H^\pm} = 400\,\text{GeV}$

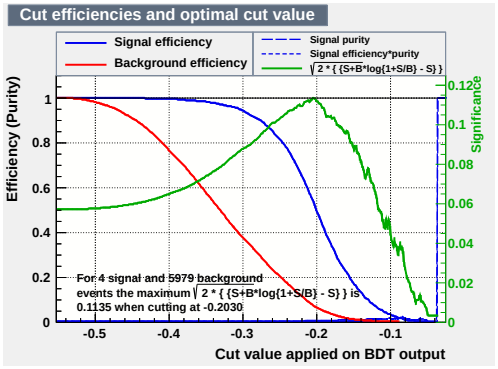

(f) $m_{H^\pm} = 500\,\text{GeV}$

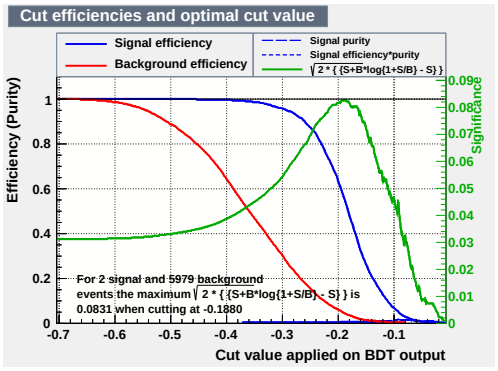

(g) $m_{H^\pm} = 600\,\text{GeV}$

Figure B.9.: BDT cut efficiencies, three-jet channel.

B.4. BDT Responses with Uncertainties

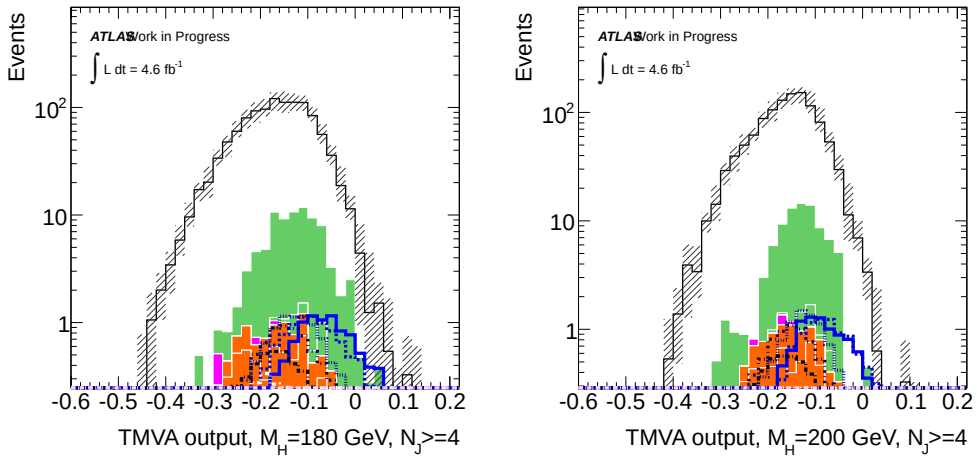

(a) BDT trained on $m_{H^\pm} = 180\,\text{GeV}$ **(b)** BDT trained on $m_{H^\pm} = 200\,\text{GeV}$

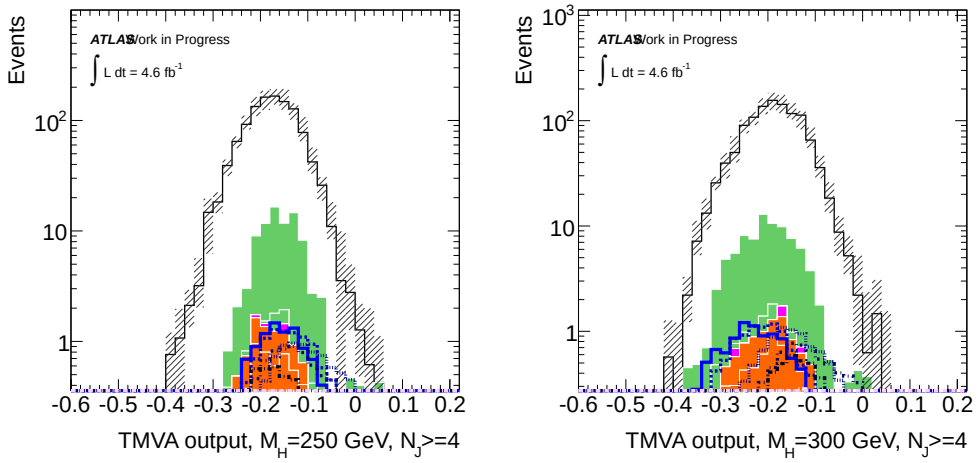

(c) BDT trained on $m_{H^\pm} = 250\,\text{GeV}$ **(d)** BDT trained on $m_{H^\pm} = 300\,\text{GeV}$

Figure B.10.: BDT response for background and signal simulations, four-jet channel.

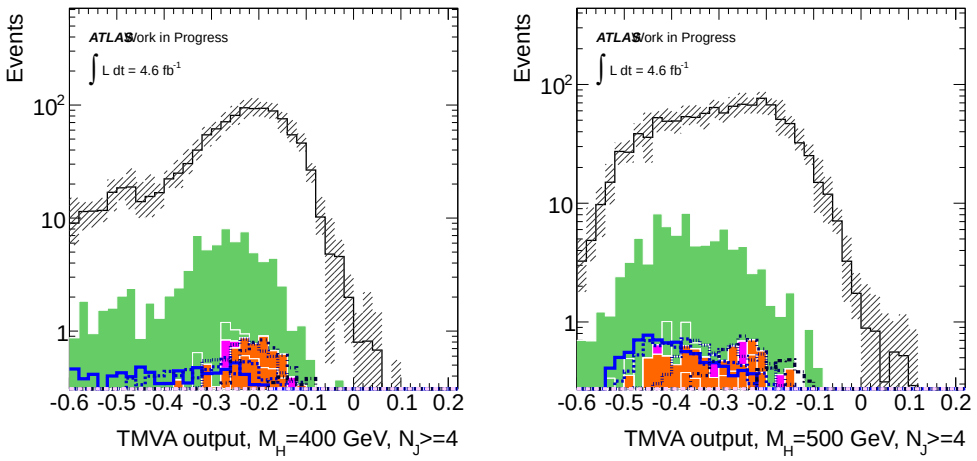

(a) BDT trained on $m_{H^\pm} = 400\,\text{GeV}$ **(b)** BDT trained on $m_{H^\pm} = 500\,\text{GeV}$

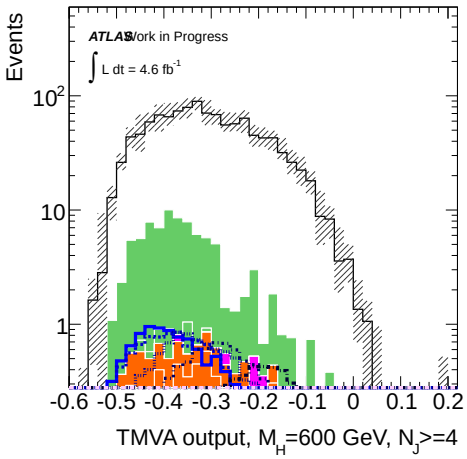

(c) BDT trained on $m_{H^\pm} = 600\,\text{GeV}$

Figure B.11.: BDT response for background and signal simulations, four-jet channel.

Bibliography

[1] D. Griffiths, "Introduction to Elementary Particles", Wiley-VCH, 2nd ed., 2008.

[2] F. Halzen and A. D. Martin, "Quarks and Leptons: An Introductory Course in Modern Particle Physics", Wiley, 1984.

[3] Y. L. Dokshitzer, "Calculation of the Structure Functions for Deep Inelastic Scattering and e+ e- Annihilation by Perturbation Theory in Quantum Chromodynamics", *Sov. Phys. JETP* **46** (1977) 641–653.

[4] G. Altarelli and G. Parisi, "Asymptotic Freedom in Parton Language", *Nucl. Phys.* **B126** (1977) 298.

[5] V. N. Gribov and L. N. Lipatov, "Deep inelastic e p scattering in perturbation theory", *Sov. J. Nucl. Phys.* **15** (1972) 438–450.

[6] J. Pumplin *et al.*, "New generation of parton distributions with uncertainties from global QCD analysis", *JHEP* **07** (2002) 012, `hep-ph/0201195`.

[7] K. Nakamura and P. D. Group, "Review of particle physics", *Journal of Physics G: Nuclear and Particle Physics* **37** (2010), no. 7A, 075021.

[8] J. F. Gunion, H. E. Haber, G. Kane, and S. Dawson, "The higgs hunter's guide", Perseus Books, 2000.

[9] G. S. Guralnik, C. R. Hagen, and T. W. B. Kibble, "Global conservation laws and massless particles", *Phys. Rev. Lett.* **13** Nov (1964) 585–587.

[10] P. Higgs, "Broken symmetries and the masses of gauge bosons", *Phys. Rev. Lett.* **13** Oct (1964) 508–509.

[11] F. Englert and R. Brout, "Broken symmetry and the mass of gauge vector mesons", *Phys. Rev. Lett.* **13** Aug (1964) 321–323.

[12] A. Djouadi, "Higgs Physics: Theory", arXiv:1203.4199.

[13] A. Djouadi, "The Anatomy of electro-weak symmetry breaking. I: The Higgs boson in the standard model", *Phys.Rept.* **457** (2008) 1–216, arXiv:hep-ph/0503172.

[14] M. Grünewald *et al.*, "Lep electroweak working group". http://lepewwg.web.cern.ch/LEPEWWG/Welcome.html.

[15] **LEP Working Group for Higgs boson searches, ALEPH, DELPHI, L3, OPAL** Collaboration, R. Barate *et al.*, "Search for the standard model Higgs boson at LEP", *Phys.Lett.* **B565** (2003) 61–75, arXiv:hep-ex/0306033.

[16] **TEVNPH (Tevatron New Phenomina and Higgs Working Group), CDF and D0** Collaboration, "Combined CDF and D0 Search for Standard Model Higgs Boson Production with up to 10 fb^{-1} of Data", 2012, FERMILAB-CONF-12-065-E.

[17] **ATLAS** Collaboration, "Combined search for the Standard Model Higgs boson using up to 4.9 fb-1 of pp collision data at sqrt(s) = 7 TeV with the ATLAS detector at the LHC", arXiv:1202.1408.

[18] **CMS** Collaboration, S. Chatrchyan *et al.*, "Combined results of searches for the standard model Higgs boson in pp collisions at sqrt(s) = 7 TeV", arXiv:1202.1488.

[19] E. Asakawa and S. Kanemura, "The $H^{\pm}W^{\mp}Z^0$ vertex and single charged Higgs boson production via W Z fusion at the Large Hadron Collider", *Phys. Lett.* **B626** (2005) 111–119, hep-ph/0506310.

[20] E. Asakawa, S. Kanemura, and J. Kanzaki, "Potential for measuring the $H^{\pm}W^{\mp}Z^0$ vertex from WZ fusion at the Large Hadron Collider", *Phys.Rev.* **D75** (2007) 075022, arXiv:hep-ph/0612271.

[21] T. Sjöstrand, S. Mrenna and P. Skands, "Pythia 6.4 physics and manual", *J. High Energy Phys.* **2006** (2006), no. 05, 026.

[22] G. Corcella *et al.*, "HERWIG 6.5: an event generator for Hadron Emission Reactions With Interfering Gluons (including supersymmetric processes)", *JHEP* **01** (2001) 010, hep-ph/0011363.

[23] J. Conway, "Pgs 4 - pretty good simulation of high energy collisions". http://physics.ucdavis.edu/~conway/research/software/pgs/pgs4-general.htm, April 2009.

[24] **GEANT4** Collaboration, S. Agostinelli *et al.*, "GEANT4: A Simulation toolkit", *Nucl.Instrum.Meth.* **A506** (2003) 250–303.

[25] C. Berger, "Elementarteilchenphysik", Springer, 2nd ed., 2006.

[26] **ATLAS** Collaboration, G. Aad *et al.*, "The atlas experiment at the cern large hadron collider", *Journal of Instrumentation* **3** (2008), no. 08, S08003.

[27] "The LHC Design Report", 2008.

[28] M. Cacciari, G. P. Salam, and G. Soyez, "The Anti-k(t) jet clustering algorithm", *JHEP* **0804** (2008) 063, arXiv:0802.1189.

[29] **ATLAS** Collaboration, G. Aad *et al.*, "Jet energy measurement with the ATLAS detector in proton- proton collisions at sqrt(s) = 7 TeV", arXiv:1112.6426.

[30] H.-J. Yang, B. P. Roe, and J. Zhu, "Studies of boosted decision trees for MiniBooNE particle identification", *Nuclear Instruments and Methods in Physics Research A* **555** (2005) 370–385, physics/0508045.

[31] Y. Freund and R. Schapire, "Experiments with a new boosting algorithm", in "Proc COLT", p. 209–217. ACM Press, New York, 1996.

[32] A. Hoecker, P. Speckmayer, J. Stelzer, J. Therhaag, E. von Toerne, and H. Voss, "TMVA: Toolkit for Multivariate Data Analysis", *PoS* **ACAT** (2007) 040, physics/0703039.

[33] R. J. Barlow, "Statistics", John Viley and Sons, 1989.

[34] A. L. Read, "Presentation of search results: the cl s technique", *Journal of Physics G: Nuclear and Particle Physics* **28** (2002), no. 10, 2693.

[35] A. L. Read, "Modified frequentist analysis of search results (the cl_s method). oai:cds.cern.ch:451614", 2000.

[36] T. Stelzer and W. F. Long, "Automatic generation of tree level helicity amplitudes", *Comput. Phys. Commun.* **81** (1994) 357–371, hep-ph/9401258.

[37] F. Maltoni and T. Stelzer, "MadEvent: Automatic event generation with MadGraph", *JHEP* **02** (2003) 027, hep-ph/0208156.

[38] J. Alwall, A. Ballestrero, P. Bartalini, S. Belov, E. Boos, *et al.*, "A Standard format for Les Houches event files", *Comput.Phys.Commun.* **176** (2007) 300–304, arXiv:hep-ph/0609017.

[39] **ATLAS** Collaboration, G. Aad *et al.*, "Search for a heavy Standard Model Higgs boson in the channel $H \to ZZ \to llqq$ using the ATLAS detector", arXiv:1108.5064.

[40] C. Buszello, I. Fleck, P. Marquard, and J. van der Bij, "Prospective analysis of spin- and CP-sensitive variables in $H \to ZZ \to l_1^+ l_1^- l_2^+ l_2^-$ at the LHC", *Eur.Phys.J.* **C32** (2004) 209–219, arXiv:hep-ph/0212396.

[41] "ExtendedPileupReweighting". Internal ATLAS TWiki page, April 1st 2012. https://twiki.cern.ch/twiki/bin/viewauth/AtlasProtected/ExtendedPileupReweighting.

[42] "EfficiencyMeasurements". Internal ATLAS TWiki page, April 1st 2012. https://twiki.cern.ch/twiki/bin/viewauth/AtlasProtected/EfficiencyMeasurements.

[43] **ATLAS** Collaboration, G. Aad *et al.*, "Measurement of the $W \to l\nu$ and $Z/\gamma^* \to l\bar{l}$ production cross sections in proton-proton collisions at sqrt(s) = 7 TeV with the ATLAS detector", *JHEP* **1012** (2010) 060, arXiv:1010.2130.

[44] **ATLAS** Collaboration, G. Aad *et al.*, "Measurement of the production cross section for Z/γ^* in association with jets in pp collisions at sqrt(s) = 7 TeV with the ATLAS detector", *Phys. Rev.* **D85** (2012) 032009, arXiv:1111.2690.

[45] "MultijetJESUncertaintyProvider". Internal ATLAS TWiki page, April 1st 2012. https://twiki.cern.ch/twiki/bin/viewauth/AtlasProtected/MultijetJESUncertaintyProvider.

[46] "EnergyRescaler". Internal ATLAS TWiki page, April 1st 2012. https://twiki.cern.ch/twiki/bin/viewauth/AtlasProtected/EnergyRescaler.

[47] T. Gleisberg *et al.*, "Event generation with SHERPA 1.1", *JHEP* **02** (2009) 007, arXiv:0811.4622.

[48] G. Cowan, K. Cranmer, E. Gross, and O. Vitells, "Asymptotic formulae for likelihood-based tests of new physics", *EUR.PHYS.J.C* **71** (2011) 1554, arXiv:1007.1727v2.

[49] M. L. Mangano, M. Moretti, F. Piccinini, R. Pittau, and A. D. Polosa, "ALPGEN, a generator for hard multiparton processes in hadronic collisions", *JHEP* **0307** (2003) 001, arXiv:hep-ph/0206293.

[50] F. Caravaglios, M. L. Mangano, M. Moretti, and R. Pittau, "A New approach to multijet calculations in hadron collisions", *Nucl.Phys.* **B539** (1999) 215–232, arXiv:hep-ph/9807570.

[51] B. P. Kersevan and E. Richter-Was, "The Monte Carlo event generator AcerMC version 2.0 with interfaces to PYTHIA 6.2 and HERWIG 6.5", arXiv:hep-ph/0405247.

[52] S. Frixione and B. R. Webber, "Matching nlo qcd computations and parton shower simulations", *Journal of High Energy Physics* **2002** (2002), no. 06, 029.

[53] S. Frixione, P. Nason, and B. R. Webber, "Matching nlo qcd and parton showers in heavy flavour production", *Journal of High Energy Physics* **2003** (2003), no. 08, 007.

Danksagung

First and foremost I would like to thank my referees, A. Quadt and S. Schumann. Thank you for giving me the opportunity to work on this project for my Master's thesis!
Many, many thanks to my immediate advisor in Göttingen, U. Blumenschein, who was always open for questions and advice and also helped me a great deal with this project.
Special thanks goes to my supervisors during my time in Uppsala, C. Buszello, R. Enberg and G. Ingelmann. Thank you for working with me and making my Erasmus exchange into a grat research experience!
A lot of thanks is also due to K. Bierwagen, who helped me settle in to the ATLAS software. Thanks for working with me and answering a lot of questions!
This whole work obviously could not have been done without the support of the ATLAS community and the other members of this institute as well as the THEP/experimental particle physics groups from Uppsala, unfortunately too many to name all.
Danke an Jan, Steffen und Nils für Korrekturlesen, Antreiben und viele hilfreiche Anmerkungen. Ich hoffe, es war nicht all zu langweilig für euch! Und nicht zu letzt vielen Dank an meine Eltern und meine Schwester Karoline für die Unterstützung und das Mut-Machen aus der Ferne.

Erklärung nach §18(8) der Prüfungsordnung für den Bachelor-Studiengang Physik und den Master-Studiengang Physik an der Universität Göttingen:

Hiermit erkläre ich, dass ich diese Abschlussarbeit selbstständig verfasst habe, keine anderen als die angegebenen Quellen und Hilfsmittel benutzt habe und alle Stellen, die wörtlich oder sinngemäß aus veröffentlichten Schriften entnommen wurden, als solche kenntlich gemacht habe.
Darüberhinaus erkläre ich, dass diese Abschlussarbeit nicht, auch nicht auszugsweise, im Rahmen einer nichtbestandenen Prüfung an dieser oder einer anderen Hochschule eingereicht wurde.

Göttingen, den 5. August 2012

(Henrike Fleischhack)